# Slope failure analysis using the material point method

Wang, Bin

**Citation (APA)**
Wang, B. (2017). *Slope failure analysis using the material point method*. [Dissertation (TU Delft), Delft University of Technology]. https://doi.org/10.4233/uuid:f24a64b0-ef93-42d7-81a0-a5d34a4eb3dc

**Important note**
To cite this publication, please use the final published version (if applicable).
Please check the document version above.

# SLOPE FAILURE ANALYSIS USING THE MATERIAL POINT METHOD

# SLOPE FAILURE ANALYSIS USING THE MATERIAL POINT METHOD

**Proefschrift**

ter verkrijging van de graad van doctor
aan de Technische Universiteit Delft,
op gezag van de Rector Magnificus prof. ir. K. C. A. M. Luyben,
voorzitter van het College voor Promoties,
in het openbaar te verdedigen op maandag 16 januari om 15:00 uur

door

**Bin WANG**

Master of Science in Geotechnical Engineering,
Wuhan University, Wuhan, China
geboren te Anhui, China.

*To my parents*

# Contents

# 1

# INTRODUCTION

**1**

## 1.1. BACKGROUND

Problems involving large deformations are of great interest and concern in the geomechanics field, such as slope collapses, landslides, and so on. Efforts have been made in understanding the mechanics, both numerically and experimentally (Cascini et al., 2009; Locat et al., 2011, 2013), in order to make more reliable predictions of these catastrophic events. Unfortunately, traditional numerical methods, e.g. the finite element method (FEM), often experience mesh distortion problems in cases of large deformations, which may compel analyses to abort abruptly or give misleading results. Various numerical methods have therefore been proposed and utilised for solving large deformation problems in soil mechanics, with each having their own pros and cons. A summary of some available contemporary numerical methods for the purpose of large strain analyses is made first in the following brief introduction, which leads to the choice of the implementation of the material point method (MPM) in this thesis. The state of the art in slope instability analyses is provided later in the section, where it is found that many theories on failure propagation are based on the back analysis of case histories. Hence, investigations into slope failure mechanisms by using numerical tools, covering both failure initiation and propagation, are highlighted.

### 1.1.1. SUMMARY OF NUMERICAL METHODS FOR LARGE STRAIN ANALYSES

The discrete element method (DEM) has been widely accepted as a useful tool in the engineering field for analysing granular flows, landslides, etc. An assemblage of rigid or deformable blocks/particles, together with the contacts between them, are used to represent soil behaviour in the domain of interest (Jing, 2003). During the deformation process, the contacts are continuously updated. By reducing the size of the particles, a grain level description of the material can inform macro-scale variables, which provides an important connection between micro and macroscopic theories (Soga et al., 2015). Although there are advantages of DEM in many applications, especially in rock mechanics, it suffers intensive computational costs and scores badly in handling boundary conditions. Moreover, the macroscopic responses of materials are strongly influenced by different packing assemblies of particles (Wang and Tonon, 2009; Hentz et al., 2004).

The arbitrary Lagrangian-Eulerian (ALE) method combines advantages from two formulations, i.e. Lagrangian and Eulerian. The ALE method has been developed based on the idea of decoupling the material displacement and mesh displacement to eliminate mesh distortions (Nazem et al., 2009), which thereby introduces two sets of unknown displacements in the global equations. Liu et al. (1986) applied the method to solid mechanics, in which the path-dependent material displacements are solved simultaneously with the mesh displacements, this ALE strategy being referred to as the "coupled" technique. However, the "decoupled" or "operator-split" technique has been more widely used due to its reduced computational cost (Benson, 1989). This involves two steps: an updated Lagrangian (UL) step followed by a convection step. Ghosh and Kikuchi (1991) presented a coupled ALE formulation for solving problems in metal forming processes. Nazem et al. (2008) generalised the method to consider consolidation problems accounting for coupled hydromechanical effects. However, because of the Lagrangian boundary condition restraints, mesh distortion is still observed for large deformation problems using this method (Soga et al., 2015).

The smoothed particle hydrodynamics (SPH) method was initially proposed for astrophysical applications (Lucy, 1977), in which a group of particles representing the continuum carries the field variables, such as mass, density, stress, etc. The equations for the continuum are converted into equations of motion for the particles, and solved by using the updated Lagrangian scheme (Bui et al., 2008). The continuous fields are taken to be interpolated from various particles through a weighted summation, which is described by using an assumed kernel function related to the spatial distance, also called smoothing distance, between the particles. In comparison to traditional grid-based numerical methods, SPH does very well in handling large deformation problems and describing post-failure mechanisms, and in modeling complex free surfaces, as well as being amenable to incorporating complicate physics (Bui et al., 2008). The propagation of catastrophic landslides has been analysed using SPH (Rodriguez-Paz and Bonet, 2005; McDougall and Hungr, 2004), but without taking hydro-mechanical coupling into consideration. However, Bui et al. (2011) extended the SPH formulation by including the pore water pressure for discontinuous slope failure simulation, and Pastor et al. (2009, 2014) further developed a depth-integrated, coupled, SPH model to consider flow-like landslides. However, intensive searching for the neighboring particles after each time step makes the method very time-consuming and, to ensure consistency among the particles, sufficient numbers of particles are needed which is hard to determine a priori. Tensile instability is also found in the code performance, which can cause numerical fractures in the continuum.

The coupled Eulerian-Lagrangian (CEL) approach also captures the strengths of the Eulerian and Lagrangian formulations. It shows an advantage in modeling soil-structure interactions, where the structure can be modeled in the Lagrangian framework, while the soil is tracked as a Eulerian material as it flows through the Eulerian mesh by computing its Eulerian volume fraction (EVF) (Qiu et al., 2011). EVF = 1 means that the element is fully filled with soil, while EVF = 0 is for an empty element. A percentage is designated for each element, representing the portion of the element filled with the material (soil). The interface in between the soil and the structure is explicitly accounted for by taking it to be the boundary of the Lagrangian domain; as the Lagrangian mesh moves together with the material node, it is able to precisely track and define the interface, which shows the main advantage of the approach. Pile jacking, ship grounding, and spudcan penetration have been modeled using this approach (Qiu et al., 2011; Tho et al., 2012), while Dey et al. (2013, 2015) investigated the progressive failures of sensitive clay slopes leading to spread. However, due to the Eulerian description of the material, additional advection terms have to be included for the transfer of the nodal quantities, and greater computational time is required.

The particle finite element method (PFEM) is an evolution of the work for the solution of fluid-solid interaction (FSI) problems using Lagrangian finite element and meshless methods (Oñate et al., 2004). To eliminate the convective terms in the fluid equations and other associated problems, both the fluid and solid are represented using the Lagrangian formulation. Compared to the particle method (e.g. SPH), the nodes of the mesh act as the particles instead and these carry all the state variables, such as density, velocity, stress, etc. An extended Delaunay tessalation (mesh regeneration) technique (Idelsohn et al., 2004, 2006) is used to move the mesh nodes for large motions of

the mesh. Both the fluid and solid domains are solved as in the standard updated La-grangian finite element method (UL-FEM), with each single node being tracked. It pro-vides an efficient way for solving contact and free-surface problems, highly simplifying the treatment of FSI (Idelsohn et al., 2006). More recently, Zhang et al. (2015) applied the method to simulate slope instabilities, covering both failure initiation and propagation. However, due to the large mesh distortions, remeshing may be a frequent necessity with time, which can be very time-consuming and thereby limits the scale of the simulation.

The material point method (MPM) makes use of two formulations, i.e. Eulerian and Lagrangian. It is considered to be a FEM variant (Wang et al., 2016c), which utilises two discretisations: one represented by the material points, that is, the Lagrangian mesh; and the other by the background mesh, that is, the Eulerian mesh. The information associated with the problem is stored at the material points and tracked through the whole computation. When subjected to loading, the material points can move freely through the background mesh. The mesh is used only for the computation and can be reset regularly. Based on the way the governing equations are solved, either explicitly or implicitly, MPM can be divided into two categories: implicit and explicit MPM. Since its invention (adaptation) for solid mechanics in 1994 (Sulsky et al., 1994), a wide range of applications have used the method, including wave breaking on a dyke (Jassim et al., 2013), snow simulation in the cartoon film "frozen" (Stomakhin et al., 2013), levee failure propagation (Bandara and Soga, 2015), and 3D analyses of the mechanics of vascularized scaffolds under tension (Guilkey et al., 2006).

In contrast to the other numerical methods mentioned above, several advantages of MPM can be summarised: 1. MPM can be easily converted from a FEM code, as it is basically a FEM variant; 2. there is no need to transfer information between the nodes (with the information stored on the material points), which improves the solution accu-racy and is more time-efficient; 3. handling boundary conditions is substantially easier than in DEM and SPH, as the tractions and displacement boundaries can be applied to the boundary particles or to the boundary layers (Chen and Brannon, 2002) directly, without using the information from neighboring particles.

### 1.1.2. SLOPE FAILURES

Informally, "a movement of a mass of rock, earth or debris down a slope" is defined as a landslide (Cruden, 1991). Based on the type of material (e.g. rock, soil) and the mode of the movement (e.g. falls, slides) involved, various types of landslides have been iden-tified (Cruden and Varnes, 1958; Varnes, 1978; Hungr et al., 2014). The corresponding failure mechanisms, mostly through the back analysis of case histories, are also diverse and complicated, due to the interactions of adjacent sliding bodies (Hungr et al., 2014). A number of related descriptions are summarised (Cruden and Varnes, 1958), such as ad-vancing, enlarging, progressive or retrogressive. If an initial slide occurs and the material in the failure flows away, which is usually caused by a high degree of strength loss, a steep main scarp will usually be formed and, therefore, support from remaining soil will be re-moved. This can result in another failure, termed a retrogressive failure. This process can repeat itself in a multiple-retrogressive fashion and can result in a bigger landslide. The recent Oso landslide in Washington was observed to have multi-rotational retrogressive failures in parts and large translational slides in the longer slopes (Keaton et al., 2014), as

(a) Oso landslide, USA, March 22, 2014 (Keaton et al., 2014)



(b) Qianjiaping landslide, China, June 10, 2003 (Wang et al., 2004)

Figure 1.1: Typical slope failure modes

shown in Fig. 1.1(a). Meanwhile, it should be noted that such strength loss during slope failures does not occur instantaneously, but is associated with the magnitude of the plastic shear strains. Hence the rupture surface normally propagates through the soil profile in a progressive way, such as in the reported progressive failures of observed landslides in Scandinavia and eastern Canada (Locat et al., 2011). Fig. 1.1(b) shows a typical failure mode for a rock slope, where a large translational slide is shown to happen along the layered weak bedding fault zones at the rear scarp; this landslide occurred very rapidly and over $2000 \times 10^4$ m$^3$ of soils slid into the reservoir, resulting in the deaths of 14 people and over 2000 people homeless (Wang et al., 2004). The occurrence of toe erosion due to a water level increase is considered as the main triggering agent for this landslide.

In slope (in)stability, thousands of studies have been carried out, but, in most cases, these have been confined to the initiation of the slope failure. Limit equilibrium methods (LEMs), such as Fellenius' method (Fellenius, 1936), Bishop's method (Bishop, 1955), etc., are favoured by many engineers, mostly for their simplicity. There are, however, some deficiencies with regard to LEMs, such as the assumptions relating to the interslice forces, zero deformation of the soil, and that the location and shape of the failure plane

**1**

have to be assumed in advance. FEM combined with the strength reduction technique (Griffiths and Lane, 1999) has been widely used to analyse slope stability, i.e. to calculate the slope factor of safety (FOS). Also, for considering the spatial variations of soil material properties in slope stability analyses, the random finite element method (RFEM), which combines finite elements and random field theory (Fenton and Vanmarcke, 1990), has been proposed (Hicks and Samy, 2002; Hicks and Onisiphorou, 2005). In this context, reliability (or conversely, probability of slope failure) is proposed to more comprehensively quantify slope safety. For example, the mean FOS for a heterogeneous soil slope is found to be smaller than the deterministic solution based on the mean values of the soil properties, due to greater relative influence of weaker zones (Hicks and Nuttall, 2012).

Investigations into the conditions triggering landslides have also been initiated (Dai and Lee, 2001; Tsaparas et al., 2002; Kilburn and Petley, 2003; Lin et al., 2006), in order to find efficient ways to mitigate landslides along with their significant impacts. Pore water pressure elevation was generally accepted to be crucial for the instability of Mt. Toc (Hendron and Patton, 1987), which catastrophically collapsed into Italy's Vajont reservoir on 9 October 1963, claiming more than 2000 lives (Müller-Salzburg, 1964). Rainfall induced slope failures have also happened frequently. During and antecedent to a rainfall event, with water infiltrating into the soil, slope failures may occur due to a loss in matric suction due to the increasing degree of saturation. Many attempts (Ng et al., 2001; Tsaparas et al., 2002; Rahardjo et al., 2007) have been made to investigate the influences of changing climatic conditions, infiltration characteristics, etc., on associated slope failures. Earthquakes can also trigger serious coseismic landslides, as well as extensively disturb surface strata around the epicentral area. Lin et al. (2006) compared the occurrence of landslides along the Choushui River, during the period from 1996 to 2001 (after the Chi-Chi earthquake) in central Taiwan, and found that the density of rainfall induced landslides was significantly increased.

To conclude, factors, such as spatial variations of soil properties and rainfall, have apparent and significant impacts on slope stability. So far, efforts to investigate these problems have mainly been made using a small deformation analysis framework. However, by incorporating large deformation theory, the risk posed by potential secondary failures (e.g. due to support being removed from the initial sliding blocks) of a slope failure mechanism can be more comprehensively quantified and understood. This helps to mitigate or minimise the risk of potential damage. As stated above, mesh distortions due to large deformations render FEM more limited in predicting the slope post-failure behaviour. Remeshing techniques can be quite time consuming, and the resulting mapping of variables between nodes causes inaccuracies in the computation. In contrast, compared to other contemporary numerical methods, MPM shows certain advantages in some aspects, and has proven to be a reliable tool in capturing large deformations in geomechanics (Al-Kafaji, 2013). Hence, MPM has been chosen and further developed in this thesis, in order to provide a more complete description of slope failure mechanisms, covering both failure initiation and the continuing development of the failure.

## 1.2. OBJECTIVES

The objective of this thesis is to provide a more complete and comprehensive understanding of slope failure mechanisms, covering both the failure initiation and the failure

consequences. Factors to be examined include excavations at the slope toe, spatial variations of soil properties and rainfall.

In detail, three research components are presented in this thesis. Firstly, an implicit material point method (IMPM) is developed, following standard FEM procedures where possible, which aims to provide a straightforward framework for adapting an FEM code into an MPM code. In this thesis, IMPM will be applied to the simulation of retrogressive and progressive failures of a slope, giving a full description of the slope failure mechanism, from the onset of failure, to the failure propagation, until the final equilibrium state is reached. Secondly, MPM will be extended and combined with random field theory, in order to provide a strategy for studying the influence of spatial variability of soil properties on the post-failure behaviour of slopes. Finally, for analysing the effects of rainfall infiltration on the slope failure mechanism, a coupled material point method (CMPM) will be developed by including the pore water pressure, via a velocity formulation, in which both the solid and fluid phase velocities are the variables.

## 1.3. OUTLINE OF THE THESIS

Including this introduction, the thesis is arranged in six chapters, in which relevant literature is introduced in this chapter and given in detail in the following most appropriate chapters.

An implicit material point method formulation is developed and described in Chapter 2. The formulation refers to a framework in which both quasi-static and dynamic problems can be solved. The derivation process, based on the finite element method, is detailed, in which three computation phases can be identified: i.e. the initiation phase, the updated Lagrangian (UL) phase, and the convection phase. Examples of implicit MPM in this chapter include quasi-static applications, in which a cantilever beam problem gives insight into the influence of the number of material points per element and an extra background stiffness; and dynamic problems, comprising a vibrating bar and sand column collapse. Comparisons with explicit MPM are provided at the end of the chapter, which aim to highlight the advantages of implicit MPM, especially with regard to the size of the time step.

By utilising the proposed implicit material point method, the retrogressive and progressive failure mechanisms of two types of slopes, which, for convenience, are called "short slope" (slope height = 5.0 m) and "long slope" (down-slope length ≈ 25.0 m), are investigated in Chapter 3. A simple cohesion softening model, coupled with the Von Mises failure criterion, is presented to characterize the soil constitutive behaviour. For the short slope, the influence of an excavation at the slope toe is first presented, to demonstrate the ability of the method to quantify the consequence of a geotechnical instability. A detailed collapse process is then modelled, which explicitly shows the slope retrogressive failure mechanism. The slope failure initiation, and influences of softening modulus and residual shear strength, are then investigated. For the long slope, the influence of slope angle is of primary concern, and shows a close relationship with the slope failure type.

The random material point method (RMPM), which combines MPM with random field theory, is presented in Chapter 4, and the basic difference from RFEM is illustrated. A brief introduction to random field theory, and the local average subdivision (LAS) al-

gorithm which is used for generating the random field, are first provided. The same two types of slopes modelled in the previous chapter are investigated. For the short slope, the sliding distances are recorded to quantify the risk posed by the ongoing failures. For the long slope, the failure mechanism is mainly investigated by considering the influences of the horizontal scale of fluctuation, slope angle, and mean shear strength trend with depth. Comparisons with determinstic analyses are also provided.

The research is extended to investigate a rainfall-induced slope slide using the coupled material point method in Chapter 5. Existing multi-phase MPM theories are reviewed first, where the one-particle two-phase formulation proposed by (Al-Kafaji, 2013) for modeling saturated soils is adopted and implemented in the research. For modeling unsaturated soils, the formulation is extended by including the degree of saturation, although the gas phase is not considered here for reasons of simplicity. An infiltration problem is used to verify the extended formulation and then an analysis of a rainfall-induced slope failure process is presented.

The concluding remarks of the research and outlook to future work are presented in Chapter 6.

# 2

# MATERIAL POINT METHOD

*An implicit version of the material point method (MPM), a variant of the finite element method (FEM), is presented in this chapter. The key feature of MPM is that the spatial discretisation uses a set of material points, which are allowed to move freely through the background mesh. All history-dependent variables are tracked on the material points and these material points are used as integration points similar to the Gaussian points. A mapping and re-mapping algorithm is employed, to allow the state variables and other information to be mapped back and forth between the material points and background mesh nodes during an analysis. The main purpose of this chapter is to provide a unified MPM framework, in which both quasi-static and dynamic analyses can be solved, and to demonstrate the model behaviour. The implementation closely follows standard FEM approaches, where possible, to allow easy conversion of other FEM codes.*

Parts of this chapter have been published in Computers and Geotechnics, **71**, 159-167, 2016 (Wang et al., 2016c).

**2**

## **2.1.** INTRODUCTION

In computational problems involving large-strains, such as granular flow or plastic form-ing, the finite element method (FEM), which is most frequently used nowadays in such analyses, may exhibit some disadvantages; i.e. the finite element mesh may suffer from extreme distortions, sometimes causing the Jacobian matrix to be negative, so that the calculation cannot continue. Given such a situation, other computational techniques have started to be investigated and used.

Generally, the methods can be classified as either Eulerian or Lagrangian methods, with each having its own advantages and disadvantages (Zhang and Chen, 2007). In Eu-lerian methods, the description of motion is with reference to the spatial coordinates. Attention is given to what is occurring at a fixed point in space as time progresses. This approach is commonly applied in the study of fluid flow. One common example of a mesh-based Eulerian method is the finite volume method (FVM). Moreover, as the com-putational mesh is decoupled from the material, convective terms appear in Eulerian FEM, introducing numerical difficulties because of the non-symmetrical properties of the resulting governing equation (Donea et al., 2004).

In contrast, in Lagrangian methods the equations of motion are formed in terms of the material coordinates. Attention is given to the material as it moves in space as time progresses, and the results obtained are independent of the choice of initial time and reference configuration. This method is normally employed in solid mechanics. The nu-merical representation of a solid is assumed to be tied to the solid, and follows the body as it moves through space and time. The updated Lagrangian finite element method (UL-FEM) is a widely used method, in which it is assumed that the computational mesh deforms together with the considered body, and all static and kinematic variables are referred to the last calculated configuration in the solution. It performs well in defining free surfaces and in handling history-dependent material behaviour. However, signifi-cant mesh distortions can exist in large deformations, and mesh re-zoning and mapping is usually needed, which is time-consuming and introduces errors.

Meshless methods do not use a mesh, and the material is often described by a cloud of points. Each individual point represents a sub-region of the considered material. A main feature of this kind of method is that all state variables are traced at the points, and hence the problem of mesh distortion inherent in FEM is overcome. However, it has dis-advantages with some problems yet unsolved, such as boundary treatments, large rota-tions and interactions between different material phases. Moreover, the computational efficiency of using meshless methods is very low (Belytschko et al., 1996)

By taking advantage of both Lagrangian and Eulerian methods, Sulsky et al. (1994, 1995) developed the material point method (MPM) for the simulation of the dynamic deformation processes of solid bodies. Their work is based on the particle-in-cell (PIC) method, which was proposed by Harlow (1964) in the 1960s for problems in fluid me-chanics, and the motivation of the development was to simulate problems such as im-pact/contact, penetration and perforation with history-dependent internal state vari-ables.

MPM uses two spatial discretisations, as shown in Fig. 2.1. The first, in which state variables are traced on a set of material points, takes a Lagrangian perspective and repre-sents the body of the continuum, while the equation of motion is formulated and solved

on the second, i.e. Eulerian, mesh (the background computational mesh). The computational mesh maintains its original position, or is adjusted in an appropriate way to avoid mesh distortion after each loading/time step, thereby removing the disadvantage from FEM of extreme mesh distortion.
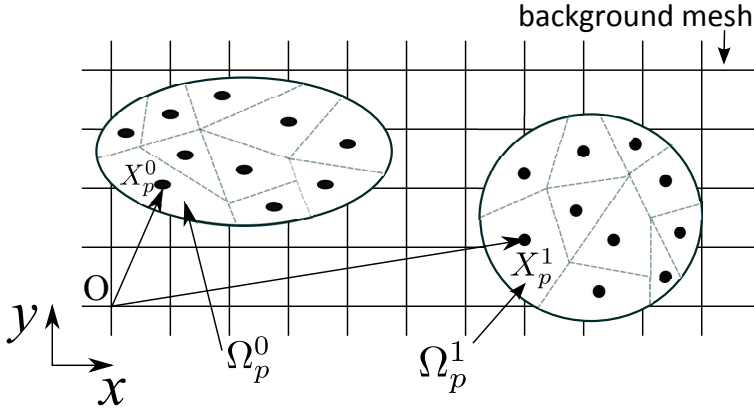


Figure 2.1: Sketch of computational grid and material elements, in which the superscript "0" represents the continuum initial state, "1" stands for the deformed state, and the background grid is used for the computation (after Sulsky et al. (1994)).

Due to its unique features, the advantages obtained from using MPM are as follows (Shin, 2009):

(a) It can simulate large deformations without mesh entanglement;

(b) It implicitly satisfies the conservation of mass;

(c) It allows the assignment of different constitutive relations to different material points, which is useful for modelling composite materials;

(d) There are algorithmic similarities between MPM and other numerical methods, so that existing theories for these methods can be applied to MPM;

(e) It can be adapted for parallel computation in a relatively easy manner.

It has been demonstrated that MPM is a very useful numerical tool in solving problems involving large deformations, and it has been applied successfully in many fields, e.g. silo discharge (Wieçkowski et al., 1999), explosion problems exploiting its ability of representing an arbitrary geometry (Henderson et al., 2000; Hu and Chen, 2006), crack propagation (Nairn, 2003), large-scale response of cellular constructs in biomechanics (Guilkey et al., 2006), and snow simulation in computer graphics (Stomakhin et al., 2013). Applications in geotechnical engineering include retaining wall failures (Wieçkowski, 2004), modeling of anchor pull-out (Coetzee et al., 2005), soil column collapse (Andersen and Andersen, 2009; Kumar et al., 2013), landslides and debris flows (Shin, 2009), landslide-induced interactions with structures (Mast, 2013) and pile installations (Phuong et al., 2014).

Due to the way of solving the governing equations, MPM can be divided into two categories; explicit and implicit MPM. MPM, so far, has been mostly developed within the framework of explicit time integration, mainly due to its convenience in implementation. However, in terms of choosing the time step size and achieving a high accuracy in problems, especially those associated with plastic strains, it suffers from some restrictions. Implicit MPM, employing an implicit time integration scheme, has been developed more recently. Sulsky and Kaul (2004) adopted the Newton-Krylov technique coupled with the conjugate gradient (CG) method to solve the governing equations in a robust, matrix-free fashion. Guilkey and Weiss (2003) explicitly formed the tangent stiffness matrix and used the Newton-Raphson iterative method together with a Newmark integration scheme to solve the equilibrium equations in time. Wang et al. (2014) investigated different aspects of the algorithm in terms of accuracies and energy conservation errors. Beuth et al. (2011) and Wang et al. (2013) presented some geotechnical applications, e.g. a soil slope stability problem, using a quasi-static MPM.

This chapter starts with a review of the explicit material point method, along with various contributions through the years, and aims to clarify the basic principles of MPM. An implicit MPM framework is then presented, in which quasi-static and dynamic problems can be solved. Details with respect to the formulation and implementation are described. Numerical examples to verify the framework are provided at the end of the chapter.

## 2.2. EXPLICIT MATERIAL POINT METHOD

This section reviews MPM with an explicit time integration scheme. A general computational cycle is given first, to illustrate the standard mapping and remapping procedure between the material points and background computational mesh. The formulations and discretisations of MPM are then provided. As stated in Sulsky et al. (1994, 1995), three phases constitute a computational cycle, in which the key phase of solving the governing equations on the background mesh according to the updated Lagrangian formulation is introduced in detail in the following. Stress oscillations are reported to be one of the main issues inherent in MPM (Bardenhagen and Kober, 2004); as stresses are calculated directly on the moving material points using the nodal shape function differentials of the background mesh, while low-order elements are normally adopted in MPM for excluding the possible negative terms in the mass matrix forming process, the discontinuities of the shape function gradients and the stresses between the elements are thereby resulted. Some work has been carried out to modify the shape functions of the background mesh in order to improve the accuracy of MPM stress integrations, and this is presented in the last part of the section.

### 2.2.1. GENERAL DESCRIPTION

The main MPM algorithm for a single time/loading step is schematically shown in Fig. 2.2, which depicts the roles of both the material points and background computational mesh. Three phases are identified: mapping phase, UL-FEM phase and convection phase. In the first phase, Fig. 2.2(a), the state variables (e.g. velocities, accelerations, etc.) are mapped from the material points to the nodes of the background mesh; in the

second phase, Fig. 2.2(b), the equation of motion is solved over the background mesh by utilising the UL-FEM to find the current acceleration, with the element integration being based on the material points (rather than on the information mapped to Gauss points); and, in the third phase, Fig. 2.2(c), the state variables on the material points are updated via remapping from the deformed background mesh, and the mesh is then reset, leaving the material points at their updated locations. These phases are repeated until the end of the time/loading steps.

Connectivity can be set up between the material points and grid nodes, and thus information can be mapped back and forth between them. It is also worth noting that, due to the different ways that may be adopted for solving the equation in time in the second phase, the formulation can yield either implicit or explicit MPM approaches.



(a) Mapping phase

(b) UL-FEM phase

(c) Convection phase
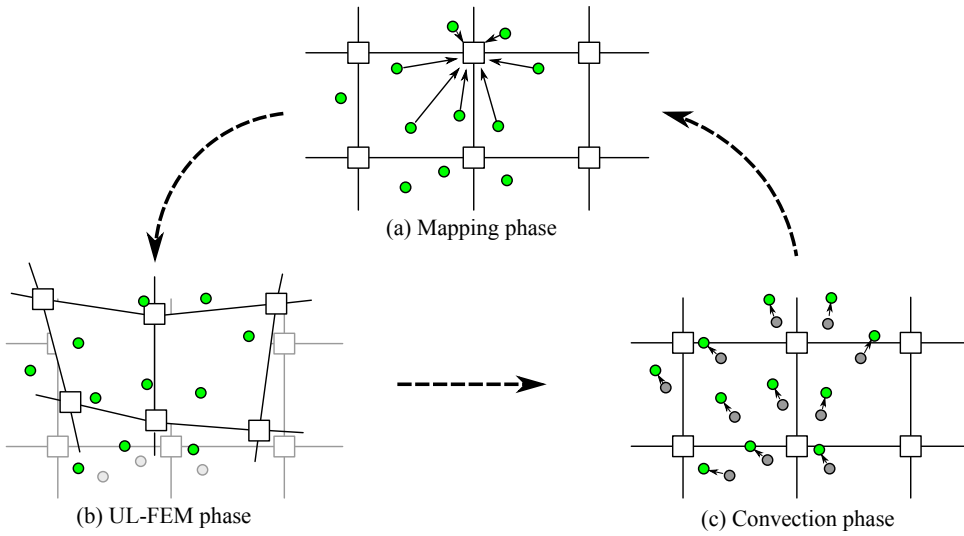
Figure 2.2: Computational cycle of MPM. (a) A set of material points representing the material, overlaid on a background computational mesh. Material properties, constitutive models and other state information are assigned to, and stored only on, the material points. Information is transferred to the nodes of the background mesh for computational purposes. (b) The equations of motion are solved on the background mesh, utilising UL-FEM. (c) The state of the material points is updated, and the background mesh reset.

### 2.2.2. FORMULATIONS OF EXPLICIT MATERIAL POINT METHOD

By applying the mass and momentum conservations, the governing differential equations at the continuum scale are

$$\frac{d\rho}{dt} + \rho\nabla\mathbf{v} = \mathbf{0} \tag{2.1}$$

$$\rho\mathbf{a} = \nabla\boldsymbol{\sigma} + \rho\mathbf{b} \tag{2.2}$$

which also require a constitutive equation to describe the stress-strain behaviour. In Eqs. (2.1) and (2.2), $\rho$ is the mass density, $\mathbf{v}$ is the velocity, $\mathbf{a}$ is the acceleration, $\boldsymbol{\sigma}$ is a

symmetric stress tensor and **b** is the body force due to, for example, gravity. Note that all these variables are functions of time and the positions of the material points.

Eq. (2.1) is automatically satisfied, as the spatial discretisation of the material leads to each material point having a mass which is fixed in time. Before each time/loading step, information is transferred to a background computational mesh from the material points. This mesh should be large enough to cover the moving trajectories of all the material points, and the details of its specification are chosen for computational convenience. With regard to the momentum equation, Eq. (2.2), by applying the principle of virtual displacement, followed by the use of the divergence theorem, the equilibrium equation expressed in the weak form (Bathe, 1996) is given by

$$\int_{\Omega} \rho \boldsymbol{\omega} \mathbf{a} d\Omega = -\int_{\Omega} \rho \boldsymbol{\sigma} : \nabla \boldsymbol{\omega} d\Omega + \int_{S^c} \rho \mathbf{c}^s \boldsymbol{\omega} dS + \int_{\Omega} \rho \boldsymbol{\omega} \mathbf{b} d\Omega \qquad (2.3)$$

where $\boldsymbol{\omega}$ denotes the test function, which is assumed to be zero where the displacement boundary conditions are prescribed, $\boldsymbol{\sigma}$ is the Cauchy stress, $\Omega$ represents the configuration of the continuum body, and $S^c$ is the boundary subjected to a prescribed traction $\mathbf{c}^s$.

To solve Eq. (2.3), it must be spatially discretised. MPM discretises a continuum body in the original configuration into a group of $N_p$ material points which move due to the deformation process. Usually, MPM treats each point as a mass, without a defined shape but occupying space; for example, the material point mass can be assigned by integrating the continuum properties over the space, i.e.

$$m_p = \int \rho(\mathbf{x}, t) \delta(\mathbf{x} - \mathbf{x}_p) dV_p \qquad (2.4)$$

and

$$\sum_{p=1}^{N_p} m_p = \sum_{p=1}^{N_p} \int \rho(\mathbf{x}, t) \delta(\mathbf{x} - \mathbf{x}_p) dV_p = \int \rho(\mathbf{x}, t) d\Omega \qquad (2.5)$$

where $m_p$ is the mass associated with the material point $p$, $\delta$ is the Dirac delta function, $V_p$ is the material point volume, $N_p$ is the number of material points, $\mathbf{x}$ is the current position of any point in the continuum and $\mathbf{x}_p$ denotes the current position of material point $p$.

Hence, Eq. (2.3) can be discretised similarly by summing the material properties over the material points, namely

$$\sum_{p=1}^{N_p} m_p [\boldsymbol{\omega}(\mathbf{x}_p^t) \mathbf{a}(\mathbf{x}_p^t)] = \sum_{p=1}^{N_p} m_p [-\boldsymbol{\sigma}(\mathbf{x}_p^t) : \nabla \boldsymbol{\omega}|_{\mathbf{x}_p^t} + \boldsymbol{\omega}(\mathbf{x}_p^t) \mathbf{c}^s(\mathbf{x}_p^t) h^{-1} + \boldsymbol{\omega}(\mathbf{x}_p^t) \mathbf{b}(\mathbf{x}_p^t)] \qquad (2.6)$$

where $h$ is the thickness of the boundary layer. The interactions between material points are described by utilising the shape functions from the background computational mesh. In this case, the shape functions are the same shape functions as used for FEM.

The spatial coordinates of a material point at time $t$ can then be recovered, by using the shape functions, as

$$\mathbf{x}_p^t = \sum_{i=1}^{N_n} N_i(\mathbf{x}_p^t)\mathbf{x}_i^t \tag{2.7}$$

where $N_i(\mathbf{x}_p^t)$ are the shape functions associated with spatial nodes $i$ and $\mathbf{x}_i^t$ are the nodal coordinates. Kinematic compatibility requires that the shape functions move along with the material, as in the updated Lagrangian framework; that is, the shape functions must be independent of time. Therefore, all the kinematic variables can be represented in the same way as for the coordinates in Eq. (2.7).

By using standard FEM procedures and the MPM equations developed above, the final discretised governing equations can be written as

$$\mathbf{M}_i\mathbf{a}_i^t = (\mathbf{F}_i^t)^{ext} - (\mathbf{F}_i^t)^{int} = \mathbf{F}_i^t \tag{2.8}$$

where $\mathbf{F}_i^t$ is the resultant nodal force, and $(\mathbf{F}_i^t)^{ext}$ and $(\mathbf{F}_i^t)^{int}$, respectively, represent the external and internal forces acting on the node $i$. For a detailed derivation of the process and expressions for the matrices, readers can resort to Sulsky et al. (1994, 1995).

### 2.2.3. UPDATE OF KINEMATIC VARIABLES

As the information is carried by the material points, while the governing equations are solved on the background mesh, this makes mapping and remapping between the material points and background mesh nodes necessary. Corresponding to the three MPM phases illustrated in Fig. 2.2, the kinematic variables need to be updated three times within the MPM computational cycle.

#### MAPPING PHASE

Since information, such as velocity and acceleration, is initially stored at the material points and the background mesh is reset regularly after each time step, it is necessary to map (i.e. transfer) the associated kinematic information from the material points to the grid nodes at time $t$ utilising the shape functions, i.e.

$$\mathbf{m}_i^t = \sum_p N_i(\mathbf{x}_p^t)m_p \tag{2.9}$$

and

$$\mathbf{v}_i^t = \frac{\sum_p N_i(\mathbf{x}_p^t)m_p\mathbf{v}_p^t}{m_i^t} \tag{2.10}$$

in which $i$ refers to a grid node, $p$ refers to material points surrounding the grid node, $\mathbf{m}_i = \begin{pmatrix} m_i & 0 \\ 0 & m_i \end{pmatrix}$ and $\mathbf{v}_i$ are the node mass and velocities (2D conditions are assumed for the mass matrix), respectively, which are assembled from the material points within the adjacent elements, $m_p$ is the material point mass, and $\mathbf{v}_p$ is the material point velocity.

Accelerations are updated in the same way, but note that the displacement is initialized to zero at the beginning of each time step, i.e. $\mathbf{u}_i^t = 0$ .

**2**

### UPDATED LAGRANGIAN PHASE

After the governing equations are solved on the background mesh, the accelerations on the material points are obtained as follows,

$$\mathbf{a}_p^t = \sum_{i=1}^{N_n} \frac{\mathbf{F}_i^t}{m_i^t} N_i(\mathbf{x}_p^t) \tag{2.11}$$

in which $\mathbf{a}_p$ is the material point acceleration, and $N_n$ is the number of nodes in an element (local support).

The velocities for the current time step are then updated as

$$\mathbf{v}_p^{t+\Delta t} = \mathbf{v}_p^t + \mathbf{a}_p^t \Delta t \tag{2.12}$$

where $\Delta t$ is the incremental time step, which is chosen subject to the Courant-Friedrichs-Lewy (CFL) condition.

Hence, the new nodal values of velocity are obtained via mapping from the related material points to the grid nodes,

$$\mathbf{v}_i^{t+\Delta t} = \frac{\sum_p (m\mathbf{v})_p^{t+\Delta t} N_i(\mathbf{x}_p^t)}{m_i^t} \tag{2.13}$$

The material point strain increment is then updated by evaluating the velocity gradient terms on the material point positions. The stress increment is subsequently obtained by using an appropriate constitutive model. Related internal state variables are also assigned to and tracked on the material points during the computation process.

### CONVECTION PHASE

The momenta on the material points for the new time step $t + \Delta t$ are updated using,

$$(m\mathbf{v})_i^{t+\Delta t} = (m\mathbf{v})_i^t + \mathbf{F}_i^t \Delta t \tag{2.14}$$

and the new nodal velocities are used for updating the positions of the material points. The velocities of the material points at time $t + \Delta t$ are expressed as,

$$\bar{\mathbf{v}}_p^{t+\Delta t} = \sum_{i=1}^{N_n} \frac{(m\mathbf{v})_i^{t+\Delta t}}{m_i^t} N_i(\mathbf{x}_p^t) \tag{2.15}$$

and thereby the new positions are,

$$\mathbf{x}_p^{t+\Delta t} = \mathbf{x}_p^t + \bar{\mathbf{v}}_p^{t+\Delta t} \Delta t \tag{2.16}$$

A computational cycle within a time step is completed when all the necessary information has been updated on the material points. The background mesh can then be discarded or reset for the convenience of computation in the new time step. Note that two particle velocities are obtained, as seen in Eqs. (2.12) and (2.15), which are used to update the stresses and positions of the material points, respectively. The use of velocity $\bar{\mathbf{v}}_p^{t+\Delta t}$ instead of the velocity $\mathbf{v}_p^{t+\Delta t}$ to update the material point position is to reduce the numerical error, as a tiny value of $m_i^t$ in the denominator in Eq. (2.11) could be possible, which may cause an abnormal acceleration on the material point $\mathbf{a}_p^t$. Due to the

use of the same set of shape functions for both the mapping (from material points to background mesh) and re-mapping phase (from background mesh to material points) at each time step, the interpenetration between material bodies is precluded in MPM, which enables simulations of impact and penetration problems of MPM without resorting to an extra contact algorithm (Chen and Brannon, 2002).

### 2.2.4. IMPACT OF TWO BARS

Two classic impact examples (Chen and Brannon, 2002) are provided here to verify the explicit MPM performance. As shown in Fig. 2.3, two bars of equal length $L = 0.5$ m are separated by an initial distance of 0.5 m. Constant velocities of $v = 1.0$ m/s and $v = -1.0$ m/s are assigned to the left and right bars, respectively, and they are allowed to translate freely. Each bar is modeled using 50 quadrilateral elements, of size 0.01 m × 1.0 m, and each element initially contains one particle. The Young's modulus is $E = 10000$ kPa, Poisson's ratio is $v = 0$, and mass density is $\rho = 1.0 \times 10^3$ kg/m$^3$, so that the wave speed is $c_v = \sqrt{E/\rho} = 100$ m/s. The time step is chosen as $2.5 \times 10^{-4}$ s.
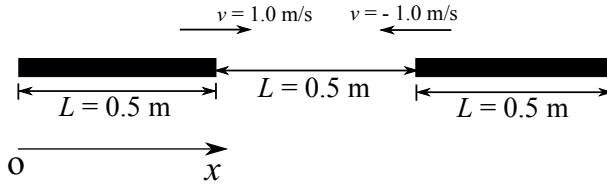


Figure 2.3: Initial conditions for two impacting bars

The two bars start to collide at time $t = 0.245$ s and remain in contact for a period of $2L/c$, before separating from each other when the reflected tensile waves cancel the compressive waves and reach the middle points of the respective bars. The stress profiles along the bars, at different times before and during the impact, are shown in Fig. 2.4. The contact stress can be obtained analytically as $\sigma = \rho * c_v * v = -100$ kPa (tension is taken as positive), and the numerical results show good agreement with the analytical solution.

#### BAR IMPACT WITH PERFECT PLASTICITY

For the following example, all the conditions are the same as in the above example, except that an elastio-plastic constitutive equation is applied; that is, a Von Mises failure criterion is used, with a perfect-plasticity model. The motions and stresses of the two bars are examined, and compared with the analytical solution.

The bars have a Young's modulus of 10000.0 kPa, a Poisson's ratio of 0.0, a density of $\rho = 1.0 \times 10^3$ kg/m$^3$ and a yield stress of 50.0 kPa. The initial velocities of the two bars are 1.0 m/s and -1.0 m/s respectively, as in the previous example.

In order to save computation time, the two bars are initially placed nearer to each other, compared to the example shown before, with a separation distance of 0.1 m. The simulation is run to a maximum time of 10.0 s. Figure 2.5 describes the moving trajectories of four particles with time, located in the middle of the left bar, right end of the left bar, middle of the right bar and left end of the right bar, respectively. It is interesting to note that, after the two bars collide, the two bars stick together rather than bounce off
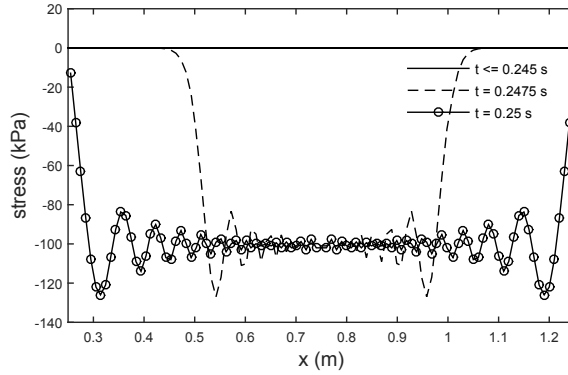
(a) prior to and during the impact
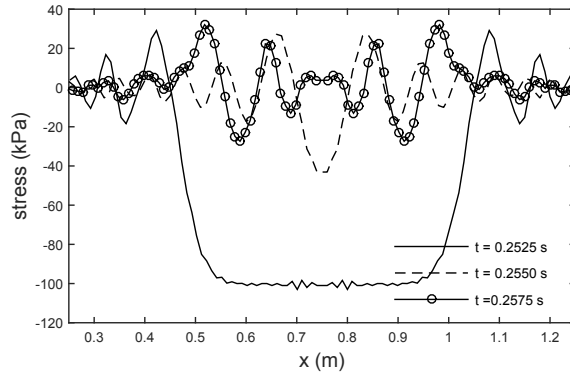


(b) after the impact

Figure 2.4: Elastic stress wave propagation along the two bars; time step is chosen as $2.5 \times 10^{-4}$ s.

each other as shown in the previous case. This is because no extra elastic energy is generated, after the bars go to perfectly plastic, which can be transformed back to kinetic energy to force the bars apart.

The corresponding stress profiles along the two bars are shown in Fig. 2.6. Three different times are chosen, which clearly show the stress wave propagation through the bars. At the time of 0.0475 s, the compressive waves have propagated to the middle points of both bars; hence, the parts of the bars where the waves have traveled through have reached the yield stress, whereas the rest remains at zero. By the time of 0.05 s, the compressive waves have reached the ends of the two bars and all the particles have gone into the plastic stage due to the stress reaching the yield stress.
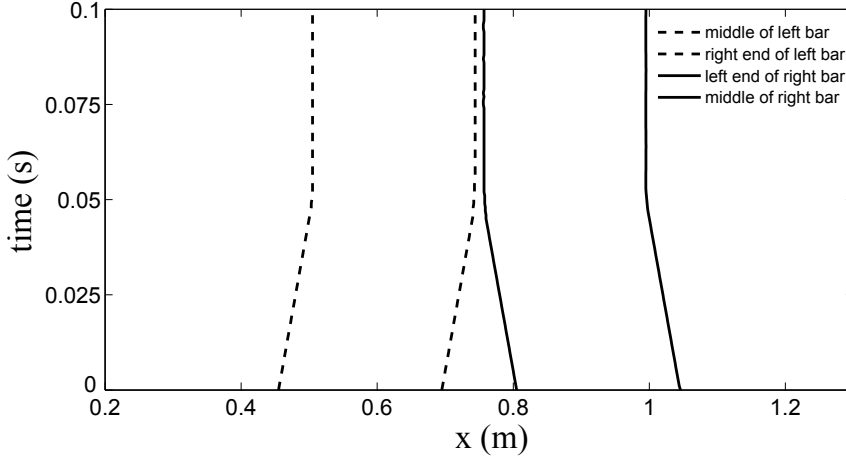
Figure 2.5: The moving trajectories of four specified particles, located in the middle of the left bar, right end of the left bar, middle of the right bar and left end of the right bar, respectively.

### 2.2.5. ADVANCES IN MATERIAL POINT METHOD DEVELOPMENT

Stress oscillations are reported to be one of the main issues inherent in MPM formulations (Bardenhagen and Kober, 2004). As material points cross a cell boundary, with the low-order shape functions adopted, the gradients of the shape functions result in discontinuities in between the elements, which causes discontinuities in the stress calculation. In severe cases, this can make the analysis collapse abruptly. Therefore, many efforts have been made in order to improve the stress performances, where the key feature among different MPM versions is the choice of the shape functions (Steffen et al., 2008). By introducing a particle characteristic function $\chi_p$, Bardenhagen and Kober (2004) developed a family of generalized interpolation material point (GIMP) methods, in which the material points are defined to occupy space. Although the GIMP approach is not implemented within the thesis, it has proven to be a useful tool in reducing the stress oscillations (Bardenhagen and Kober, 2004), and will be a future research subject. The density is modified as

$$\rho(\mathbf{x}, t) = \sum_{p=1}^{N_p} \rho_p \chi_p \qquad (2.17)$$

where the material density is non-zero over a small volume rather on a fixed position $\mathbf{x}_p$ as shown in Eq. (2.4). The weighting function and weighting function gradient are used to weight the nodal contributions from the material points instead of the original standard shape function, that is

$$\boldsymbol{\varphi}_i(\mathbf{x}_p) = \frac{1}{V_p} \int_{\Omega_\chi} \chi_p(\mathbf{x} - \mathbf{x}_p) \mathbf{N}_i(\mathbf{x}) d\mathbf{x} \qquad (2.18)$$

$$\nabla \boldsymbol{\varphi}_i(\mathbf{x}_p) = \frac{1}{V_p} \int_{\Omega_\chi} \chi_p(\mathbf{x} - \mathbf{x}_p) \nabla \mathbf{N}_i(\mathbf{x}) d\mathbf{x} \qquad (2.19)$$
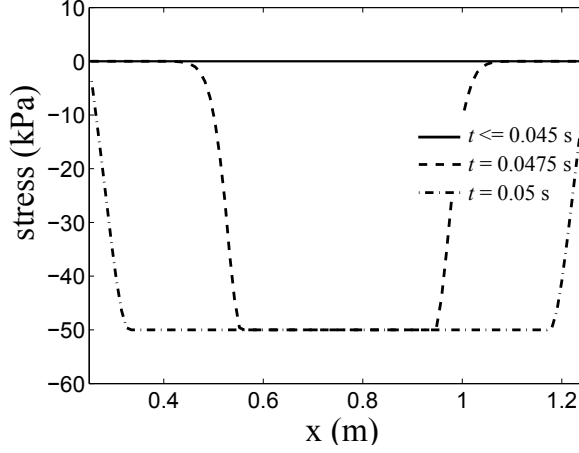
Figure 2.6: The stress profiles along the bars at three different times; Von Mises model with perfect plasticity

where $\chi_p$ is the particle characteristic function, $\Omega_\chi$ denotes the integral domain of the function, and $\boldsymbol{\varphi}_i(\mathbf{x}_p)$ and $\nabla\boldsymbol{\varphi}_i(\mathbf{x}_p)$ are the weighting function and weighting function gradient, respectively, which are intended to smooth out the discontinuity over a finite domain $V_p$.

Various selections of characteristic functions can be made, given that the requirement of the functions to be a partition of unity is met. Eq. (2.20) gives the simplest form of the generalisation, which retains the grid shape functions used in the original MPM, but replaces the particle mass points with particle volumes (Bardenhagen and Kober, 2004).

$$\chi_p(\mathbf{x}) = \begin{cases} 1 & if\,\mathbf{x}\in V_p \\ 0 & otherwise \end{cases} \tag{2.20}$$

where $V_p$ represents the domain occupied by the material point. This work is further developed by Ma et al. (2006), in which the material point domains are taken to be rectangles in 2D and are assumed to evolve with time such that the artificial separation observed, especially in tensile simulations, may be eliminated.

Sadeghirad et al. (2011) reported that the assumption of material point domains as rectangles (in 2D) is not accurate, due to the domain updates always being aligned with the grid, which is not suitable for problems involving shear deformations or large rotations. Hence, the material point domain is convected into parallelograms, and an alternative shape function field is constructed. This approach has been called the convected particle domain interpolation (CPDI) technique.

The modified grid shape functions are constructed to be an interpolation of standard grid shape functions at the corners of the particle domain:

$$\mathbf{N}_i(\mathbf{x}) = \sum_{\alpha=1}^{N} \mathbf{N}_\alpha^p(\mathbf{x})\mathbf{N}_i(\mathbf{x}_\alpha^p) \qquad \text{on } \Omega_p \tag{2.21}$$

where $\mathbf{N}_i(\mathbf{x}_\alpha^p)$ is the standard shape function value at a corner of the particle domain, and $\mathbf{N}_\alpha^p(\mathbf{x})$ is the shape function associated with the $\alpha$th corner of the domain of particle $p$. By replacing standard shape functions with modified functions in Eqs. (2.18) and (2.19), the weighting and weighting gradient function can be modified accordingly.

## 2.3. IMPLICIT MATERIAL POINT METHOD

MPM has so far been mostly formulated in an explicit manner, so that it is restricted by the Courant–Friedrichs–Lewy (CFL) condition (a necessary condition for stability with explicit time integration schemes), which causes limitations on the choice of time step size. Meanwhile, the explicit formulation may suffer the problem of inaccuracies for some particular problems, such as during plastic behaviour, as, in each loading/time step, the displacement increment is not strictly determined for a fixed load increment by using an explicit time integration. Hence, errors may accumulate over the time. Increasing the number of the subincrements can of course improve the accuracy, but the computational cost may then become prohibitive. Therefore, many implicit MPM formulations have then been proposed, such as Guilkey and Weiss (2003), Beuth et al. (2011) and Lim (2012). In this section, a unified IMPM framework proposed by the author and his colleagues is provided, within which both quasi-static and dynamic analyses can be solved. The implementation procedure closely follows standard FEM approaches, where possible, to allow easy conversion of other FEM codes. This section aims to provide a clear and straightforward overview of all the necessary techniques for adapting an existing FEM implementation into one based on implicit MPM.

### 2.3.1. UPDATED LAGRANGIAN FORMULATION

Three computational phases are also included in the IMPM formulation, i.e. a mapping phase, UL-FEM phase and convection phase. A detailed introduction of the UL formulation is first introduced as a prequel for the derivation of the IMPM and to identify the differences, as opposed to using a small strain formulation, in solving large deformation problems by use of the UL-FEM formulation.

An important consideration in the computational analysis of large deformation problems is a proper kinematic description. Based on the configuration, all static and kinematic variables in the solution are referred to two formulations within Largrangian methods, these being termed total Lagrangian (TL) and updated Lagrangian (UL). The initial configuration corresponding to time $t = 0$ is used in the TL formulation, while the last calculated configuration is referred to for the UL formulation. Both formulations include all kinematic nonlinear effects due to large displacements, large rotations and large strains. The only advantage of using one formulation rather than the other lies in its greater numerical efficiency (Bathe, 1996).

Assume that the externally applied loads are a function of time, and that the solutions for the static and kinematic variables for all time steps from time 0 to $t$ have been obtained. Then the solution for the next required equilibrium position corresponding to time $t + \Delta t$, where $\Delta t$ is a time increment, is applied repetitively until the complete solution path has been solved for. Using the principle of virtual displacement, where the inertial terms are neglected for simplicity, the equilibrium conditions of a system of fi-

nite elements representing the body under consideration at time $t + \Delta t$ can be expressed as, using the UL-FEM formulation,

$$\int_{\Omega_{e,t}} \mathbf{S}_t^{t+\Delta t} \delta \boldsymbol{\epsilon}_t^{t+\Delta t} d\Omega_{e,t} = \mathbf{R}_{ext}^{t+\Delta t} \tag{2.22}$$

where the superscript $t + \Delta t$ refers to the current configuration, the subscript $t$ is the reference configuration, $\mathbf{S}$ is the second Piola-Kirchhoff stress tensor, $\delta \boldsymbol{\epsilon}$ is the Green-Lagrange strain tensor corresponding to the virtual displacements, $\Omega_{e,t}$ is the element domain at time $t$, and $\mathbf{R}_{ext}$ is the virtual work equaling the external force multiplied by the virtual displacement.

Assuming an incremental procedure, the stress at time $t + \Delta t$ can be considered as an incremental term added to the term at time $t$:

$$\mathbf{S}_t^{t+\Delta t} = \mathbf{S}_t^t + \mathbf{S}_t \tag{2.23}$$

where $\mathbf{S}_t = \Delta \boldsymbol{\sigma}$ is the incremental stress for the period of $\Delta t$. Note that, in the UL-FEM formulation, the stress at the current time step $t$ is basically the Cauchy stress, i.e.

$$\mathbf{S}_t^t = \boldsymbol{\sigma}^t \tag{2.24}$$

where $\boldsymbol{\sigma}^t$ are the known Cauchy stresses at time $t$.

The strain at time $t + \Delta t$ with respect to $t$ is actually the incremental strain,

$$\boldsymbol{\epsilon}_t^{t+\Delta t} = \boldsymbol{\epsilon}_t \tag{2.25}$$

Hence, $\delta \boldsymbol{\epsilon}_t^{t+\Delta t} = \delta \boldsymbol{\epsilon}_t$ and the incremental strain can be decomposed into two parts, $\boldsymbol{\epsilon}_t = \Delta \mathbf{e} + \Delta \boldsymbol{\eta}$, in which $\Delta \mathbf{e}$ is the linear part as commonly used in small strain analysis and $\Delta \boldsymbol{\eta}$ is the high order term, as expressed respectively by,

$$\Delta \mathbf{e} = \frac{1}{2} (\nabla \bar{\mathbf{u}} + (\nabla \bar{\mathbf{u}})^{\mathrm{T}}) \tag{2.26}$$

and

$$\Delta \boldsymbol{\eta} = \frac{1}{2} ((\nabla \bar{\mathbf{u}})^{\mathrm{T}} \cdot \nabla \bar{\mathbf{u}}) \tag{2.27}$$

where $\bar{\mathbf{u}}$ is the incremental displacement.

By taking Eqs. (2.23) and (2.24) for the stress measure and Eqs. (2.26) - (2.27) for the strain measure, and substituting them into the equilibrium equation (2.22), by neglecting high order terms and linearizing it, the governing equation becomes,

$$\int_{\Omega_e} \Delta \boldsymbol{\sigma} \delta \Delta \mathbf{e} d\Omega_e + \int_{\Omega_e} \boldsymbol{\sigma}^t \delta \Delta \boldsymbol{\eta} d\Omega_e = \mathbf{R}_{ext}^{t+\Delta t} - \int_{\Omega_e} \boldsymbol{\sigma}^t \delta \Delta \mathbf{e} d\Omega_e \tag{2.28}$$

A key in the general application of Eq. (2.28) is that an appropriate configuration is referred to, which is due to the fact that the configuration of the body changes continuously in a large deformation analysis and hence entails some important consequences for the development of an incremental procedure. Generally, the incremental stress can be calculated from either the second Piola–Kirchhoff stress and Green–Lagrange strain tensors (see Bathe (1996)), or, as in this thesis, via a rate dependant formulation using

the Jaumann stress rate and velocity strain tensors (Bathe, 1996). For consistency, the stress and strain rates are here shown in incremental form, with the Jaumann stress rate being given by,

$$\Delta \boldsymbol{\sigma}^J = \mathbf{C} \Delta \mathbf{e} \tag{2.29}$$

where $\Delta \boldsymbol{\sigma}^J$ is the Jaumann stress increment and $\mathbf{C}$ is the incremental stress–strain tensor.

Following Bathe (1996), the Cauchy stress increment can then be written as

$$\Delta \boldsymbol{\sigma} = \Delta \boldsymbol{\sigma}^J - \boldsymbol{\sigma}^t \cdot \Delta \boldsymbol{\omega} + \Delta \boldsymbol{\omega} \cdot \boldsymbol{\sigma}^t \tag{2.30}$$

where $\Delta \boldsymbol{\omega}$ is the spin tensor (also called vorticity tensor) increment at time $t$, in which

$$\Delta \boldsymbol{\omega} = \frac{1}{2}[(\nabla \bar{\mathbf{u}}) - (\nabla \bar{\mathbf{u}})^{\mathrm{T}}] \tag{2.31}$$

Substituting Eqs. (2.29) and (2.30) into the equation of motion for small strain, Eq. (2.28), the final equilibrium equation for large deformation analysis is obtained as

$$\int_{\Omega_e} \mathbf{C} \Delta \mathbf{e} \cdot \delta \Delta \mathbf{e} d\Omega_e - \int_{\Omega_e} (\boldsymbol{\sigma}^t \Delta \boldsymbol{\omega} - \Delta \boldsymbol{\omega} \boldsymbol{\sigma}^t) \cdot \delta \Delta \mathbf{e} d\Omega_e + \int_{\Omega_e} \boldsymbol{\sigma}^t \cdot \delta \Delta \boldsymbol{\eta} d\Omega_e = \mathbf{R}_{ext}^{t+\Delta t} - \int_{\Omega_e} \boldsymbol{\sigma}^t \cdot \delta \Delta \mathbf{e} d\Omega_e \tag{2.32}$$

### 2.3.2. SPATIAL DISCRETISATION

By eliminating the virtual displacement terms on both sides of the final governing equation, i.e. Eq. (2.32), the equation can be simplified as a state equation of force equilibrium. Moreover, to solve Eq. (2.32), it must be spatially discretised. MPM discretises a continuum body in the original configuration into a finite set of material points that are tracked throughout the deformation process. The points are selected to represent a material mass and do not have a defined shape. The method solves the equations on the background mesh; hence, this spatial discretisation is undertaken utilising typical finite element methodology, with the major difference being that the integration uses the material points directly.

Taking the first term in Eq. (2.32) as an example, which is basically the linear elastic stiffness term multiplied by the unknown displacement, and using the same method as in FEM, the shape functions and nodal values of displacement are used to approximate the continuum field, i.e. $\bar{\mathbf{u}}$. Using the strain–displacement transformation matrix, $\Delta \mathbf{e} = \mathbf{B}_L \bar{\mathbf{u}}$, and the method of weighted residuals, the stiffness part of the term can be easily transformed into matrix form, i.e.

$$\mathbf{K}_L^t = \int_{\Omega_e} \mathbf{B}_L^{\mathrm{T}} \mathbf{C} \mathbf{B}_L d\Omega_e \tag{2.33}$$

Note that this is the small strain linear elastic stiffness matrix in a standard FEM procedure, where $\mathbf{B}_L$ is the linear strain–displacement transformation matrix.

The integrals of the weak form are then converted into the sums of quantities evaluated at the material points, which yields

$$\mathbf{K}_L^t = \sum_p (\mathbf{B}_L^{\mathrm{T}}(\mathbf{x}_p) \mathbf{C}_p \mathbf{B}_L(\mathbf{x}_p)) V_p^t \tag{2.34}$$

where, for a single element, $p$ is the number of material points within the element, $V_p^t$ refers to the volume of material point $p$ at time $t$ and the shape function differential $\mathbf{B}_L$ is a function of the material point positions $\mathbf{x}_p$, which are updated after each time step.

Similarly, the second and third terms in Eq. (2.32), referring to the non-linear contributions due to the geometry change and Jaumaan stress, are written as (with the displacement part omitted),

$$\mathbf{K}_{NL}^t = \sum_p (\mathbf{B}_{NL}^T(\mathbf{x}_p)\hat{\boldsymbol{\sigma}}_p\mathbf{B}_{NL}(\mathbf{x}_p) - \mathbf{B}_L^T(\mathbf{x}_p)\tilde{\boldsymbol{\sigma}}_p\mathbf{B}_L(\mathbf{x}_p))V_p^t \tag{2.35}$$

where $\mathbf{B}_{NL}$ represents the nonlinear strain–displacement transformation matrix, $\hat{\boldsymbol{\sigma}}_p$ is the Cauchy stress matrix, while the matrix $\tilde{\boldsymbol{\sigma}}_p$, used in the second term of the integrand of $\mathbf{K}_{NL}$, is due to the Jaumann stress.

The internal force, i.e. the last term in Eq. (2.32), at the reference time $t$ and the external force in Eq. (2.32) are respectively expressed as,

$$\mathbf{F}_{int}^t = \sum_p (\mathbf{B}_L^T(\mathbf{x}_p^t)\boldsymbol{\sigma}_p) \cdot V_p^t \tag{2.36}$$

and

$$\mathbf{F}_{ext}^{t+\Delta t} = \sum_p (\mathbf{N}(\mathbf{x}_p^t)\mathbf{b}_p + \mathbf{N}(\mathbf{x}_p^t)\tau^s) \cdot V_p^t \tag{2.37}$$

where $\mathbf{N}(\mathbf{x}_p^t)$ are the shape functions at location $\mathbf{x}_p^t$ at time $t$. Detailed matrix expressions are addressed as following:

(a) Linear strain-displacement transformation matrix:

$$\mathbf{B}_L = \begin{pmatrix} h_{1,1} & 0 & h_{2,1} & 0 & \dots & h_{N,1} & 0 \\ 0 & h_{1,2} & 0 & h_{2,2} & \dots & 0 & h_{N,2} \\ h_{1,2} & h_{1,1} & h_{2,2} & h_{2,1} & \dots & h_{N,2} & h_{N,1} \end{pmatrix}$$

where $h_{k,j} = \frac{\partial N_k}{\partial x_j}$ are the shape function differentials with respect to the Cartesian coordinates $x_j$, and $N$ is the number of nodes.

(b) Non-linear strain-displacement transformation matrix:

$$\mathbf{B}_{NL} = \begin{pmatrix} h_{1,1} & 0 & h_{2,1} & 0 & \dots & h_{N,1} & 0 \\ h_{1,2} & 0 & h_{2,2} & 0 & \dots & h_{N,2} & 0 \\ 0 & h_{1,1} & 0 & h_{2,1} & \dots & 0 & h_{N,1} \\ 0 & h_{1,2} & 0 & h_{2,2} & \dots & 0 & h_{N,2} \end{pmatrix}$$

(c) Cauchy stress matrix:

$$\hat{\boldsymbol{\sigma}}_p = \begin{pmatrix} \sigma_{11} & \sigma_{12} & 0 & 0 & 0 \\ \sigma_{21} & \sigma_{22} & 0 & 0 & 0 \\ 0 & 0 & \sigma_{11} & \sigma_{12} & 0 \\ 0 & 0 & \sigma_{21} & \sigma_{22} & 0 \\ 0 & 0 & 0 & 0 & \sigma_{33} \end{pmatrix}$$

where $\sigma$ refers to the corresponding Cauchy stress.

As mentioned before, an objective stress rate such as the Jaumann stress rate is normally used to include the large rotation effects and, correspondingly, an additional stiffness matrix due to the rotation is then generated.

(d) Rotation matrix:

$$\tilde{\boldsymbol{\sigma}}_p = - \begin{pmatrix} 2\sigma_{11} & 0 & \sigma_{12} & 0 \\ 0 & 2\sigma_{22} & \sigma_{12} & 0 \\ \sigma_{12} & \sigma_{12} & 0.5(\sigma_{11}+\sigma_{22}) & 0 \\ 0 & 0 & 0 & \sigma_{33} \end{pmatrix}$$

After substituting Eqs. (2.34) – (2.37) into Eq. (2.32), the equilibrium equation in matrix form can then be formulated as:

$$\mathbf{K}^t \bar{\mathbf{u}} = \mathbf{F}_{ext}^{t+\Delta t} - \mathbf{F}_{int}^t \tag{2.38}$$

where $\mathbf{K}^t = \mathbf{K}_L^t + \mathbf{K}_{NL}^t$, and is comprised of both linear and nonlinear terms.

### 2.3.3. DYNAMIC FORM

A governing dynamic equation is obtained by adding an inertial term in Eq. (2.38), satisfying Eq. (2.2). Hence,

$$\mathbf{K}^t \bar{\mathbf{u}} + \mathbf{M}^t \mathbf{a}^{t+\Delta t} = \mathbf{F}_{ext}^{t+\Delta t} - \mathbf{F}_{int}^t \tag{2.39}$$

where $\mathbf{M}^t$ is the mass matrix, which, in lumped form, is given by,

$$\mathbf{K}^t \bar{\mathbf{u}} + \mathbf{M}^t \mathbf{a}^{t+\Delta t} = \mathbf{F}_{ext}^{t+\Delta t} - \mathbf{F}_{int}^t \tag{2.40}$$

where $\mathbf{M}_p$ is the material point mass matrix, of size $N_{\text{dim}} \times N_{\text{dim}}$ (where $N_{\text{dim}}$ is the number of dimensions). Following Newmark's (1959) time integration scheme,

$$\mathbf{v}^{t+\Delta t} = \mathbf{v}^t + [(1-\delta)\mathbf{a}^t + \delta\mathbf{a}^{t+\Delta t}]\Delta t \tag{2.41}$$

$$\mathbf{u}^{t+\Delta t} = \mathbf{u}^t + \mathbf{v}^t\Delta t + [(\tfrac{1}{2} - \alpha)\mathbf{a}^t + \alpha\mathbf{a}^{t+\Delta t}]\Delta t^2 \tag{2.42}$$

where $\Delta t$ is the time step, $\mathbf{a}^{t+\Delta t}$, $\mathbf{v}^{t+\Delta t}$ and $\mathbf{u}^{t+\Delta t}$ are the accelerations, velocities and displacements at time $t + \Delta t$, and $\delta$ and $\alpha$ are time stepping parameters which influence the integration accuracy and stability, and are chosen as $\delta = 0.5$ and $\alpha = 0.25$ in the following analyses. The incremental displacement is given by $\bar{\mathbf{u}} = \mathbf{u}^{t+\Delta t} - \mathbf{u}^t$. Hence, substituting Eq. (2.42) into Eq. (2.39) and rearranging, the resulting equation in the form of Eq. (2.38) leads to,

$$(\mathbf{K}^t + \frac{\mathbf{M}^t}{\alpha\Delta t^2})\bar{\mathbf{u}} = \mathbf{F}_{ext}^{t+\Delta t} + \mathbf{M}^t(\frac{1}{\alpha\Delta t}\mathbf{v}^t + (\frac{1}{2\alpha} - 1)\mathbf{a}^t) - \mathbf{F}_{int}^t \tag{2.43}$$

Let $\bar{\mathbf{K}}^t$ represent a modified stiffness matrix, which takes the form $\bar{\mathbf{K}}^t = \mathbf{K}^t + \frac{\mathbf{M}^t}{\alpha\Delta t^2}$, and assume the new external force contains the kinetic terms from the previous time step, i.e.

$$\bar{\mathbf{F}}_{ext}^{t+\Delta t} = \mathbf{F}_{ext}^{t+\Delta t} + \mathbf{M}^t(\frac{1}{\alpha\Delta t}\mathbf{v}^t + (\frac{1}{2\alpha} - 1)\mathbf{a}^t) \tag{2.44}$$

Hence the rewritten governing equation takes the form,

$$\bar{\mathbf{K}}^t \bar{\mathbf{u}} = \bar{\mathbf{F}}_{ext}^{t+\Delta t} - \mathbf{F}_{int}^t \tag{2.45}$$

so that both the dynamic and quasi-static formulations can be solved in the same manner using the Newton–Raphson method.

### 2.3.4. UPDATE OF KINEMATIC VARIABLES

In a quasi-static analysis, after the incremental displacement is obtained by solving the equation of motion, Eq. (2.38), the next step is only to move the material point in accordance with the displacement of the computational grid. However, dynamic analysis involves the solution of Eq. (2.45); in this case, as well as displacements, it is also necessary to update accelerations and velocities. Details of kinematic variable updating are therefore presented in this sub-section. As with the MPM introduced in section 2.2, the kinematic variables need to be updated three times within the IMPM computational cycle.

#### MAPPING PHASE

Kinematic information from the material points needs to be mapped to the grid nodes before proceeding to solve the equations of motion. For completeness, Eq. (2.9) is rewritten here as an illustration of the information transfer between the material points and the background mesh nodes:

$$\mathbf{v}_i^t = \frac{\sum_p N_i(\mathbf{x}_p^t) m_p \mathbf{v}_p^t}{m_i^t} \tag{2.46}$$

#### UPDATED LAGRANGIAN PHASE

For the computation stage, Newton's method is used to calculate the incremental displacement $\bar{\mathbf{u}}_i$ (Eq. 2.45). Solving for velocities and accelerations using Eqs. (2.41) and (2.42), with $\delta = 0.5$ and $\alpha = 0.25$, the two kinematic variables yield,

$$\mathbf{v}_i^{t+\Delta t} = \frac{2}{\Delta t} \bar{\mathbf{u}}_i - \mathbf{v}_i^t \tag{2.47}$$

$$\mathbf{a}_i^{t+\Delta t} = \frac{4}{\Delta t^2} \bar{\mathbf{u}}_i - \frac{4}{\Delta t} \mathbf{v}_i^t - \mathbf{a}_i^t \tag{2.48}$$

#### CONVECTION PHASE

The final stage is to map the information from the grid nodes back to the material points. Accelerations and displacements are directly mapped from the nodes using the shape functions, i.e.

$$\mathbf{a}_p^{t+\Delta t} = \sum_{i=1}^{N_n} \mathbf{a}_i^{t+\Delta t} N_i(\mathbf{x}_p^t) \tag{2.49}$$

$$\bar{\mathbf{u}}_p^{t+\Delta t} = \sum_{i=1}^{N_n} \Delta \bar{\mathbf{u}}_i^{t+\Delta t} N_i(\mathbf{x}_p^t) \tag{2.50}$$

where $N_n$ is the number of grid nodes which provide support to the material point, which in this case is the number of nodes in an element, while, in cases of utilising generalized interpolation MPM (Bardenhagen and Kober, 2004), the nodes of surrounding elements can also be included. The trapezoidal rule is thus used here to update the velocity, i.e.

$$\mathbf{v}_p^{t+\Delta t} = \mathbf{v}_p^t + \frac{1}{2}(\mathbf{a}_p^t + \mathbf{a}_p^{t+\Delta t})\Delta t \tag{2.51}$$

### 2.3.5. Further features in this implementation

In this subsection, the procedures adopted for calculating the damping force and frictional boundary conditions within the IMPM framework are introduced, as well as the update of the volumes of material points.

#### Damping force

Damping is included in the formulation to avoid non-physical vibration in dynamic analyses. It is common to assume the damping matrix to be a function of the linear combination of the mass and stiffness matrices, utilising the so-called "Rayleigh" damping coefficients (Smith and Griffiths, 2005). However, Rayleigh damping is frequency dependent, and hence prior knowledge about the frequency of the system is needed. The approach proposed by Cundall (1987), which involves a local non-viscous damping to overcome the difficulty due to frequency dependence, has been adopted herein. Hence, the damping force on a node is proportional to the magnitude of the out-of-balance forces, with a directional function that ensures that vibrational modes are damped, i.e.

$$\mathbf{F}_{damp,i} = -c_d |\mathbf{F}_i| \, sign(\mathbf{v}_i) \tag{2.52}$$

where $c_d$ is a dimensionless damping factor, $\mathbf{f}_i$ are the nodal resultant forces and $sign(\mathbf{v}_i)$ is the velocity direction.

The choice of damping factor in the analyses is not necessarily easy to define. The factor should be large enough to dissipate any unbalanced energy causing unrealisitic oscillations, but not so large as to cause an overdamped system, which would unrealistically reduce the speed of the slide in slope instability analyses. To achieve a quasi-static equilibrium efficiently, the factor was chosen mostly to be 0.75 in Al-Kafaji (2013); however, for the unsaturated one-point three-phase MPM in Yerro et al. (2015), the factor was chosen to be only 0.05, as it was stated that the drag force between the solid and the fluid introduces an implicit damping force; and in the river levee collapse analysis in Bandara and Soga (2015), the damping force was not considered during the evolution of the failure mechanism, as the plasticity of the material and the viscous effects of the fluid were reported to be sufficient to dissipate the unbalanced energy. Hence, the damping factor is problem/material dependent.

#### Frictional boundary conditions

The interaction between the soil and a non-deforming material outside the domain has been modelled using a Coulomb frictional algorithm. This algorithm is basically a simplified version of the contact algorithm introduced in Bardenhagen et al. (2001).

Initially, a fully fixed boundary condition is applied and the reaction forces on the boundary, $f_{react}$, are calculated and termed trial forces. The tangential component of this force is then compared to the maximum allowable tangential force considering frictional behaviour, i.e. $\mu\max(0, f_{react,n}^{t+\Delta t,tr})$, where $\mu$ is the friction coefficient between the soil and material outside the domain, the superscript $tr$ indicates that this refers to the trial force and the subscript $n$ refers to the normal component. If the trial force exceeds the allowable force, then a slip condition occurs and the allowable force is used as the boundary condition and the increment is re-calculated. This can be expressed as,

$$f_{react,t}^{t+\Delta t} = \begin{cases} \mu\max(0, f_{react,n}^{t+\Delta t,tr}) & if \quad f_{react,t}^{t+\Delta t,tr} > \mu\max(0, f_{react,n}^{t+\Delta t,tr}), i.e.slip \\ f_{react,t}^{t+\Delta t,tr} & otherwise(stick) \end{cases} \tag{2.53}$$

where the subscript $t$ refers to the tangential component of the reaction force.

The trial reaction force can be applied to all the background element nodes attached to the boundary and included in the vector $\mathbf{F}_{react}^{t+\Delta t}$. The trial reaction force at each node, $i$, is then given by

$$\mathbf{F}_{react,i}^{t+\Delta t,tr} = -\mathbf{F}_{ext,i}^{t+\Delta t} + \mathbf{F}_{int,i}^{t} + \mathbf{M}_i \mathbf{a}_i^t \tag{2.54}$$

Further details of the implementation of the frictional algorithm, in particular for slope problems, can be found in Shin (2009) and Bandara (2013).

### UPDATE OF MATERIAL POINT VOLUMES

It is worth noting that material points, though they cannot be defined as explicit, quantitative shapes, do implicitly have sizes (volumes). By adding up these sizes (volumes) together, it approximately equals the continuum size (volume), when numerical errors are taken into consideration.

In the convection phase within a computation cycle, the deformation gradient is calculated in order to update the material point volume using Eq. (2.55):

$$\Omega_p^{t+\Delta t} = J_t^{t+\Delta t}\Omega_p^t \tag{2.55}$$

where $\Omega_p^t$ and $\Omega_p^{t+\Delta t}$ are the volumes calculated for times $t$ and $t+\Delta t$, respectively, and $J_t^{t+\Delta t}$ denotes the Jacobian determinant of the deformation gradient calculated for time $t+\Delta t$ and related to the configuration at time $t$.

For small strain problems, the calculations of the deformation gradient can be approximated by the trace of the strain tensor, i.e. $J = 1 + tr(\boldsymbol{\epsilon})$.

### 2.3.6. FINAL GOVERNING EQUATIONS

Based on the acquired damping force and reaction forces (e.g. from the ground against the slope bottom), a final governing equation for the implicit MPM can be formulated as,

$$\bar{\mathbf{K}}^t\bar{\mathbf{u}} = \bar{\mathbf{F}}_{ext}^{t+\Delta t} - \mathbf{F}_{int}^t + \mathbf{F}_{react}^{t+\Delta t} + \mathbf{F}_{damp}^{t+\Delta t} \tag{2.56}$$

## 2.4. IMPLICIT MPM FOR QUASI-STATIC APPLICATIONS

In the following section, a variety of problems are addressed using the implicit MPM framework defined by Eq. (2.38).

For the computational elements which are not fully filled by material points, an ill-conditioned stiffness matrix may be formed, which could lead to numerical instability. This effect is especially significant when only one material point exists within an element, in particular when it is in or near an element corner. Therefore, an additional material stiffness, of an insignificant magnitude relative to the real material stiffness, is normally assigned to the background mesh, known as a "soft stiffness", in order to improve the numerical stability of the solution.

On the other hand, to achieve a spatially converged solution, i.e. not dependent upon the initial material point positions, a greater number of material points than the Gaussian points is often required. This is due to the changing position of the material points and the non-uniform distribution throughout the computational grid. The influence of the number of material points per element on the numerical results is thus discussed.

### 2.4.1. COLUMN COMPRESSION

A subdivision algorithm is firstly introduced to show the initialisation of the material point positions. A 1-D column compression is then analysed and, by comparing the result with an UL–FEM solution, which is considered to be capable of providing accurate results for large displacement, albeit small strain, problems (Beuth et al., 2011), the good performance of IMPM in solving large deformation problems is demonstrated.



(a) before loading          (b) after loading
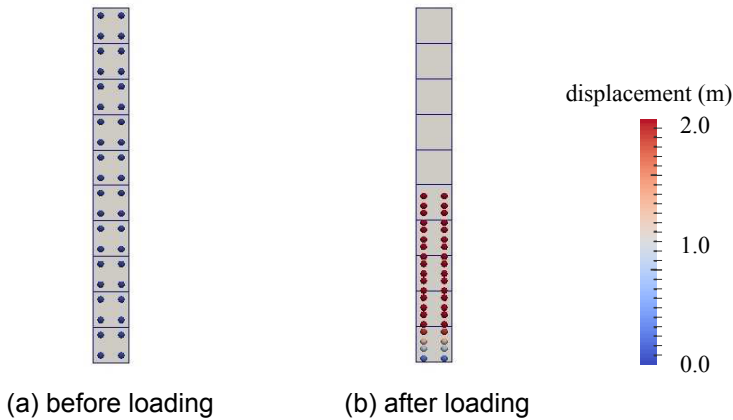
Figure 2.7: 1-D column compression

#### SUBDIVISION ALGORITHM

There are many potential ways to initialise the locations of the material points, such as evenly spaced over the area, using Gauss point positions and so on. Here, the subdivision algorithm introduced in Lim (2012) is chosen. For example, an 8-node quadrilateral parent element with 4 Gauss points is adopted initially, and then, for obtaining more material points, the parent element is subdivided into smaller cells; e.g. into 2 × 2 cells, and

then, by placing the material points on the local Gauss point positions of the small cells, to give a total of 16 material points for the original finite element.

## IMPM SOLUTIONS VERSUS UL–FEM SOLUTIONS

A 10m high column is discretised into a computational grid consisting of ten 8-noded square elements. Within each element 4 material points are initially located at the Gaussian point positions, as shown in Fig. 2.7(a). Both sides of the domain are constrained in the horizontal direction, and the bottom of the mesh is fully fixed. An increasing stress is applied at the top, from 0 to 10 MPa in 40 equal load steps. A plane strain condition is assumed and a linear elastic model employed. The Young's modulus and Poisson's ratio are 10 MPa and 0.3, respectively. After loading, the column is less than half of the original height, as indicated by the closely grouped material points in Fig. 2.7(b).

The stress-strain curve for the one-dimensional compression problem is plotted in Fig. 2.8, alongside UL-FEM results for the same problem. As can be seen, the MPM results correspond well with the FEM solution, although a gradually increasing deviation occurs at larger deformation. This is due to the relatively small number of material points located within each element. As each material point (which is also one of the integration points in the calculation of the stiffness matrix) moves, no matter where it is, the same weighting coefficients are used for the numerical integration which leads to some inaccuracies in the solution. This problem can be alleviated by increasing the number of material points within each element, as in section 2.4.2.
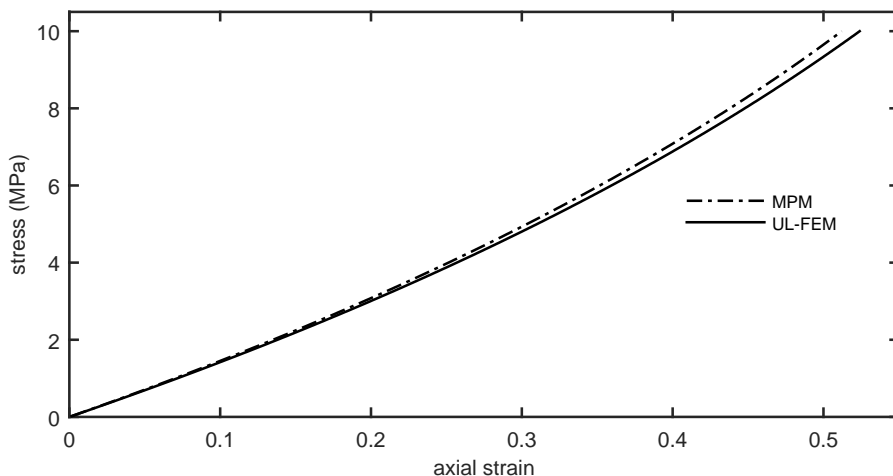


Figure 2.8: Stress-strain curve for 1-D compression

### 2.4.2. CANTILEVER BEAM

A 2-D (i.e. plane strain) linear elastic cantilever beam has been analysed. The beam, as shown in Fig. 2.9, has a length of 1 m, a depth of 0.3 m, a Young's modulus of 100 kPa and a Poisson's ratio of 0. It is built-in along its left edge and its initial configuration is shown in grey, representing the originally filled background mesh. The self-weight was increased from 0 kN/m$^3$ to 4 kN/m$^3$ in 20 loading steps, with each applied increment being equal to 0.2 kN/m$^3$. The analysis used 8-noded quadrilateral elements, with 16 material points being initially located in each element.

In order to increase the numerical stability, a "soft stiffness", as described by Lim (2012), has been assigned to the background mesh, which has been assembled using conventional Gauss point integration of the mesh (i.e. independently of the material points). The ratio of the soft stiffness to the actual stiffness is represented by $\eta$, where $\eta = 0.1$ is applied in this case.
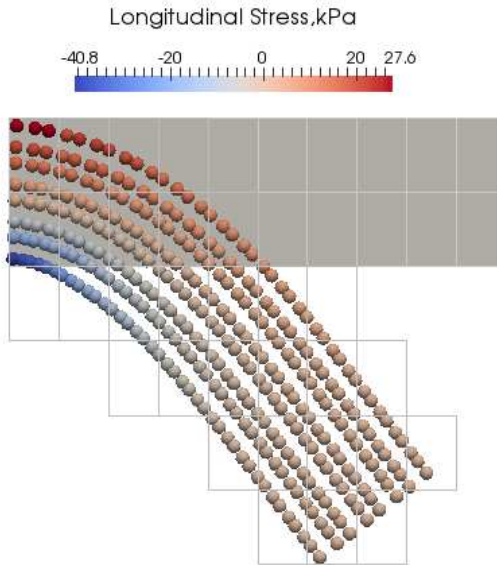


Figure 2.9: Initial and final deformed configurations

The final configuration of the beam is also shown in Fig. 2.9, with the tip displacement (taken from the tracked material point located in the bottom right corner) being –0.38 m and –0.61 m, respectively, in the horizontal and vertical directions. Accordingly, the final activated mesh/elements are shown as a wireframe, which was determined by tracing the material point positions. The colouration of the material points represents the longitudinal stress along the beam, with blue representing compression and red representing tension, ranging from –40.8 kPa (compression) to 27.6 kPa (tension) on the

material points located nearest the fixed end. By using extrapolation, the stresses at the element nodes can be obtained, ranging from –47.5 kPa to 32.0 kPa. UL-FEM solutions are provided here as a direct comparison, where, for the utilised element mesh, the stress range of –47.4 kPa to 32.6 kPa at the fixed end is in good agreement with the MPM solution.

Due to the use of high order elements in the quasi-static code, the potential problems associated with using linear elements, i.e. locking, cell crossing (Bardenhagen and Kober, 2004), etc., are avoided. However, by omitting the inertial terms, the code stability decreases, which leads to the need for more material points and a "soft stiffness" being used. The influences of the number of material points and "soft stiffness" are investigated in the following.

### SOFT STIFFNESS INFLUENCE

The addition of an extra small stiffness across the background mesh is to increase the numerical stability of the code. For example, as a single material point moves near a finite element boundary, the shape function (at the material point) corresponding to the farthest element node may approach zero, while the gradient of the shape function will not be equal to zero; hence it is very hard to get the resultant force on the farthest node converging to zero, thereby leading to a non-convergent analysis. For implicit MPM, the problem normally occurs during the stiffness matrix formation or factorisation, and can lead to an extremely large/unrealistic solution being output, as illustrated by the near vertical dotted line in Fig. 2.10. In the second loading step, the analysis stops due to an extremely large displacement at the beam tip. In contrast, even with a very "soft"/small background stiffness, the outputs are realistic. The results obtained with four different stiffness ratios, i.e. ratio of the soft stiffness to the actual stiffness, of 0.1, 0.01, 0.001 and 0.0001, have been included here, in order to gain a picture of the influence of the "soft stiffness". 16 material points are initially placed in each element.

For comparison with the UL–FEM solution, the vertical tip displacement of the beam (which is taken to be the average vertical displacement of the right-most column of material points near the beam tip) is shown in Fig. 2.10. It is seen that, the higher the stiffness ratio, the greater the error. When the ratio is increased to 0.1, at the final applied load the error relative to the UL solution reaches 0.15, although, for ratios equal to or smaller than 0.01, there is only a small difference in the results. Meanwhile, as the stiffness ratio increases, the code gets more stable. Therefore, for the beam case considered here, a ratio of 0.01 is adopted for all other simulations.

### INFLUENCE OF THE NUMBER OF MATERIAL POINTS PER ELEMENT

By using the subdivision algorithm introduced above, three different numbers of material points per element (in the initial mesh) have been considered, i.e. 4, 16 and 36. The influence of the number of material points has been investigated by comparing the averaged material point displacements across the beam tip with the UL–FEM results. Figs. 2.11 and 2.12 show the relationship between the self-weight and the recorded displacement (horizontal and vertical). It is seen that, with initially 4 material points per element, there is a large divergence from the UL–FEM result, whereas, as the number increases, the differences become negligible, i.e. for 16 and 36 material points per element.
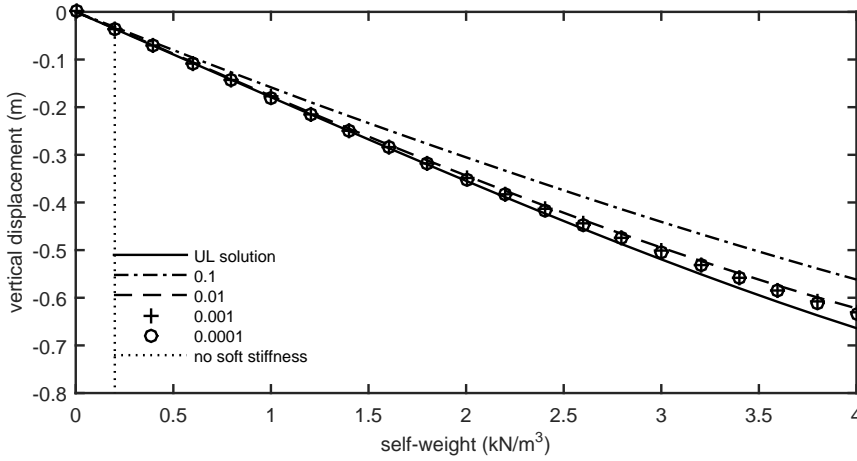
Figure 2.10: Applied load versus tip vertical displacement for different ratios of soft stiffness

By putting more material points within an element, it increases the possibility of material points being distributed over the mesh more evenly, and thus it increases the code stability. However, as the number increases, the computation cost goes up. Hence, a balance has to be made, and here, initially 16 material points per 8-noded element are considered appropriate to analyse the beam.

In terms of generalising the results in this section, it is difficult to determine a priori the appropriate level of discretisation in terms of both the number of elements and number of material points per element. As with standard finite element analysis, good numerical modelling practice is recommended to ensure spatial convergence of the results, i.e. by increasing the level of discretisation and checking the consistency of the results.

## 2.5. IMPLICIT MPM FOR DYNAMIC APPLICATIONS

For the examples presented below, the implicit dynamic method is utilised. Two things are worthy of note: (a) due to the presence of the mass matrix, in which negative terms may arise for high-order elements, low-order elements are here adopted (i.e. a 4-node quadrilateral element in this thesis); (b) as the inertial term is included, initially 4 material points per element are found to be enough for ensuring accuracy when carrying out dynamic analyses and an extra "soft stiffness" is not necessary.

As opposed to the explicit integration method, the implicit time integration algorithm can address time step size restriction, especially for problems with a slow rate of loading, and much computational cost can be saved with little loss in accuracy. The algorithm, which is governed by Eq. (2.45), is tested via two numerical examples within the following section. By utilising a bar vibration example, the influence of the time step
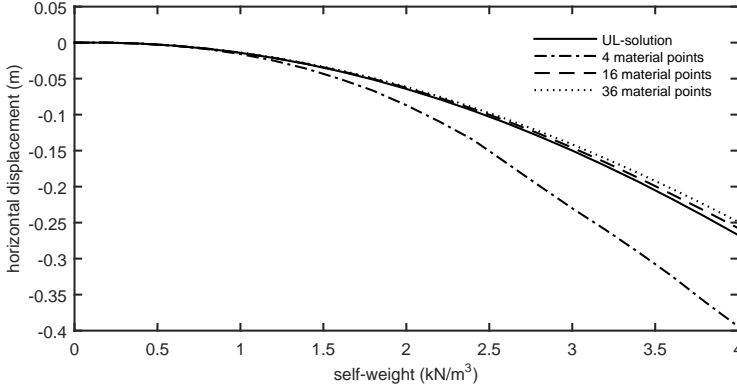
Figure 2.11: Influence of particle density on load–displacement response (horizontal displacement curves)

size is discussed. In the second example, a sand column collapse is performed, with the results being compared to an experiment; this is to further demonstrate the capability of MPM for modeling extreme deformations.

### 2.5.1. AXIAL VIBRATION OF A CONTINUUM BAR

For the vibration of a continuous bar, the case considered here is the same as for a single material point (as in section 2.3.4), but multiple elements have been used. One end ($x = 0$) is fixed, and the other ($x = L$) is free. The bar is found to oscillate in modes, but here only the first mode is considered. The eigenvalue is then $\beta_1 = \frac{\pi}{2L}$, and the frequency of oscillation is related to the eigenvalue $\omega_1 = \beta_1 c$, where $c_v = \sqrt{\frac{E}{\rho}}$ is the wave speed, as before. This gives the analytical solution,

$$v(x, t) = v_0 cos(\omega_1 t) sin(\beta_1 x) \tag{2.57}$$

for velocities and

$$u(x, t) = \frac{v_0}{\omega_1} sin(\omega_1 t) sin(\beta_1 x) \tag{2.58}$$

for displacements, where subscript 1 refers to the first mode. The initial velocities are set to be $v(x, 0) = v_0 sin(\beta_1 x)$ and the displacements are $u(x, 0) = 0$.

The bar is assumed to be of length $L = 1$ m and composed of 10 elements, each equal to 0.1m. In each element, a single material point has been located at the centre of the element. The elastic modulus is $E = 10^4$ Pa and the material density is $\rho = 10^3$ kg/m$^3$. The time step size is set as 0.01 s.

Figure 2.13 presents the comparison between stress updating methods for the 10 element axial vibration analysis. Depending on the order of updating the stress (i.e. at the beginning or at the end of a time step), two different approaches, USF (update stress first) and USL (update stress last), can be distinguished (Bardenhagen and Kober, 2004). It can be seen that, under these conditions, the reduced time step allows for the USL
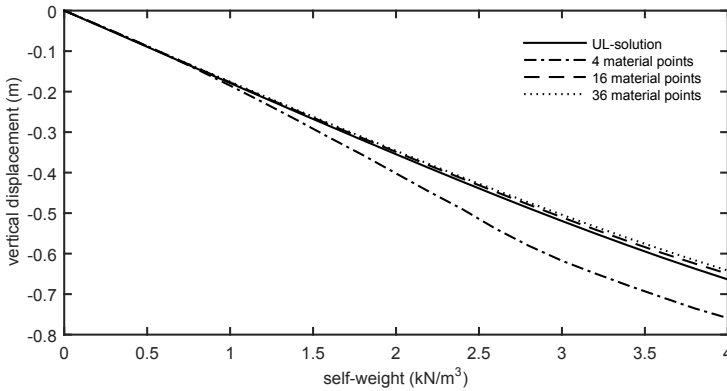
Figure 2.12: Influence of particle density on load–displacement response (vertical displacement curves)

method to almost fully conserve velocity, whereas the USF method still shows energy dissipation.
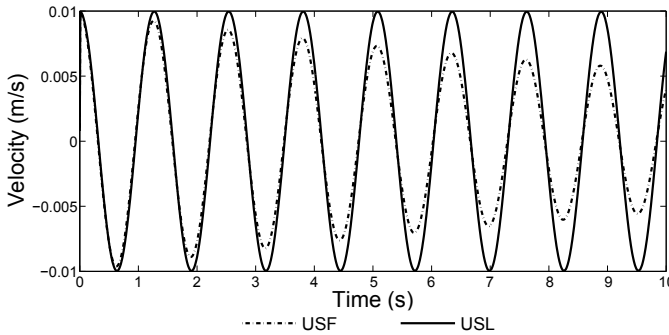


Figure 2.13: Comparison of USL with USF, using 10 element mesh with implicit MPM

Figure 2.14 illustrates the influence of time step size on the variation of velocity when the USF method is utilised, and the analytical solution is provided as a comparison. Three different time-step sizes are set; 0.1, 0.01 and 0.001s, in which the CFL (Courant-Friedrichs-Lewy, a necessary condition for stability with explicit time integration schemes) limit is near 0.01s. It is shown that a poor approximation of the oscillation period and amplitude is depicted with the largest time step, while, with a moderate time step of 0.01s, the period can be captured accurately. When the time step decreases to 0.001s, there are few perceptible differences between the analytical solution and numerical results.

In other words, the program can remain stable even with a large time step size, but energy dissipation and poor approximations may occur. Sulsky and Kaul (2004) also demonstrated that energy dissipation would occur if larger time steps were chosen, but
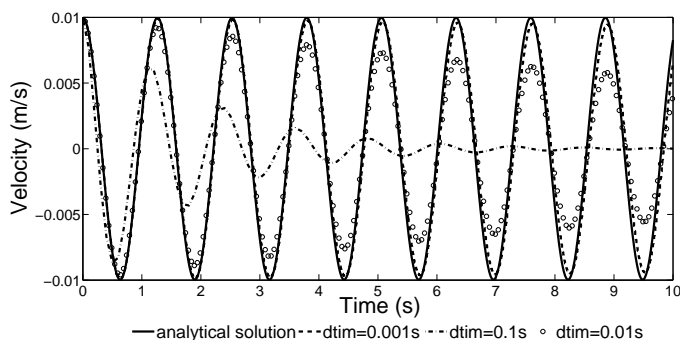
Figure 2.14: Influence of time step size on the velocity variation

that reasonable answers could be still obtained. Hence, initial comparisons of time step sizes based on energy conservation errors are necessary before proceeding with an implicit MPM program.

### 2.5.2. SAND COLUMN COLLAPSE
The following example aims to reproduce the experimental results of Lube et al. (2007), to demonstrate that MPM can be a reliable tool to model the extreme deformations seen in some geotechnical applications.
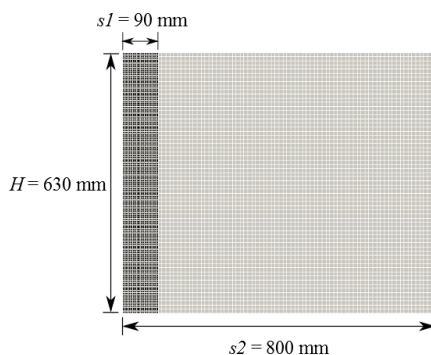


Figure 2.15: Initial column geometry and background domain

As shown in Figure 2.15, the column height is 630 mm and the width is 90 mm. The column is discretized using 4-node square elements, of dimensions 0.01 m × 0.01 m. Four material points are initially placed within each element at the Gauss point positions, so that the simulation is made up of a total of 2268 material points. The light grey background represents the computational domain covering the potential moving trajectories of the material points. The whole simulation is divided into two stages: (1) The lateral boundary conditions are rollers allowing only vertical displacement and the bottom boundary is fully fixed, to allow in-situ stresses due to gravity to be generated; (2) The right side wall is removed to allow the column to collapse from that side. Moreover,

(a) $t = 0.25$ s for the experiment; $t =0.30$ s for the simulation
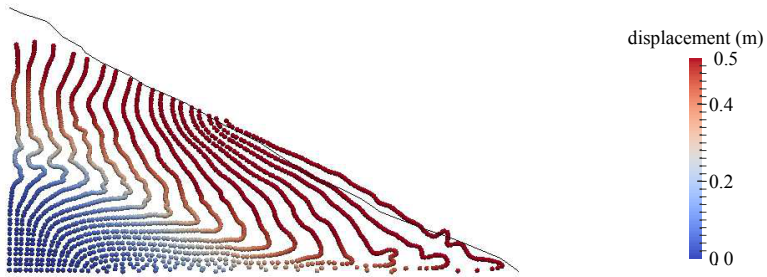


(b) $t = 0.375$ s for the experiment; $t =0.42$ s for the simulation
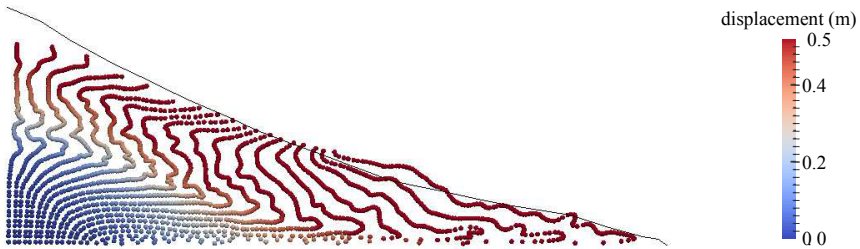


(c) $t = 0.5$ s for the experiment; $t =0.55$ s for the simulation

Figure 2.16: Comparison between MPM computation and experimental result (shown by solid blank line)

the bottom boundary condition is changed to a frictional one to model the interaction between the ground and the column base, as is described in section 2.3.5, and the friction coefficient is set to 0.3. The time step is chosen to be $5.0 \times 10^{-4}$ s.

The sand is modeled as a Mohr-Coulomb material. Material properties are listed in Table 2.1. Note that no porosity was given for the original experiment, although this should not make a difference for the adopted model. The stress update algorithm during the plastic stage follows the procedure of Clausen et al. (2007) to ensure the stress remains on or within the yield surface. Fern and Soga (2016) emphasised the role of constitutive models in modeling column collapses, and concluded that the models can define the volume of the mobilised mass which spreads along the ground. A damping factor of 0.15 is used in the analysis to replicate the energy loss of the sand, which can be attributed to the friction between sand grains during movement.

The material point configurations at three different times are shown in Fig. 2.16. The material points are coloured relative to their initial positions, and the experiment results are represented by continuous lines outlining the surface of the collapsing sand column. It is seen that reasonable agreement is achieved. A discrepancy in time of 0.04 s is shown throughout the simulation, possibly due to the initial release mechanism not being modeled.

| Shear modulus (MPa) | Bulk modulus (MPa) | Cohesion (kPa) | Friction angle (deg) | Dilation angle (deg) | Density (kg/m$^3$) |
|---|---|---|---|---|---|
| 0.323 | 0.7 | 0 | 31 | 1 | 2650 |

Table 2.1: Material properties for sand (after Sołowski and Sloan (2013))

## 2.6. COMPARISONS BETWEEN EXPLICIT MPM AND IMPLICIT MPM

An example of two elastic disks colliding is provided here for a comparison between the explicit and implicit MPM approaches. Two disks with radii equal to 0.2 m are simulated, assuming plane strain conditions. Initially, the two disks are located in the lower left and upper right corners of a square background mesh, as shown in Fig. 2.17(a). The mesh comprises 400 equal-sized square elements of side length equal to 0.05 m. Initial velocities (1.0 m/s, 1.0 m/s) and (–1.0 m/s, –1.0 m/s) are assigned to the two disks, so that they move towards each other along the diagonal of the square. The Young's modulus was 100.0 kPa, the Possion's ratio was 0.3 and the density was 1.0 kg/m$^3$. The simulation was run to a final time of $t = 37.5$ s.

Fig. 2.17 shows the collision process of the two disks, in which the colouration represents the mean stress distribution within the disks. In Fig. 2.17 (a), the initial positions of the two disks are shown. Before impact, due to the constant velocities assigned to the material points, no velocity gradient will be experienced during this phase and hence no stress magnitudes are shown on the disks. Fig. 2.17(b) shows the simulation during the impact, revealing that the material points near the contact region have higher compressive stresses than would be expected. Finally, Fig. 2.17(c) shows the disks after impact,
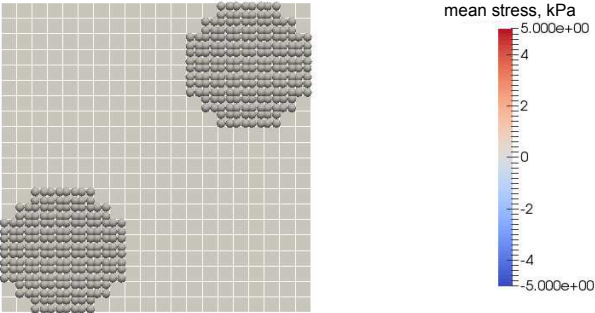
(a) initial locations
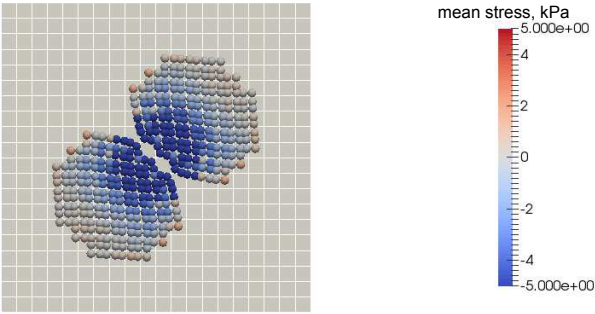


(b) at impact



(c) after impact

Figure 2.17: Collision process of two elastic disks

where the velocities are now in the opposite direction to before the impact. Small residual stresses can be observed on the disks, due to the free vibration of the disks after the impact.

The energy conservation errors of the system were tracked, as a function of time, throughout the analysis. At time $t + \Delta t$ , the total energy of the system can be expressed as

$$E_{tot}^{t+\Delta t} = E_{kin}^{t+\Delta t} + E_{strain}^{t+\Delta t} \tag{2.59}$$

where $E_{kin}$ is the kinetic energy and $E_{strain}$ is the strain energy stored in the material points. These are defined as,

$$E_{kin}^{t+\Delta t} = \frac{1}{2} \sum_p m_p (\mathbf{v}_p^{t+\Delta t})^2 \tag{2.60}$$

$$E_{strain}^{t+\Delta t} = E_{strain}^t + \sum_p V_p^{t+\Delta t} \frac{\boldsymbol{\sigma}_p^t + \boldsymbol{\sigma}_p^{t+\Delta t}}{2} : \Delta \boldsymbol{\varepsilon}_p \tag{2.61}$$

Fig. 2.18 shows the system energy conservation errors with time for different applied time steps, where the initial velocities were changed to 0.005 m/s in order to simulate a longer time during which the two disks remain in contact. Fig. 2.18(a) shows the results using explicit MPM, where the time step was chosen to be $\Delta t = 0.0025$ s by applying the Courant–Friedrichs–Lewy (CFL) condition. The results obtained with the implicit MPM are provided in Fig. 2.18(b) – (d), where time steps were chosen to be the same, 10 times and 100 times that of the explicit code, respectively.

For the cases shown in Fig. 2.18(a) – (c), the energy is preserved well before and after the impact. Before impact, the material points comprising the disks are moving with uniform velocities, and no strains or stresses are generated; hence the energy is purely due to the uniform movement of the disks. During the impact, the kinetic energy decreases to zero, with the strain energy reaching its maximum value at the point of maximum deformation. After that, the disks start to bounce back from each other, and, at the same time, the deformation is recovered, leading to a decrease in the strain energy and a resurgence of kinetic energy. After the impact, a small amount of strain energy remains, which is due to the free vibration of the disks after separation.

Fig. 2.18(d) shows the energy conservation errors corresponding to a time step size of $\Delta t = 0.25$ s, i.e. 100 times the explicit $\Delta t$ . It is seen that the energy not conserved is severe, although the material point trajectories were not much affected. As pointed out by others (e.g. Smith and Griffiths (2005)), implicit integration schemes such as the trapezoidal rule are unconditionally stable in linear analyses, which enables the code to work at extremely large time steps. However, for the problem presented herein, there is a bound on the implicit time step imposed by the accurate resolution of the collision, known as the characteristic collision time, i.e. the time that it takes for a wave to traverse the disk (Sulsky and Kaul, 2004). In this example, the wave speed is about 10.0 m/s, and the disk diameter is approximately 0.4 m, thus giving the characteristic collision time to be about 0.04 s, i.e. 16 times the explicit time step size.
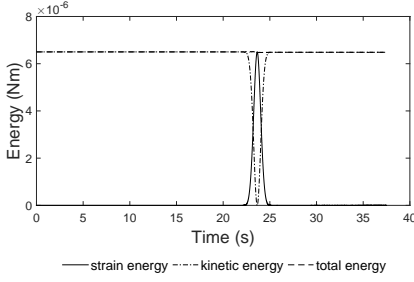
(a) explicit MPM with $\Delta t = 0.0025$ s
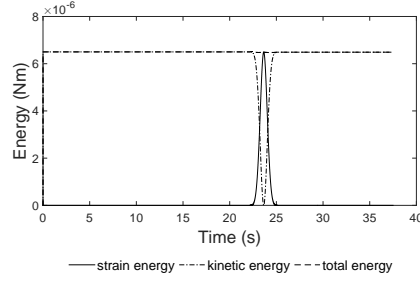
(b) $\Delta t = 0.0025$ s
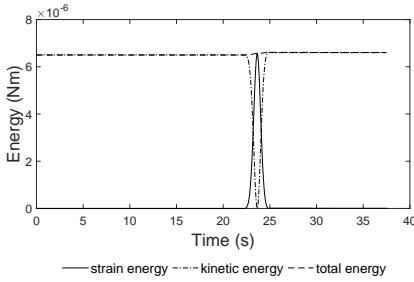
(c) $\Delta t = 0.025$ s
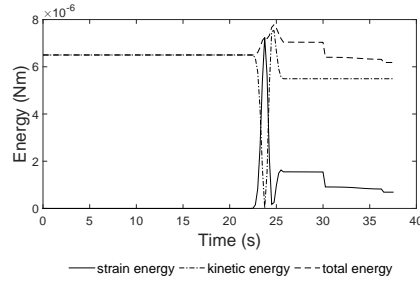
(d) $\Delta t = 0.25$ s

Figure 2.18: Energy conservation errors for elastic disk collision

## 2.7. CONCLUSIONS

An implicit material point method (IMPM) framework has been developed for both quasi-static and dynamic analyses. The improved characteristics in solving large-deformation elasto-plastic problems compared to the finite element method (FEM) are highlighted. The chapter provides a comprehensive overview of the IMPM working procedures and formulation, following, where possible, standard FEM methods, thereby enabling the adaptation of an FEM code to an MPM code in a relatively straightforward manner.

Numerical examples of increasing complexity are provided, so as to clarify and illustrate the implementation procedures, performance and behaviour in a step by step manner. The 1-D column compression introduces the subdivision algorithm adopted in this implementation for the initialisation of material points for the computational continuum. The cantilever beam problem represents a quasi-static case and is used to demonstrate various details of MPM, including the influence of using a "soft stiffness" for the background mesh and the influence of the number of material points per element, and the results are shown to compare favourably with an UL-FEM solution. The dynamic case is illustrated via the axial vibration of a continuum bar and a sand col-

**2**

umn collapse. Aspects, such as the time step size and the order of updating the stress, are investigated in the first example. For the sand column collapse problem, the computed solution is compared with an experimental result, which further demonstrates the capability of MPM in modeling extreme deformations. Finally, a comparison between implicit and explicit MPM models is provided using a disk collision example, where the advantage of using IMPM over explicit MPM in terms of the chosen time step size is identified. Note that if a highly nonlinear constitutive model had been used, then the time step must be selected to ensure an accurate stress return during each loading step, and that therefore the differences between the required time step in the explicit and implicit formulations may be reduced.

# 3

# SLOPE INSTABILITY APPLICATIONS WITH IMPM

*MPM is able to simulate large strain analyses by representing the material as a collection of points which are able to move through a background mesh. By utilising the material point method (MPM) coupled with a cohesive strain softening constitutive model, retrogressive failures within two types of clayey slopes are modelled, which are shown to be in accordance with failure modes observed in reality. Slope geometry is considered to be crucial in the development of slope failure mechanisms, and retrogressive failures are revealed to be closely associated with the post-peak strain softening behaviour of soil. Observations on the collapse process of a long inclined slope reveal that multiple slope slides are occurring simultaneously, and that, based on the slope angle, two types of slope failure can be categorised. For gentler slopes, a retrogressive failure mode, with individual failure blocks forming wedge structures, is observed, whereas, for steeper slopes, a large translational slide is observed, with the soil mass subsequently breaking up.*

## 3.1. INTRODUCTION

Retrogressive and progressive slope failures are a dynamic process in the sense that they involve a progressively changing scenario. A slope, which, when subjected to a toe excavation, becomes unstable, or after an initial failure is steepened, may lead to the initiation of further failures retrogressing backwards. This process can repeat itself in a multiple-retrogressive fashion, and can result in a bigger landslide. Cases reported include the retrogressive failures of cemented sensitive clays in the Ottawa–St. Lawrence Lowlands (Mitchell and Klugman, 1979); retrogressive landslide complexes in the Boone valley in the French Alps (Van Asch et al., 1984); and the progressive failures of observed landslides in Scandinavia and eastern Canada (Locat et al., 2011).

Site investigations on real slope failures provide very valuable information; however, the intervals between individual failures in a larger slide can sometimes amount to some tens of years (Brunsden and Jones, 1980). In most cases of real slope failures, instrumentation of the failure and material characterisation are not undertaken. Hence, for helping to investigate slope failure conditions in a time efficient way, numerical modeling shows certain advantages. A recent publication (Llano-Serna et al., 2015) compares MPM simulation with two real cases, although the only comparison is the final situation, without any observation of the failure and propagation mechanisms.

This chapter presents an investigation of the collapse process of slopes, utilising the implicit material point method (MPM) introduced in the previous chapter, in order to provide a view of how the retrogressive failure develops in the slopes. The whole slope failure process, from initiation, through failure propagation, to the final equilibrium configuration, is simulated.

For convenience in benchmarking this technique, some idealised assumptions are made, but these can easily be changed for more site specific analyses. The simplifying assumptions are: (a) the flow material is a clay idealised by a linear elastic, cohesion strain softening Von Mises model; (b) the slope is assumed to be initially unstable under the in-situ stress condition, so that self-weight is the trigger for the slope failure rather than any other factors; (c) no pore pressure changes are simulated. Hence, a simple total stress approach is adopted in this chapter, with the aim of giving a clear (albeit simplified) picture of some of the main features of slope failure mechanisms in cohesive soils; that is, as a prequel to future investigations involving more realistic material and triggering scenarios. The emphasis here is to reproduce commonly seen clay-type slope failures (Mitchell and Klugman, 1979; Van Asch et al., 1984; Locat et al., 2011) (e.g. rotational and translational slides), and to interpret the failure mechanisms within the proposed framework; that is, to explain the observed translational and rotational slides through the concepts of retrogressive and progressive failure. Comparison of simulations with field cases is beyond the scope of this investigation.

For modeling slope instability, traditional numerical tools such as the finite element method are often limited in their applicability to problems involving large deformations, due to potential excessive mesh distortions that can occur in such cases. This can give an incomplete description of failure, in that the initial slip is considered and the ongoing sliding failure is ignored. That is, continual changes in geometry cannot easily be simulated without extensive re-meshing. However, by using the implicit material point method (IMPM) (Wang et al., 2016c) coupled with a cohesive softening (Von Mises type)

constitutive model, the process of retrogressive failure in an undrained soft clay slope under self-weight loading is possible, as will be demonstrated herein. For this purpose, two types of slope are analysed, which, for convenience, are called "short slope" (slope height = 5.0 m) and "long slope" (down-slope length ≈ 25.0 m). The factors influencing the post-failure and retrogressive failure behaviours of the two slopes have been investigated. For the long slope, different slope angles are considered, to investigate the link between slope geometry and the various failure mechanism categories.

## 3.2. PROGRESSIVE AND RETROGRESSIVE FAILURES IN CLAYS



(a) multiple rotational slips

(b) translational progressive landslide

(c) spread
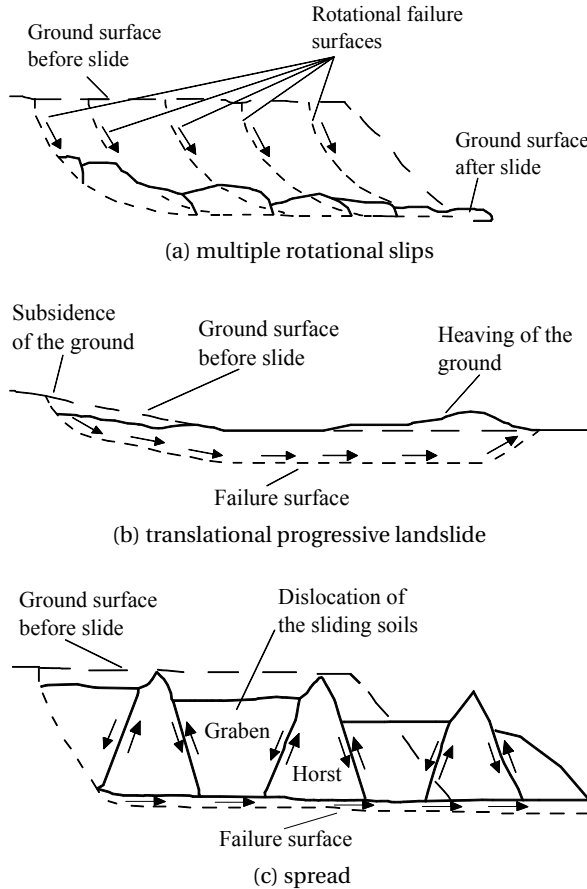
Figure 3.1: Three types of retrogressive landslide in sensitive clay (after Locat et al. (2011)).

Slope failure is a typical geotechnical problem and receives substantial attention due to its potential to cause catastrophic damage. It can be triggered by a variety of factors, such as rainfall infiltration, water level rise, earthquakes and so on. Corresponding failure mechanisms that have been identified, mostly through the back analysis of case histories, are complicated and diverse (Quinn et al., 2007; Bernander, 2000). Generally,

three types of retrogressive landslides in clayey slopes have been summarised (Van Asch et al., 1984; Locat et al., 2011), i.e. multiple rotational slips, translational progressive landslides and spreads, as illustrated in Fig. 3.1.

Multiple rotational slips (or slumps) are believed to happen in a successive way (Xu et al., 2014), following an initial failure which is often due to a long term erosion process. When a down slope failure moves completely away from the newly formed crater, the back scarp is exposed and free, which may result in the scarp itself being an unstable slope and thus another slide occurs. This process can continue until a final stable back scarp is formed. The mechanism of retrogressive failure can be easily recognized in this case, because subsequent failures occur after a block has completely moved out of the sliding area.



(a) shallow sucessive rotational slips



(b) deep seated multiple rotational slips without complete exposure of
the rear scarp
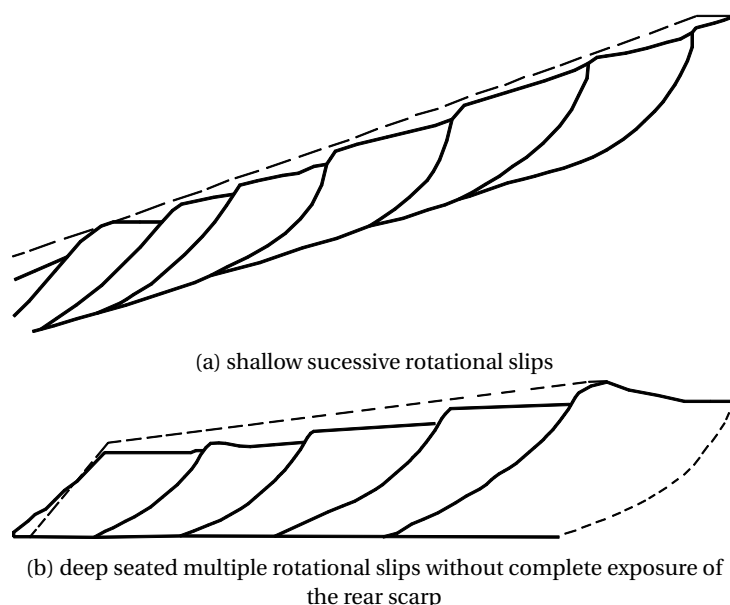
Figure 3.2: Development of rotational slips (after Van Asch et al. (1984)).

There are also examples of slope failure complexes comprising individual failure blocks which have moved very little relative to each other (Van Asch et al., 1984), as shown in Fig. 3.2. The configuration depicted in Fig. 3.2(a) has not necessarily developed by the mechanim of retrogressive failure. Based on plastic static theory, Sokolovskii (1966) has shown that, in long shallow soil slopes, rotational failure planes develop which are linked tangentially to a failure plane parallel to the slope base. The soil above the failure plane can fail as a single block while secondary movements along rotational failure surfaces give the slope a step-like character. Deep seated landslides, as shown in Fig. 3.2(b), are reported to be caused by the mechanism of retrogressive failure (Thomson and Hayley, 1975), although the rear scarp is not completely exposed. In their view, the

slight movement of a block is sufficient to cause a reduction of the lateral support to the upslope soils, hence initiating failure of the next block.

Bjerrum (1955) quantified the danger of successive multiple rotational slumps by considering the stability of one of the single slips, which implicitly assumes that all the slumps behave in a consistently uniform way. It was believed that stabilisation of these slopes could be achieved simply by stabilising the lowest block of the slope (Van Asch et al., 1984).

Translational failures are often found in shallow soil layers, overlaying stiffer and stronger soil or rock layers on long slopes, with a failure plane almost parallel to the topographical surface. The resulting landslides are characterized by a marked subsidence zone at the head of the slope and a heaved passive zone, usually far beyond the toe of the slope, into more level ground (see Fig. 3.1(b); Locat et al. (2011)). Several distinct phases can be concluded in the development of a progressive failure (Bernander, 2000):

– the disturbance phase, in which an initial local instability at the upper part of the slope, such as an earth fill, causes an increase of earth pressure, gradually mobilizing the remaining shear capacity in the potential failure zone;
– an intermediate, virtually dynamic stage of stress redistribution, when the unbalanced shear forces propagate to the more stable, less inclined areas downslope;
– a possible new state of equilibrium, in which, if the maximum earth pressure is less than the current passive earth pressure resistance, the slide movement stops, and the outcome may be a minor local active failure or cracking in the upslope area.
– an actual slide event, in which, if the passive resistance is exceeded over some distance in the lower part of the slope, the soil mass will then disintegrate in a state of passive failure, entailing substantial heave of the ground surface.
– the final state of equilibrium.

Varying material properties and changing geometry in the soil mass in different phases are considered of decisive importance to failure development. A deformation-softening model, in which the shear strength of soils reduces not only due to plastic shear straining, but also due to local failures in the soil masses, was assumed in the work of Bernander (2000) and believed to better describe the extensive failures in a downhill progressive failure. Andresen and Jostad (2004, 2007) further investigated the influences of the material properties on slope failures. By analysing the progressive failure in a long, gently inclined, slope of sensitive clay subjected to undrained loading with a finite element procedure, two different material behaviours (perfect-plasticity and strain softening) were compared. It was concluded that the triggering load for a landslide in strain-softening clay is less than the one for a perfectly-plastic clay with the same shear strength. Moreover, when perfect-plasticity is assumed, the slope fails via a local failure in the upslope area, without any of the failure propagations observed in practice.

Spreads have been proposed to result from the disruption and dislocation of a soil mass above a failure surface (Cruden and Varnes, 1958), beginning at the free surface, and leading to horst and graben type ribs and ridges within slide debris. Odenstad (1951) and Carson (1977) indicate that the angle of the slip surfaces forming the ridges would be at $45° + \phi/2$ to the horizontal, where $\phi$ is the friction angle of the soil. In addition, Carson

(1977) emphasizes the importance of tension crack development between the horsts and grabens and their effects on the morphology of the debris left in the crater. The spread is also postulated to be triggered by an initial instability in the downslope areas, such as toe erosion (Bernander, 2000; Quinn et al., 2007), leading to a loss of lateral support to the soils upslope. The shear strains are mainly concentrated along the surfaces of the horsts and grabens, with minimal strains inside the soil blocks (Dey et al., 2015). The propagation of a horizontal failure surface is considered as another distinct process in forming the spread (Locat et al., 2011, 2013), which underlies and connects the wedge failure blocks. Once the failure surfaces have developed, the horsts and grabens displace almost horizontally along the horizontal shear band, and the failure stops when the subsidence of a graben is not high enough to leave an unstable rear scarp (Carson, 1977). Spreads are believed to occur very rapidly, due to limited time to dissipate the pore pressures in essentially undrained conditions (Locat et al., 2013), and cover larger areas than circular slides. It is even reported that over 42% of the landslides that have happened in Scandinavia can be categorised as spread (Fortin et al., 2008), such as the Sköttorp landslide in Sweden (Odenstad, 1951), and the 1989 Saint-Liguori landslide (see Fig. 3.3; Locat et al. (2011)). Conventional limit equilibrium analyses applied to these types of movements give factors of safety well above unity (Demers et al., 2014). However, the progressive failure mechanism has been put forward, in recent studies, to explain this failure mode. Dey et al. (2013, 2015) simulated the whole process of progressive failure leading to spread by using the coupled Eulerian Lagrangian (CEL) approach, which explained the displacements of different blocks in the failed soil mass and also the remoulding of soil around the shear bands.



Figure 3.3: 1989 landslide at Saint-Liguori, Quebec (Locat et al., 2011)

Many slope collapses can be more complicated, and combine more than one or two of the failure modes listed above. Mitchell and Klugman (1979) described retrogressive

landslide development as a compound failure mode, comprising (a) an initial slip, (b) a retrogressive flow slide owing to the soil strength in the current back scarp being overcome by the gravitational force, and (c) a plastic extrusion process. Quinn et al. (2007) suggested that retrogressive landslides are not in fact retrogressive, but rather the result of translation, subsidence and disruption of a monolithic slide mass over a developing liquefied zone. The Rissa slide, Norway, was reported to be initiated by a retrogressive landslide caused by human activity, characterized by consecutive circular slip surfaces and followed by a big progressive downhill landslide (Gregersen, 1981). The recent Oso landslide in Washington was observed to have multi-rotational retrogressive failures in parts and large translational slides in the longer slopes (Keaton et al., 2014).

For simplicity, this thesis considers an idealized sensitive clayey slope in the following study, where a sharp strength loss is observed once the soil enters the plastic stage, i.e. a simplified strain-softening constitutive model. Andresen and Jostad (2004, 2007) compared the effects of using a strain-softening model with using a perfectly-plastic model in analysing progressive failures in long natural slopes. It was reported that the mechanism for the perfectly-plastic model is local, which highlights the importance of accounting for strain-softening behaviour in slope post-failure assessments.

## 3.3. Constitutive model

This section presents a review of a simple cohesion softening model (after Yap and Hicks (2001)), which is used throughout the thesis. By using different failure criteria, the model is considered to be able to simulate different types of soils, e.g. frictional or clayey soils. For simplicity, Mohr-Coulomb and Von Mises criteria are used in the context of the following analyses. Moreover, the cohesion is considered as a linear function of the accumulated plastic shear strain invariant. Before proceeding to the description of the model, the functions for the two failure criteria are briefly reviewed.

### 3.3.1. Failure criteria

Many failure criteria have been proposed for representing the strength of soils. Among them, the Von Mises and Mohr-Coulomb criteria are often used to describe cohesive (clay) and cohesive-frictional (sand, sandy clay) soil behaviours, respectively, due to their simplicity and the fact that they permit finite element solutions to be compared with a variety of classical plasticity solutions.

To avoid calculating the principal stresses explicitly, which may become complicated for axisymmetric and three-dimensional deformation, the yield fuctions below are expressed in terms of stress invariants. Furthermore, due to the gradient discontinuities which occur at both the edges and apex of the Mohr-Coulomb surface, a smooth hyperbolic approximation (Abbo and Sloan, 1995) is adopted in this work.

#### Von Mises

For undrained clays which behave in a frictionless manner, the Von Mises criterion is appropriate and gives equal weighting to all three principal stresses. Under plane strain conditions, assuming no plastic volume change, the Von Mises criterion is given by,

$$F_{vm} = \sqrt{3}\bar{\sigma} - \sqrt{3}c_u \tag{3.1}$$

where $c_u$ is the undrained shear strength of the soil, and $\bar{\sigma}$ is a stress invariant, equaling the square root of the second devitoric stress invariant, that is,

$$\bar{\sigma} = \sqrt{\frac{1}{2}(s_x^2 + s_y^2 + s_z^2) + \tau_{xy}^2 + \tau_{yz}^2 + \tau_{zx}^2} \tag{3.2}$$

## MOHR-COULOMB

For soils possessing both frictional and cohesive components of shear strength, conical failure criteria are appropriate, the best known of which is the Mohr-Coulomb criterion. In invariant form, the criterion can be written as,

$$F_{mc} = \sigma_m \sin\phi + \bar{\sigma} k_\theta - c \cos\phi \tag{3.3}$$

with

$$k_\theta = \left(\cos\theta - \frac{\sin\theta \sin\phi}{\sqrt{3}}\right) \tag{3.4}$$

where $c$ and $\phi$ are the cohesion and the friction angle of the soil, $\sigma_m$ is the mean stress and $\theta$, called the Lode angle, is a measure of the angular position of the stress point in the $\pi$-plane (Nayak and Zienkiewicz, 1972). These are defined as,

$$\sigma_m = \frac{1}{3}(\sigma_x + \sigma_y + \sigma_z) \tag{3.5}$$

$$\theta = \frac{1}{3}\arcsin(-\frac{3\sqrt{3}}{2}\frac{J_3}{\bar{\sigma}^3}), -30^\circ \le \theta \le 30^\circ \tag{3.6}$$

where $\boldsymbol{\sigma} = (\sigma_x, \sigma_y, \sigma_z, \tau_{xy}, \tau_{yz}, \tau_{zx})^{\mathrm{T}}$ is the Cauchy stress vector, $x$, $y$ and $z$ are the Cartesian coordinates, and $\mathbf{s} = (s_x, s_y, s_z, \tau_{xy}, \tau_{yz}, \tau_{zx})^{\mathrm{T}}$ is the deviator stress vector, with each component being defined as

$$s_x = \sigma_x - \sigma_m, s_y = \sigma_y - \sigma_m, s_z = \sigma_z - \sigma_m \tag{3.7}$$

$J_3$ is the third stress invariant,

$$J_3 = s_x s_y s_z + 2\tau_{xy}\tau_{yz}\tau_{zx} - s_x\tau_{yz}^2 - s_y\tau_{zx}^2 - s_z\tau_{xy}^2 \tag{3.8}$$

To eliminate the singularities at the apex and edges, the yield surface is rounded by introducing two extra parameters, which govern the accuracy of the approximation; details can be found in Abbo and Sloan (1995). Specifically, the yield function is modified as

$$F_{mc} = \sigma_m \sin\phi + \sqrt{\bar{\sigma}^2 k_\theta^2 + a^2 sin\phi^2} - c\cos\phi \tag{3.9}$$

in which parameter $a$ can be adjusted to model the Mohr-Coulomb yield function as closely as desired, as shown in Fig. 3.4, although, in practice, $a = 0.05c\cot\phi$ has been found to give results which are almost identical to those obtained from the Mohr-Coulomb model. If $a$ is set to zero, the traditional Mohr-Coulomb yield function is recovered.
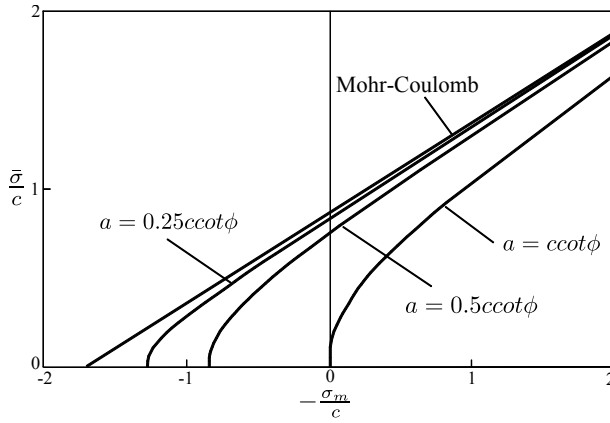
Figure 3.4: Hyperbolic approximation to Mohr-Coulomb meridional section (after Abbo and Sloan (1995))

In Eq. (3.9), $k_\theta$ is similar to the original Mohr-Coulomb definition in Eq. (3.4), except that it is rounded in the vicinity of the singularities, yielding

$$k_\theta = \begin{cases} (A_1 - B_1 \sin 3\theta), & |\theta| > \theta_T \\ (\cos\theta - \frac{1}{\sqrt{3}} \sin\phi \sin\theta), & |\theta| \leq \theta_T \end{cases} \tag{3.10}$$

where

$$A_1 = \frac{1}{3} \cos\theta_T (3 + \tan\theta_T \tan 3\theta_T + \frac{1}{\sqrt{3}} sign(\theta)(\tan 3\theta_T - 3\tan\theta_T) \sin\phi) \tag{3.11}$$

$$B_1 = \frac{1}{3\cos 3\theta_T} (sign(\theta) \sin\theta_T + \frac{1}{\sqrt{3}} \sin\phi \cos\theta_T) \tag{3.12}$$

$$sign(\theta) = \begin{cases} +1, & for \quad \theta > 0^\circ \\ -1, & for \quad \theta \leq 0^\circ \end{cases} \tag{3.13}$$

where $\theta_T$ is a specified transition angle, in which a typical value of $25^\circ$ is used in practice (Abbo and Sloan, 1995).

### 3.3.2. FORMULATION OF THE SOFTENING MODEL

During plastic flow, the current stress coincides with the current yield stress and the value of the yield function remains constant, i.e.

$$F(\boldsymbol{\sigma}, \kappa) = 0 \tag{3.14}$$

where the scalar yield function is a function of the stress tensor, $\boldsymbol{\sigma}$, and the internal hardening/softening parameter, $\kappa$.

As the consistency condition applies, the rate of $F$ vanishes whenever plastic yielding occurs (both hardening and softening), and can be described as

$$dF = \left\{ \frac{\partial F}{\partial \boldsymbol{\sigma}} \right\}^{\mathrm{T}} d\boldsymbol{\sigma} + \frac{\partial F}{\partial \kappa} d\kappa = 0 \tag{3.15}$$

Defining the modulus $A$ as

$$A = -\frac{1}{d\lambda} \left\{ \frac{\partial F}{\partial \kappa} d\kappa \right\} \tag{3.16}$$

where $d\lambda$ is a scalar defining the magnitude of the plastic strain increment, the yield function rate can alternatively be written as

$$dF = \left\{ \frac{\partial F}{\partial \boldsymbol{\sigma}} \right\}^{\mathrm{T}} d\boldsymbol{\sigma} - A d\lambda = 0 \tag{3.17}$$

Note that $A$ is defined in such a way that it is positive when the soil is hardening and negative when the soil is softening.

Rearranging in terms of $d\lambda$ leads to

$$d\lambda = \frac{\left\{ \frac{\partial F}{\partial \boldsymbol{\sigma}} \right\}^{\mathrm{T}} \mathbf{D}^e d\boldsymbol{\varepsilon}}{A + \left\{ \frac{\partial F}{\partial \boldsymbol{\sigma}} \right\}^{\mathrm{T}} \mathbf{D}^e \left\{ \frac{\partial Q}{\partial \boldsymbol{\sigma}} \right\}} \tag{3.18}$$

where $\mathbf{D}^e$ is the elastic stiffness matrix, $d\boldsymbol{\varepsilon}$ is the incremental strain, $Q$ is the plastic potential function, which is regarded the same as the failure function in expressions for an associated flow rule, $\partial F/\partial \boldsymbol{\sigma}$ is the vector normal to the yield surface and $\partial Q/\partial \boldsymbol{\sigma}$ is the vector normal to the plastic potential surface.

The elasto-plasticity is described by introducing the elasto-plastic stress-strain matrix, i.e.

$$d\boldsymbol{\sigma} = \mathbf{D}^{ep} d\boldsymbol{\varepsilon} \tag{3.19}$$

where the elasto-plastic stiffness matrix can be obtained from,

$$\mathbf{D}^{ep} = \mathbf{D}^e - \mathbf{D}^p \tag{3.20}$$

in which $\mathbf{D}^p$ is the plastic stress-strain matrix, given by

$$\mathbf{D}^p = \frac{\mathbf{D}^e \left\{ \frac{\partial Q}{\partial \sigma} \right\} \left\{ \frac{\partial F}{\partial \sigma} \right\}^{\mathrm{T}} \mathbf{D}^e}{A + \left\{ \frac{\partial F}{\partial \sigma} \right\}^{\mathrm{T}} \mathbf{D}^e \left\{ \frac{\partial Q}{\partial \sigma} \right\}} \tag{3.21}$$

The equivalent accumulated plastic strain, in its incremental form, is

$$d\bar{\varepsilon}^p = \sqrt{\frac{2}{3} d\boldsymbol{\varepsilon}^p : d\boldsymbol{\varepsilon}^p} = \sqrt{\frac{2}{3}} \left\| d\varepsilon^p \right\| \tag{3.22}$$

in which $d\boldsymbol{\varepsilon}^p$ is the plastic strain increment, which is normal to the plastic potential surface, i.e.

$$d\boldsymbol{\varepsilon}^p = d\lambda \left\{ \frac{\partial Q}{\partial \boldsymbol{\sigma}} \right\} \tag{3.23}$$

Substituting Eq. (3.23) into Eq. (3.22) leads to

$$d\bar{\varepsilon}^p = \frac{2}{3} d\lambda \sqrt{dQ} \tag{3.24}$$

where,

$$dQ = \frac{1}{2} \left( \left( \frac{\partial Q}{\partial \sigma_x} - \frac{\partial Q}{\partial \sigma_y} \right)^2 + \left( \frac{\partial Q}{\partial \sigma_y} - \frac{\partial Q}{\partial \sigma_z} \right)^2 + \left( \frac{\partial Q}{\partial \sigma_z} - \frac{\partial Q}{\partial \sigma_x} \right)^2 + \frac{3}{4} \frac{\partial Q}{\partial \tau_{xy}}^2 \right) \tag{3.25}$$

Hence, $d\lambda$ is given by

$$d\lambda = \frac{3d\bar{\varepsilon}^p}{2\sqrt{dQ}} \tag{3.26}$$

As the cohesion varies with plastic strain, it can be taken as an internal variable in the yield function as shown in Eq. (3.14), i.e. $dc = d\kappa$. In the model, the stress-strain relationship in the softening stage is assumed to be linear and given by,

$$c(\bar{\varepsilon}^p) = c_0 + H \cdot \bar{\varepsilon}^p; \quad \bar{\varepsilon}^p < \bar{\varepsilon}_{pr} \tag{3.27}$$

$$c(\bar{\varepsilon}^p) = c_r; \quad \bar{\varepsilon}^p > \bar{\varepsilon}_{pr} \tag{3.28}$$

where $c_0$ is the initial cohesion, $c_r$ is the residual cohesion, $\bar{\varepsilon}_{pr}$ is the plastic deviatoric strain invariant at the onset of the residual strength and $H$ is the softening modulus (which is taken to be negative). A sketch of the model is shown in Fig. 3.5. Note that hardening behaviour can easily be included by taking $H$ to be positive.
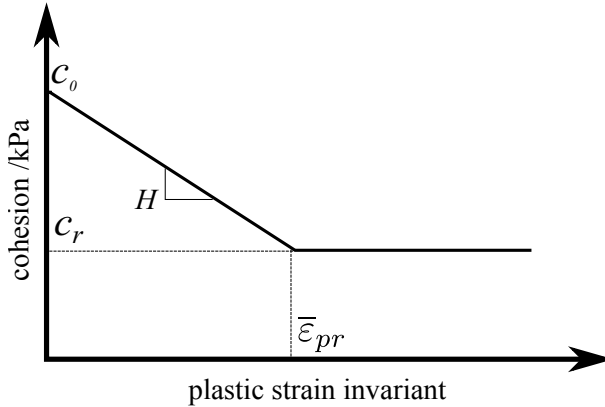


Figure 3.5: Sketch of cohesion softening model

Thus, the change in internal variables can be expresses as,

$$d\kappa = dc = H \cdot d\bar{\varepsilon}^p \tag{3.29}$$

By substituting Eqs. (3.26) and (3.29) into Eq. (3.16), modulus $A$ is then given as,

$$A = -\frac{2}{3}\sqrt{dQ} \cdot H \cdot \frac{\partial F}{\partial \kappa}$$

(3.30)

The partial derivative of the yield function with respect to the internal variable $\kappa$ can be calculated directly using the Eqs. (3.1) and (3.3); for the Von Mises criterion,

$$\frac{\partial F}{\partial \kappa} = \frac{\partial F}{\partial c} = -\sqrt{3}$$

(3.31)

and for the Mohr-Coulomb criterion,

$$\frac{\partial F}{\partial \kappa} = \frac{\partial F}{\partial c} = -\cos\phi$$

(3.32)

Therefore, the final expression for $A$ can be explicitly expressed as a simple function of the input softening parameter; for the Von Mises criterion,

$$A = \frac{2}{3} \cdot \sqrt{dQ} \cdot \sqrt{3}H$$

(3.33)

and for the Mohr-Coulomb criterion,

$$A = \frac{2}{3} \cdot \sqrt{dQ} \cdot H \cdot \cos\phi$$

(3.34)

### 3.3.3. NUMERICAL EXAMPLE

To validate the above softening model, the axisymmetric loading of a single 8-noded quadrilateral element is provided here as an example, as shown in Fig. 3.6. The specimen is 1m high and 1m wide. Both the left and bottom boundaries are on rollers, while the bottom left corner is fixed. It is subjected to vertical displacement-controlled compression on top of the specimen. A total of 110 equal displacement loading-steps are applied, with every step being $-5.0 \times 10^{-5}$m. The material properties are listed in Table 3.1 and the Von Mises failure criterion is used. For the stress integration, an elasto-plastic algorithm has been used, following the approach used by Smith and Griffiths (2005) in which the constitutive equation, Eq. (3.19), is first solved with an initial elastic trial. The stress states at the material points are then checked to determine whether the stress state is allowable, or yield has occurred. A sub-stepping algorithm (Sloan et al., 2001, 2002) has been used to re-distribute stresses and ensure that all stress states are within, or on, the yield surface.

The model results are shown in Fig. 3.7. Four different stages are shown; i.e. linear elastic, linear plastic hardening, linear plastic softening and residual stages. For comparison, models with a perfectly plastic failure criterion are also shown. The results correspond to the analytical solutions.

By combining the proposed strain-softening model with various failure criteria, the studies in this thesis aim to give a clear picture of some of the main geometric features of slope failures. For simplicity, the hardening stage has been omitted in these analyses.
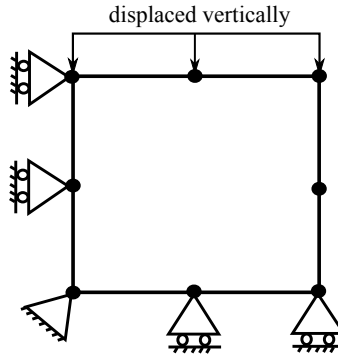
Figure 3.6: Diagram of the numerical example

| Parameters | Values |
|---|---|
| Young's modulus (kPa) | $2.5 \times 10^4$ |
| Poisson's ratio | 0.25 |
| Initial cohesion (kPa) | 16.0 |
| Peak cohesion (kPa) | 20.0 |
| Residual cohesion (kPa) | 15.0 |
| Hardening modulus (kPa) | $5.0 \times 10^3$ |
| Softening modulus (kPa) | $-2.5 \times 10^3$ |

Table 3.1: Parameters for an undrained triaxial compression test

## 3.4. SLOPE COLLAPSE DUE TO AN EXCAVATION AT THE SLOPE TOE

A slope collapse triggered by an excavation in the slope toe area is performed in this section, which provides a preliminary insight into retrogressive and progressive slope failures.

Excavations at the toe of a slope can trigger the collapse of the slope. As well as changing the slope geometry, it may also expose significant geologic features such as shear zones, faults and folds in some circumstances, thereby causing slope instability.

To investigate the effect of excavation on a slope, a naturally stable slope was first considered, as shown in Fig. 3.8, and then a vertical cut of height 0.2 m was excavated at the slope toe, as indicated. The problem is assumed to be plane strain, and the computational grid is made up of 4-noded square elements, of 0.05 m side length, with each element initially containing 4 material points. The height of the slope is 1 m and the slope angle is $45°$. Roller boundaries are prescribed at the left side of the domain, to allow only vertical displacements. The interaction between the slope base and the ground is modelled using the frictional boundary condition (Eq. 2.53), which allows the slope base to move horizontally when friction is overcome.

The linear elastic, cohesion softening Von Mises model, as shown in Fig. 3.5, was used to describe the soil behaviour. $c_0$ is the initial cohesion, $c_r$ is the residual cohe-
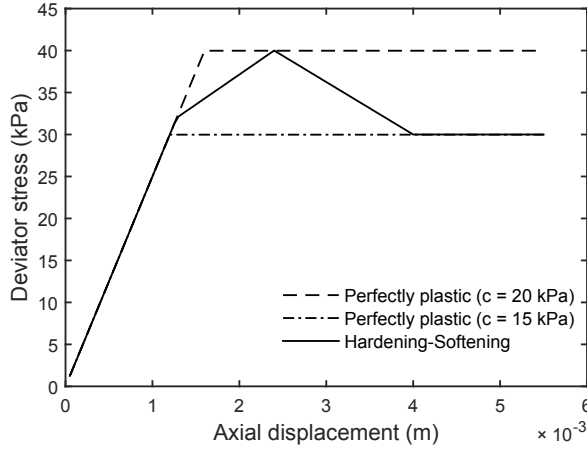
Figure 3.7: Deviator stress versus axial displacement
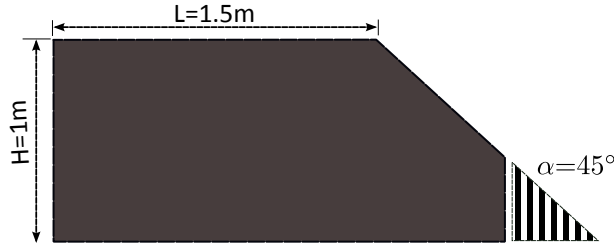


Figure 3.8: Sketch of an excavation undertaken at the toe of a slope

sion, $\bar{\varepsilon}_{pr}$ is the plastic deviatoric strain invariant at the onset of the residual strength and $H$ is the softening modulus (which is taken to be negative for softening). The material properties are shown in Table 3.2. Since a local softening model is used here for demonstrating the proposed solution procedure, the numerical results are mesh dependent. However, as the proposed method is based on a FEM formulation, the same regularisation techniques as used in FEM (Sluys et al., 1993) are likely to be able to address this issue. Note that some regularisation techniques often used in FEM, for example, the addition of higher order gradients, can be more difficult to implement within the MPM framework. Hence, particular attention is needed during the implementation.

The dynamic implicit MPM was utilised in this case. The time step was set as $5.0 \times 10^{-3}$ s, and the computation was divided into two stages. Initially, the self-weight of $\gamma_z = 20$ kN/m$^3$ is applied to the slope in one step to generate the initial total stresses. Quasi-static equilibrium is detected by using the criterion based on the energy and force ratio (Al-Kafaji, 2013), with the out of balance force ratio expressed as,

| Parameters | Values |
|---|---|
| Young's modulus (kPa) | 200.0 |
| Poisson's ratio | 0.33 |
| Self weight (kN/m$^3$) | 20.0 |
| Peak cohesion (kPa) | 5.0 |
| Residual cohesion (kPa) | 1.0 |
| Softening modulus (kPa) | -50.0 |

Table 3.2: Parameters for the excavation case

$$\delta_1 = \frac{\left\| F^{ext} - F^{int} \right\|}{\left\| F^{ext} \right\|} \tag{3.35}$$

and a dimensionless energy ratio as,

$$\delta_2 = \frac{E_{kin}}{W^{ext}} \tag{3.36}$$

where $E_{kin}$ denotes the kinetic energy of the system, $W^{ext}$ is the work induced by the external force, and a tolerance of 0.01 was used for both criteria. To achieve the quasi-static equilibrium state, a damping force needs to be introduced to model the energy loss that occurs in reality (Eq. 2.52). For this case, the factor is chosen as $c_d = 0.75$ to obtain faster convergence in the quasi-static equilibrium stage. Secondly, the triangular soil block was "excavated" instantly to trigger the slope collapse. The collapse process is illustrated in Fig. 3.9, with the colouration representing the accumulated plastic strain invariant $\bar{\varepsilon}^p$ .

Due to the toe excavation, the slope becomes unstable and a slope slide was triggered. In Fig. 3.9(a), a complete shear band, starting from the new slope toe was formed. Fig. 3.9(b) shows that the soil above the shear band moves as a block along the failure surface, and the final quasi-static configuration is displayed.

This analysis illustrates the ability of the proposed method to simulate geotechnical behaviour at large strains, which generally occur in arbitrary directions, i.e. not aligned with the mesh. The consequence of a geotechnical instability can then be better quantified, as can further potential unstable situations, as may be observed, for example, in retrogressive and progressive failures, which will be investigated in the next two sections.

## 3.5. RETROGRESSIVE FAILURE OF A SHORT SLOPE UNDER SELF-WEIGHT LOADING

A relatively short cohesive soil slope has first been analysed using IMPM, combined with the cohesive softening constitutive model. Parametric studies based on the softening modulus and residual strength are provided at the end of the section.

### 3.5.1. RETROGRESSIVE FAILURES WITHIN A SHORT SLOPE
Fig. 3.10 shows the initial geometry of the slope. It has a height of 5 m and a slope angle of 45°, and the distance from the crest to the left-hand boundary is 10.0 m. The

(a) shear band formed due to toe excavation



(b) final configuration of the collapsed slope
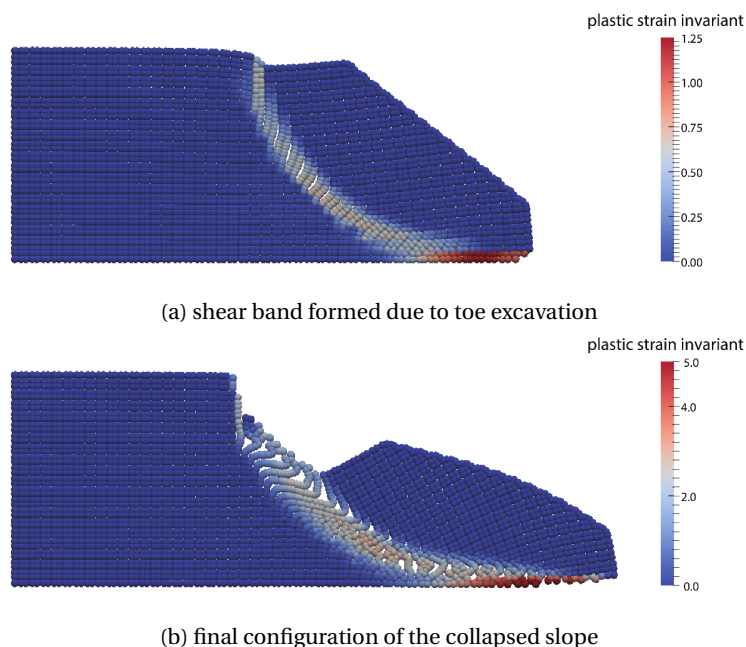
Figure 3.9: Evolution of slope failure due to excavation at the toe

material properties are shown in Table 3.3. These values are hypothetical and do not represent a real case, although they are representative of a soft clay material. The chosen elastic parameters do not cause significant deformation, with the majority of the deformation due to plastic yielding. The problem is assumed to be plane strain. The boundary conditions are rollers on the left-hand edge allowing only vertical movement, and the interaction between the slope base and the underlying ground is modelled using the Coulomb frictional algorithm from Section 2.3.5, with the friction coefficient set to 0.3. The computational grid is made up of 4-node quadrilateral elements, with each element initially having 4 material points located at the Gauss point positions. The background computational mesh is shown as light grey squares in Fig. 3.10, and consists of 20 elements vertically and 80 horizontally. There are 4040 material points. The time step is set as $5.0 \times 10^{-3}$ s. The simulation was run until a final quasi-static equilibrium state was reached. Using an Intel Xeon E5-1620 processor, the analyses take approximately 3-4 hours to execute on a single core.

Fig. 3.11 illustrates the collapse process and development of retrogressive failures within the slope, with the locations of the material points indicating the displaced soil and the coloured contours representing the accumulated plastic shear strain invariant. The static factor of safety (FOS) of the slope is 0.96, as determined using the strength reduction method (Smith and Griffiths, 2005). Gravity loads are applied as body loads on the material points in a single increment and kept constant. To determine the FOS, the strength reduction method has been used to gradually reduce the shear strength until plastic strains are indeterminate and the algorithm fails to converge, at which point the
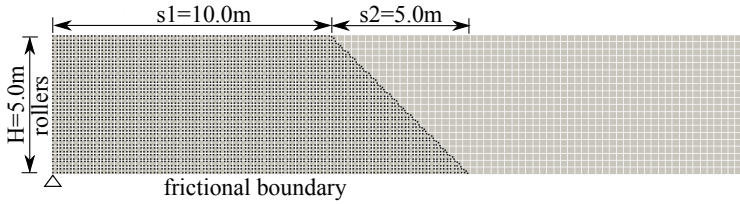
Figure 3.10: Initial conditions of the slope

| Parameters | Values |
|---|---|
| Young's modulus (kPa) | 1000 |
| Poisson's ratio | 0.33 |
| Self weight (kN/m$^3$) | 20.0 |
| Peak cohesion (kPa) | 20.0 |
| Residual cohesion (kPa) | 4.0 |
| Softening modulus (kPa) | -50.0 |

Table 3.3: Material properties for the short slope analysis

strength reduction factor is interpreted as the FOS. For simplicity, an initially unstable slope is considered; hence, self-weight loading is here considered to initialise the slope failure.

An initial band of plastic shear strains can be seen initiating from the slope toe in Fig. 3.11(a). The band then propagates backwards and upwards, so that a complete slip surface is formed soon afterwards, as shown in Fig. 3.11(b). It is observed that the body of soil above the critical slip surface starts to slide along the surface, and that a second slip plane, also originating from the slope base, forms the second failure block. The remaining part of the slope remains largely intact, i.e. elastic. Fig. 3.11(c) clearly shows that plastic strains (and therefore strain softening) are concentrated along the slip surfaces, and that the sliding soil moves as discrete blocks. Formations of soil wedges with shapes of graben and horst are shown in Fig. 3.11(d), where, apart from the two distinct failure planes, the failure propagates in the horizontal direction as well, forming the wedge base. This is in accordance with the previous conceptual model of Odenstad (1951) in explaining the retrogressive failure mechanism, where a horizontal weak plane/layer is assumed. However, in this case it is the strain softening that causes the "weak layer". As time progresses, the retrogression continues to move backwards and upwards and, after approximately 40 s, the exposed back behind the second slide has become large enough so that, due to the removal of down-slope support, it becomes unstable and the third slide is triggered, as shown in Fig. 3.11(e). Unlike the second slide, the block of almost intact clay displaces laterally on the horizontal plane. The final stable configuration is displayed in Fig. 3.11(f), once the three failure blocks have formed. By observing and comparing the successive slides, it can be noticed that, as the failure propagates backwards, the time interval between successive slides becomes larger.

(a) $t = 1.5$ s

(b) $t = 2.5$ s

(c) $t = 3.75$ s

(d) $t = 22.5$ s

(e) $t = 40.5$ s

(f) $t = 73.5$ s
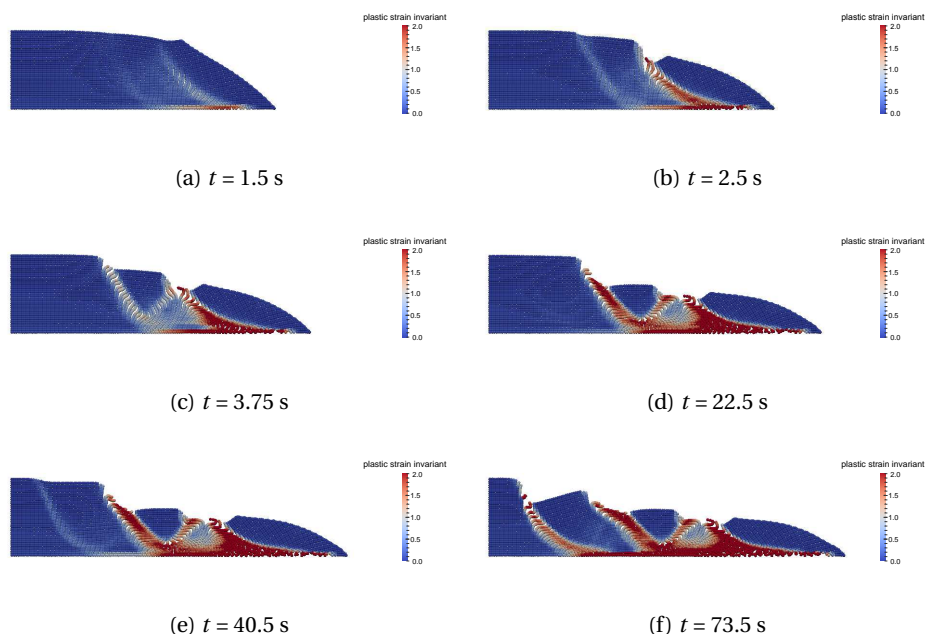
Figure 3.11: Collapse process of a short soft clayey slope

Fig. 3.12 depicts the stages of the constitutive model governing the behaviour of the material points within the slope. Hence, blue, light blue, grey and red colours indicate elastic, elastic unloading, softening and residual stages of the model, respectively. By identifying the stage that each material point is associated with at different times, these plots provide a clear view of the retrogressive failure phenomenon. It can be seen that the strength loss does not occur simultaneously throughout the slope, but according to the stress state and the accumulated plastic strain. When forming a distinct slip surface, material points within the shear band are seen to lose their strength very quickly, after which their response is governed by the residual cohesion. Material points in the immediate vicinity of the shear band are mostly softening, which decreases the soil strength and thereby perpetuates the retrogression of the failure mechanism back into the slope. Large changes in the plastic strain invariant are also seen at the slope base, which experiences the formation of a horizontal weak plane governed by the residual soil strength. In contrast, the soil that is remote from the shear band (mostly near the left-hand boundary or above the critical surface) remains intact. During the failure evolution process, there are two observations worthy of note: firstly, when a block of soil moves out of the sliding area, the exposed soil at the back scarp experiences elastic unloading; secondly, as a new shear band is formed, the soils within the previous shear band(s) remain at the residual state or elastically unload. No special technique is used here to avoid mesh dependency problems due to the inclusion of strain softening, although these could be included via similar treatments as for FEM. The mesh was shown via a sensitivity study to be con-

(a) $t = 1.5$ s



(b) $t = 2.5$ s



(c) $t = 40.5$ s
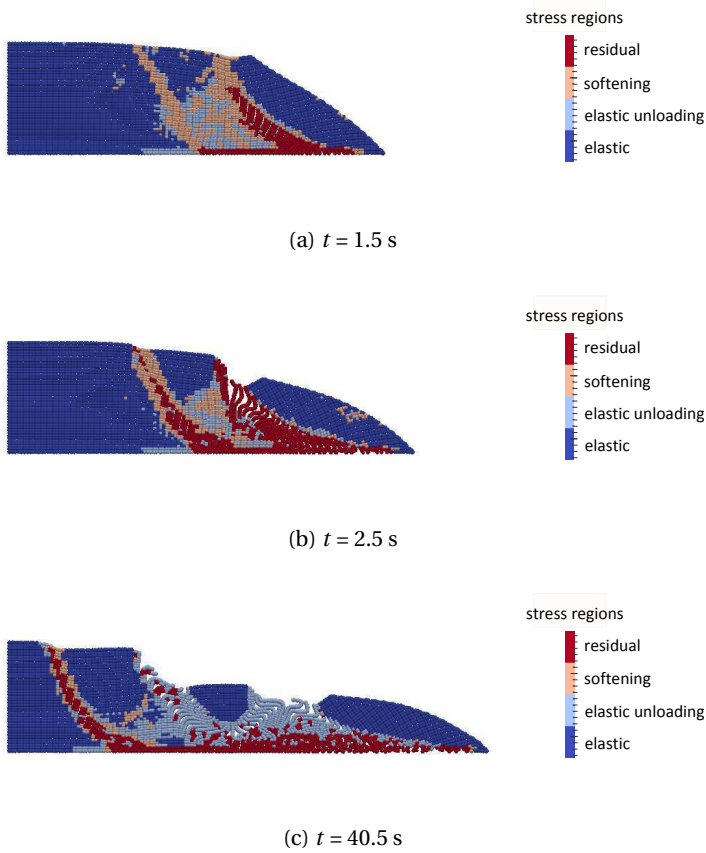
Figure 3.12: Evolution of stress regions during the slope failure process

verged, i.e. giving the same results for a finer mesh, although some mesh dependency was observed. The level of mesh dependency was found to be a function of the shear (softening) behaviour, the mesh size, the number of material points and the frictional boundary condition.

Fig. 3.13 shows the shear stresses at the material points at time $t = 40.5$ s. It is seen that the stress states coincide with the deformations in a reasonable way, i.e. shear stresses are largest either side of shear bands of failing or recently failed segments (the most left hand side in Fig. 3.13). Although stress oscillations are seen to exist spatially (as observed most clearly on either side of the shear band furthest to the left), these can be reduced by using Gaussian integration techniques, GIMP, etc. (Beuth et al., 2011; Bardenhagen and Kober, 2004).

To conclude, this type of slope failure is attributed to the slope geometry change during the retrogression. As the previous slide moves far, rendering the exposure of a steepened scarp behind it, the force imbalance will be transferred backwards and trigger
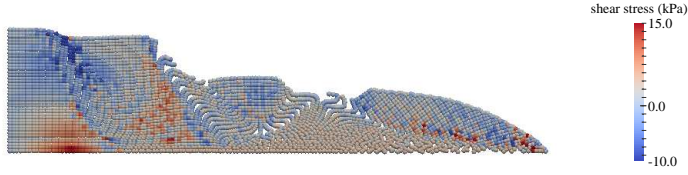
Figure 3.13: Shear stress at material points during the slope failure process at $t$ = 40.5 s

other slides. When a stable slope geometry is eventually formed, i.e. the incremental strain energy and kinetic energy become zero due to plastic deformation, friction, etc., the retrogression stops.

### 3.5.2. INVESTIGATION OF SLOPE RETROGRESSION BEHAVIOUR

#### INFLUENCE OF THE SOFTENING MODULUS

To further investigate the possible failure modes of the clayey slope, the softening modulus is discussed in this sub-section. Three cases have been analysed, corresponding to softening moduli of -25.0 kPa, -50.0 kPa and -75.0 kPa (whereas the softening modulus used in the previous section was -50 kPa). Other material properties are the same as for the base case. The simulations have again been run until quasi-static equilibrium states have been reached.

Fig. 3.14 shows the failure process of the slope for a softening modulus of -25.0 kPa. Three things should be noted. Firstly, the interval between the first slide and the second slide is much longer than for the slope with a softening modulus of -50.0 kPa. Secondly, the failure is seen to originate from the middle part of the previous slip circle, not from the slope base, thereby making the failed soil volume smaller. Thirdly, the final deposition of the slope is apparently different, with a smaller sliding distance; or, in other words, it poses a smaller risk to the surrounding area if the failure consequence is considered.

Fig. 3.15 shows the final displacement configurations and contours of accumulated shear strain invariant for the slope with a softening modulus of -75.0 kPa. The failure process was found to be similar to that of the slope with a softening modulus of -50.0 kPa, and is therefore not presented. As seen in the figure, the formation of the last "strange" vertical failure block is due to the boundary condition, which implies a larger sliding distance than the prescribed computational domain.

To conclude, the softening modulus has a strong impact on the slope post-failure behaviour, e.g. the extent of retrogression, sliding distance and number of failure blocks, as illustrated in this case. As the retrogression moves backwards, the released system energy will be gradually counteracted by the soil plasticity (where energy is lost) and friction on the bottom boundary.
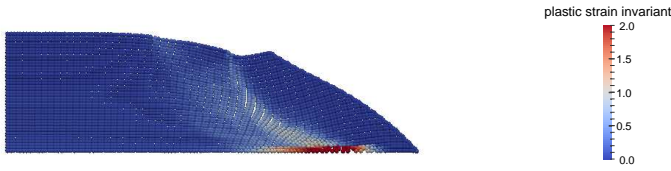
(a) formation of the first slip plane at $t = 6.0$ s
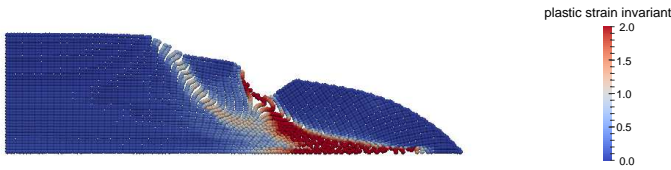


(b) formation of the second slip plane at $t = 23.25$ s
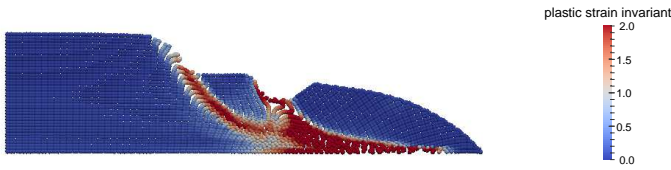


(c) final quasi-static state at $t = 38.25$ s

Figure 3.14: Collapse process of a short soft clayey slope with a softening modulus = -25.0 kPa

### INFLUENCE OF THE RESIDUAL SHEAR STRENGTH

In this sub-section, different residual shear strengths were considered, but with the same softening modulus, -50 kPa, to test how the post-failure slope behaviour is governed by the weakest soil strength. The coefficient $\eta$ is defined as the ratio of the residual strength over the peak strength. Apart from the original ratio, i.e. 0.2, used in the analysis presented in Section 3.5.1, two other ratios have been chosen, i.e. 0.4 and 0.6, corresponding to residual strengths of 8.0 kPa and 12.0 kPa, respectively. All other material properties and boundary conditions are the same as in Section 3.5.1, and the simulations were run until quasi-static equilibrium was reached.

The final slope geometries are shown in Fig. 3.16. Fig. 3.16(a) shows that, when the residual strength is 8.0 kPa (i.e. $\eta = 0.4$), two sliding soil blocks are formed, leaving a shallow headscarp exposed when the whole system is in equilibrium. Compared to the
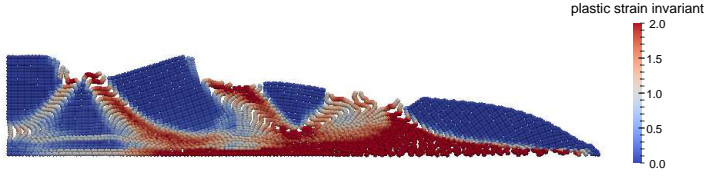
Figure 3.15: Final slope configurations corresponding to softening modulus = -75.0 kPa at $t = 82.5$ s

initial slide, the second slide does not propagate to the slope base and is smaller in size. The maximum plastic shear strain invariant is observed at the slope base boundary. In Fig. 3.16(b), where the residual strength is 12.0 kPa (i.e. $\eta = 0.6$), only one slide occurs, and the accumulated plastic strains are significantly lower than in the other two cases.
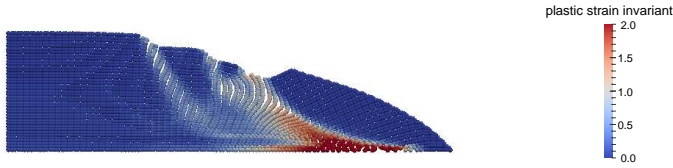


(a) final quasi-static state reached at $t = 48.75$ s for the case of $\eta = 0.4$
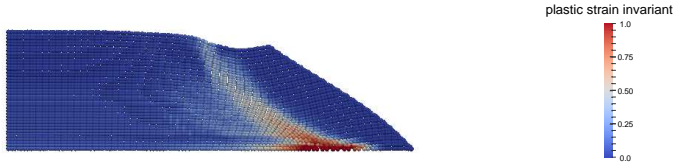


(b) final quasi-static state reached at $t = 8.25$ s for the case of $\eta = 0.6$

Figure 3.16: Final slope configurations corresponding to different residual shear strengths; $\eta$ refers to the ratio of the residual to peak shear strengths.

## INFLUENCE OF FRICTION AT THE BOTTOM BOUNDARY

The friction angle imposed at the bottom boundary has an influential effect on the propagation of the slope failures, which can alter the failure behaviour. Here two friction coefficients ($\mu_f$) have been considered, equal to 0.1 and 1.0. The softening modulus was

(a) final state at $t = 45.0$ s for case of $\mu_f = 0.1$



(b) final state at $t = 19.0$ s for case of $\mu_f = 1.0$
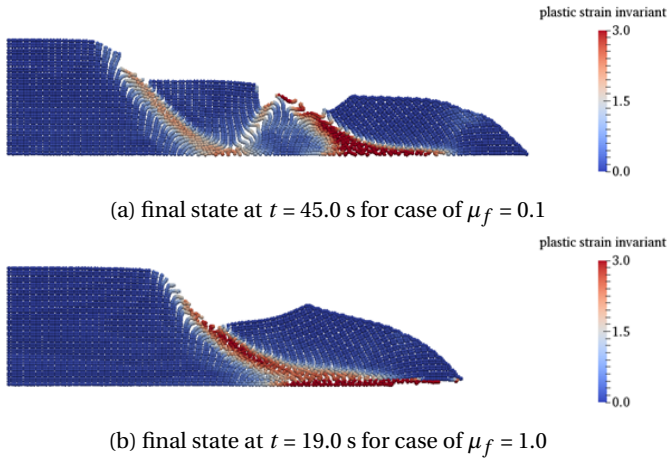
Figure 3.17: Final slope configurations corresponding to different friction coefficients

set to -25.0 kPa, and the other parameters and geometry are the same as above. The final slope configurations are shown in Fig. 3.17. The results can also be compared with the results presented in Fig. 3.14(c), where the friction coefficient is 0.3. It can be observed that, as the friction becomes larger, the number of failure blocks reduces, giving a shorter run-out distance. By comparing Fig. 3.14(c) with Fig. 3.17(a), although two blocks are formed in both cases, the failure is deeper into the soil when the friction at the boundary is smaller, as the soil runs out more quickly so a deeper second failure is caused. The times taken for the slope to reach equilibrium are also seen to increase when the friction is reduced.

## 3.6. Retrogressive failure of a long slope under self-weight loading

This section analyses a long inclined slope, comprising a 5 m thick layer of soft clay deposited on top of a sloping bedrock. A cutting has been made at the toe of the long slope which makes the slope unstable. The development of the failure mechanisms is investigated and discussed.
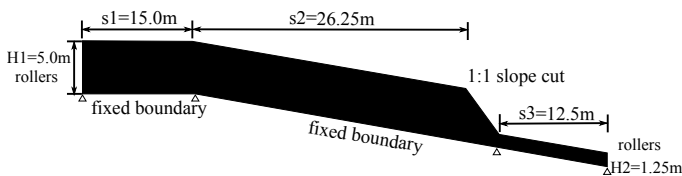


Figure 3.18: Initial configuration of a long inclined slope (not to scale)
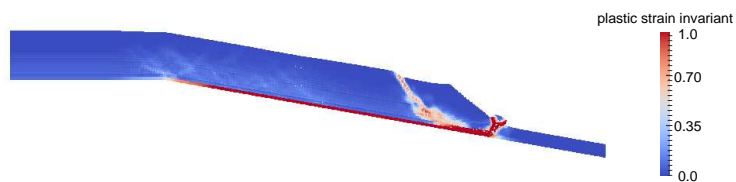
(a) first critical (rotational) slip surface formed at $t = 1.75$ s
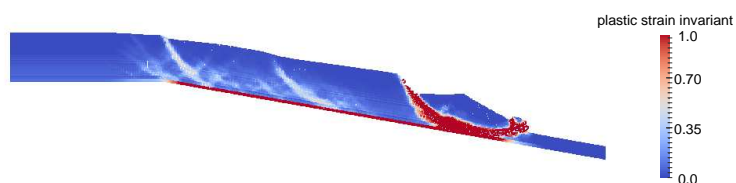


(b) translational failure surface formed at $t = 2.75$ s
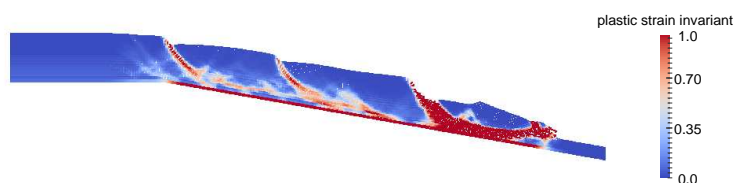


(c) retrogression backwards at $t = 4.0$ s
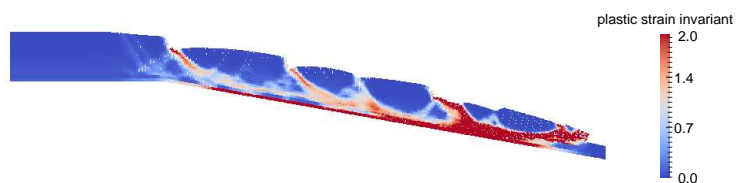


(d) configuration of the collapsed slope at $t = 6.0$ s, giving a step-like character

Figure 3.19: Collapse process of a long inclined slope

### 3.6.1. COLLAPSE PROCESS OF A LONG INCLINED SLOPE

The main slope is inclined at 10° and, to avoid boundary effects, a horizontal section is included at the top of the slope, as shown in Fig. 3.18. Towards the bottom of the slope, a smaller second slope has been cut to a depth of 3.75 m; this slope is inclined at an angle of 45° to the main slope surface (i.e. 55° to the horizontal). The horizontal section is 15 m long, whereas the inclined slope is over 40 m long (along the line of the slope), with the main section (5m deep) being over 26 m long. Parameters for the analysis are shown in Table 3.4. The boundary conditions include rollers at both ends of the domain, preventing horizontal displacement, and a fully fixed bottom boundary which simulates the rough interaction with the bedrock below. As in the previous numerical example, the slope fails under its own self weight. A total of 14980 material points and 4600 4-node background mesh elements are generated initially. Since the focus of the analysis is on the failure modes of the long inclined part of the slope, to reduce the computational cost the simulation is only run for 6.0 s, by which time the failure is fully developed in the inclined part, but not fully developed in the horizontal part. The time step is $5.0 \times 10^{-3}$ s. Once again, an Intel Xeon E5-1620 processor has been used, with the analysis taking approximately 1 hour to execute on a single core.

| Parameters | Values |
|---|---|
| Young's modulus (kPa) | 1000 |
| Poisson's ratio | 0.33 |
| Self weight (kN/m$^3$) | 20.0 |
| Peak cohesion (kPa) | 20.0 |
| Residual cohesion (kPa) | 5.0 |
| Softening modulus (kPa) | -75.0 |

Table 3.4: Material properties for the long slope analysis

Fig. 3.19 shows the accumulated shear strains at four times during the slope failure evolution, in order to provide a comprehensive explanation of the failure mechanism development. Fig. 3.19(a) shows that an initial rotational failure develops at the bottom of the slope. This slide increases the shear stresses at the bottom of the soil layer, leading to the propagation of a shear band back up along the base of the layer, to form the basal failure plane of a large translational slide, as shown in Fig. 3.19(b). At the top of the main slope, a curved slip plane develops, which is linked tangentially to the basal plane to form one large failure block. At the time, a secondary curved failure plane initiates from the middle part of the basal plane. Fig. 3.19(c) illustrates the step-like character of the slope due to the soil movement along the secondary planes. The development of the basal failure plane continues, as seen by the increasing plastic strain invariant along the bottom line. Also, more secondary failure planes are shown in Fig. 3.19(d), for the prescribed final time of $t = 6.0$ s. It is also seen that the soil mass dislocates due to active failures in the downslope area behind the initial circular slide; that is, soil wedges with shapes of sharp horst and graben are exhibited.
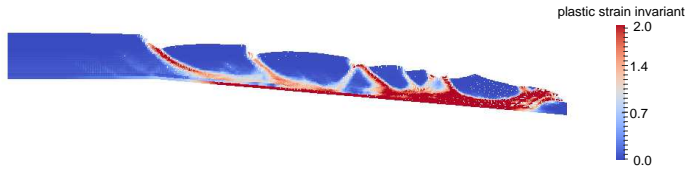
(a) slope angle = 5° ($t = 25.0$ s)
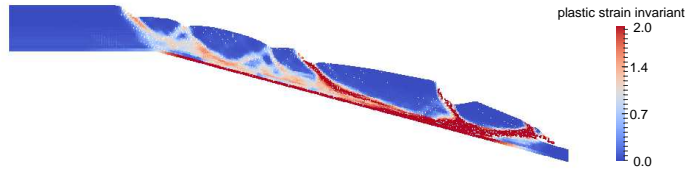


(b) slope angle = 15° ($t = 3.5$ s)
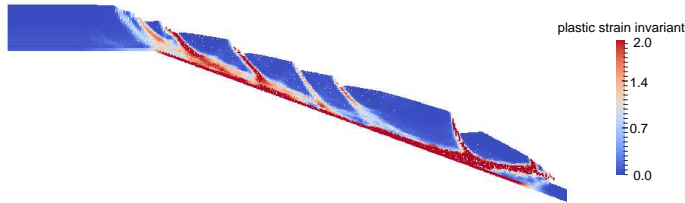


(c) slope angle = 20° ($t = 3.0$ s)

Figure 3.20: Failure of the long slope for different slope angles

## 3.6.2. INFLUENCE OF SLOPE ANGLE

For the above slope, a parametric study involving the slope angle is now presented. All properties and domain details are the same, except that slope angles of 5°, 15° and 20° are now considered. The corresponding failure configurations are illustrated in Fig. 3.20. Note that, in each case, the analysis has been terminated before the onset of the retrogressive failure at the headscarp.

With reference to Figs. 3.19(d) and 3.20, all slopes exhibit a translational failure, as well as a rotational failure at the slope toe. At a gentle slope angle (i.e. 5°, 10°), the rotational failure at the toe occurs prior to the occurrence of the translation; hence the rotational failure can be regarded as the trigger for the whole slope collapse, due to the removal of lateral restraint on, and subsequent increase of shear stress in, the soil behind. Specifically, for the case of 5°, after the initial rotational failure, there are a series of

retrogressive slides moving back up the slope from the toe, which is not seen in the case of 10°, before the formation of the entire translational failure of the main slope. There is also secondary movement within the moving mass, resulting in the appearance of horst and graben.

For a steeper angle (i.e. 15° as illustrated in Fig. 3.20(b)), the initial rotational and translational failure planes occur almost simultaneously. Moreover, the moving block in the translational failure is bigger than those in cases with shallower slope angles (in terms of failing volumes). For the steepest slope considered (i.e. 20°, Fig. 3.20(c)), there are three main differences in the failure mechanism development: firstly, slope failure is triggered by the translational slide; secondly, the toe rotational slide does not trigger retrogressive failures, although further slides occur within the moving soil mass due to the global translational failure; thirdly, there are a greater number of secondary slip planes, making individual failure blocks smaller, and all secondary movements are in the form of a series of rotational failures.

## 3.7. CONCLUSIONS

Retrogressive failures within a clayey soil slope have been analysed using the material point method (MPM) in conjunction with a simple elasto-plastic (Von Mises) softening constitutive model. The results show that MPM is a promising method to simulate slope failures, especially in capturing the post-failure behaviour of slopes. The evolution of the collapse process in a natural short slope, triggered by the soil self-weight, is provided first. Geometry changes during slope failure are thought to be a main reason for the retrogressive failure mechanism, with the removal of down slope support accounting for the successive slope failures, see Fig. 3.1(a). As the failure moves backwards up the slope, the time interval between successive failures becomes larger, and the failing area/volume can get smaller when a low softening modulus or a high residual stress is defined, see Figs. 3.14 and 3.16(a). By means of observing the range of final slope configurations for the short slope, it has been shown that multiple retrogressive failures in slope collapse processes are associated closely with the softening modulus and residual shear strength. Frictions at the slope bottom are also shown to have a significant influence on the slope failure development.

A long inclined slope has also been investigated. It has been seen that, as the slope angle increases, the failure mode changes. For a shallow slope, an initial rotational slide seems to trigger the whole slope collapse; then, as the retrogression moves back up the slope, the appearance of horst and graben (wedge) structures occurs, as was observed for the short slope, see Fig. 3.1(a). As the slope gets steeper, successive secondary rotational slides are usually observed, although the sliding distances of individual failure blocks with respect to each other are small compared to the shallower slopes in which the rear scarps of the slides are usually completely free. The failure mode can be generalised as a primary large translational failure, which propagates down to the base of the soil layer, giving a common basal slide plane, while, at the same time, secondary failure surfaces give the failed slope a step-like character, as shown in Fig. 3.1(b) and 3.2(a).

# 4

# SLOPE FAILURE ANALYSIS WITH RMPM

*The random material point method (RMPM), which combines random field theory and the material point method (MPM), is proposed. It differs from the random finite element method (RFEM), by assigning random field (cell) values to material points that are free to move relative to the computational grid, rather than to Gauss points as in a conventional finite element mesh. The importance of considering the effects of both large deformations and the spatial variability of soil strength properties in slope stability analyses is highlighted. The risks posed by potential slides are quantified by the extent of retrogressive failure; i.e. due to the tendency for secondary failures to be triggered by the removal of support from the remaining soil mass caused by the initial failure. The results show that RMPM provides a much wider range of possible solutions, in general increasing the volume of material in the failure compared to the RFEM solutions, which are usually limited to the initial slide. Moreover, the anisotropic nature of soil heterogeneity is shown to have a significant influence on the nature and extent of the failure.*

## 4.1. Introduction

Soils exhibit spatial variability of material properties due to variations in density, particle size distribution, minerology and stress history. A variety of failure mechanisms may be possible due to the spatial distribution of weaker soil zones. Hence, the influence of soil heterogeneity on slope failure initiation and post-failure behaviour is investigated in this chapter.

In traditional analysis methods, soil structures are often treated by subdividing the domain into layers (zones) comprising uniform soil types. However, it is well-known that the formation/deposition of soil layers is a complicated process involving geological, environmental, physio-chemical processes, and so on. Hence, even in so-called "uniform" deposits, spatial variation (i.e. heterogeneity) in material properties exist (Hicks and Samy, 2002). In deterministic designs, each material property is generally represented by its mean or some other characteristic value; this generally leads to a single factor of safety that reveals nothing about the probability of failure. However, by accounting for the natural variability of soils, a more realistic and comprehensive understanding of soil structure response can be obtained.

This chapter starts with a brief introduction on random field generation. This is followed by a series of investigations, using slope geometries similar to those already investigated in the previous chapter; however, this time accounting for the spatial variability of the undrained shear strength. For the shorter slope, the influence zone of the failure (i.e. the distance retrogressed) is mainly investigated. For the long slope, different factors, such as the scale of fluctuation, slope geometry, and mean undrained shear strength varying with depth, are investigated.

## 4.2. Development of random material point method

The precise determination of slope stability can be quite challenging, partly due to the spatial variability of soil properties. However, in conventional designs the ground is often assumed to be homogeneous, or subdivided into different homogeneous soil layers. Hence, slope stability tends to be represented by a single number, i.e. by a factor of safety (FOS), which is often obtained by using the strength reduction technique (Griffiths and Lane, 1999). However, it has been shown that the results can over or under predict the true FOS of a heterogeneous soil slope (Cho, 2007).

Probabilistic methods, which take account of the soil variabilities, can better describe slope stability than traditional deterministic methods. Since the first order second moment (FOSM) method (one of the simpler reliability methods) was proposed in the 1970s, many related methods have been developed and, among them, the random finite element method (RFEM) (Griffiths and Fenton, 1993) has shown good performance. However, as stated before, finite element analyses are often limited to small deformation problems, due to excessive mesh distortions during large deformations. Hence, for the purpose of tackling this problem, the random material point method (RMPM) is here proposed.

### 4.2.1. CHARACTERISATION OF SOIL VARIABILITY

Fig. 4.1 shows statistical measures of undrained shear strength $c_u$ of a clay soil. In conventional design, the mean undrained shear strength, which is constant with depth for the example in Fig. 4.1(a), or some other characteristic value, is normally used; while, in stochastic analysis, all the data are utilised, by use of, for example, a probability density function (pdf) as shown in Fig. 4.1(b).



(a) variation of $c_u$ with depth

(b) probability density function of $c_u$
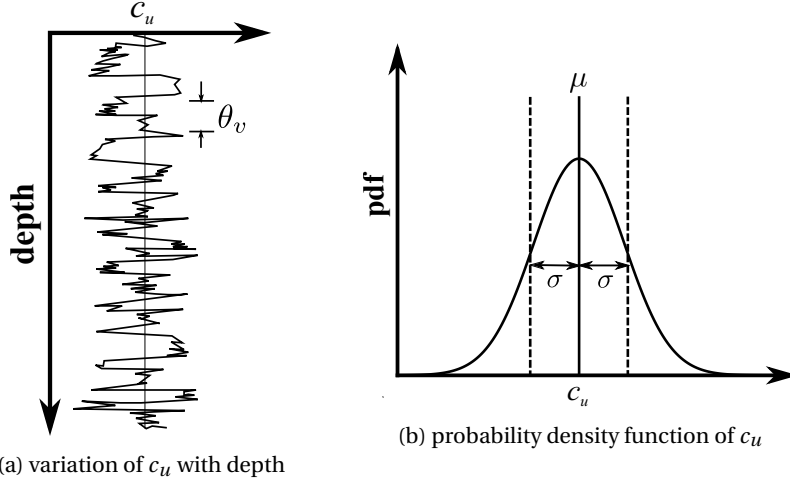
Figure 4.1: Statistical measures of $c_u$ variability

Hicks and Samy (2002) showed that the normal distribution can reasonably describe the variability of undrained shear strength for low and immediate values of the coefficient of variation (e.g. 0.1-0.3), as is often observed in practice. Although, in practice, other distributions, such as lognormal, exponential and beta may be used, the spatial variability of soil in this study is approximated by a normal distribution, due to its simplicity.

To define the variability of a soil parameter, the most basic statistical properties are the mean, $\mu$, standard deviation, $\sigma$, and the coefficient of variation, $V$, given by

$$V = \frac{\sigma}{\mu} \tag{4.1}$$

Furthermore, to consider the depth-dependent trends in the point statistics (i.e. in the mean and standard deviation), the definitions of the mean and standard deviation can be extended so that they are functions of depth, $z_d$ (Lumb, 1966), e.g.

$$c_u = \mu + \sigma u \tag{4.2}$$

in which

$$\mu = \mu(z_d) = \mu(z_d = 0) + \alpha_1 z_d \tag{4.3}$$

$$\sigma = \sigma(z_d) = \sigma(z_d = 0) + \alpha_2 z_d \tag{4.4}$$

where $u$ is a standardized random variable of zero mean and unit standard deviation, and $\alpha_1$ and $\alpha_2$ are fitting parameters.

The scale of fluctuation, $\theta$, is also needed to describe the spatial characteristics of soil variability. Fig. 4.1(a) shows that $\theta_v$, the vertical scale of fluctuation, defines the degree of spatial correlation with depth. Mathematically, $\theta$ is defined as the area under the correlation function (Vanmarcke, 2010). However, loosely speaking, it can be interpreted as the distance beyond which the correlation of property values becomes negligible (Vanmarcke, 2010; Griffiths et al., 2011).

The anisotropy of the heterogeneity, $\xi$, is the ratio of the horizontal and vertical scales of fluctuation, i.e.

$$\xi = \frac{\theta_h}{\theta_v} \tag{4.5}$$

where $\theta_h$ is the horizontal scale of fluctuation. Although anisotropy is often referred to in the literature, it is sometimes not implemented in analyses due to the difficulty in quantifying it to a sufficient degree of accuracy (Spencer, 2007). However, available evidence strongly points to a much larger correlation in the horizontal plane $\theta_h$ than in the vertical direction $\theta_v$, due to the process of deposition (Fenton and Griffiths, 2003; Griffiths and Fenton, 2004; Hicks and Onisiphorou, 2005). Once the statistics ($\mu$, $\sigma$, $\theta_v$, $\theta_h$) for a material are known, a numerical simulation of the material property distribution (i.e. a random field) can then be generated.

### 4.2.2. Random field generation

Random fields are numerically generated property distributions, which are intended to mimic the spatial variability found in nature. Numerous methods have been presented for the generation of random fields, such as the moving average (MA) technique (Gersch and Yonemoto, 1977), turning bands method (TBM) (Matheron, 1973), fast Fourier transform (FFT) method (Cooley and Tukey, 1965) and local average subdivision (LAS) method (Fenton and Vanmarcke, 1990), amongst which LAS is chosen for this study. In contrast to some other methods, LAS is computationally efficient in achieving accurate realisations of discrete local averages, which are especially convenient for directly mapping to the finite element meshes in RFEM or material points in RMPM. A 2-D implementation of LAS (Hicks and Samy, 2002) is used in the current investigation and, for completeness, local averaging theory and LAS in 2D are here briefly reviewed.

Assume the generated local averages are based on the field $X(t_1, t_2)$ over an area $A = T_1 T_2$. Mathematically, it is given by

$$X_A(t_1, t_2) = \frac{1}{A} \int_{t_1 - \frac{T_1}{2}}^{t_1 + \frac{T_1}{2}} \int_{t_2 - \frac{T_2}{2}}^{t_2 + \frac{T_2}{2}} X(t_1, t_2) \, dt_1 dt_2 \tag{4.6}$$

in which area $A$ has dimensions of $T_1 \times T_2$, with each side parallel to the axes $t_1$ and $t_2$, respectively. The variance of the local averages is expressed as

$$\sigma_A^2 = \sigma^2 \gamma(T_1, T_2) \tag{4.7}$$

in which $\gamma(T_1, T_2)$ is the variance function, given by (Vanmarcke, 2010),

$$\gamma(T_1, T_2) = \frac{1}{T_1 T_2} \int_{-T_1}^{+T_1} \int_{-T_2}^{T_2} (1 - \frac{|\tau_1|}{T_1})(1 - \frac{|\tau_2|}{T_2}) \rho(\tau_1, \tau_2) \, d\tau_1 \, d\tau_2 \tag{4.8}$$

in which $\rho(\tau_1, \tau_2)$ is the correlation function, and $\tau_1$ and $\tau_2$ are the lag distances in the two directions.

The governing covariance function can take various forms, but the one used in the present implementation is the Gauss-Markov process with an exponential covariance function. The correlation function is given by

$$\rho(\tau_1, \tau_2) = \exp\left\{ -\sqrt{\left(\frac{2\tau_1}{\theta_1}\right)^2 + \left(\frac{2\tau_2}{\theta_2}\right)^2} \right\} \tag{4.9}$$

where $\theta_1$ and $\theta_2$ denote the scales of fluctuations in two directions.

Averaging the random field $X(t_1, t_2)$ over the rectangular area $A$ can be carried out in two stages:

(1) Integrate $X(t_1, t_2)$ over the distance $T_1$ along the $t_1$ axis, which gives a 1-D random function $X_{T_1}(t_2)$, defined as the local average of $X(t_1, t_2)$ within a band of length $T_2$ parallel to the $t_2$ axis:

$$X_{T_1}(t_2) = \frac{1}{T_1} \int_{t_1 - \frac{T_1}{2}}^{t_1 + \frac{T_1}{2}} X(t_1, t_2) dt_1 \tag{4.10}$$

The variance of $X_{T_1}(t_2)$ is,

$$\sigma_{T_1}^2 = \sigma^2 \gamma(T_1) \tag{4.11}$$

(2) Integrate $X_{T_1}(t_2)$ over the distance $T_2$ along the $t_2$ axis, leading to a further reduction in the variance, such that

$$\sigma_A^2 = \sigma^2 \gamma(T_1) \gamma(T_1 | T_2) \tag{4.12}$$

where $\gamma(T_1 | T_2)$ is the conditional variance function of $X(t_1, t_2)$, provided averaging over distance $T_1$ has been performed.

By combing Eqs. 4.7 and 4.12, the variance function can be expressed as the product of the 'marginal' and 'conditional' variance functions, i.e.

$$\gamma(T_1, T_2) = \gamma(T_1) \gamma(T_1 | T_2) \tag{4.13}$$

For further details on the formulation, readers can refer to Samy (2003). The local average subdivision method is summarised as follows:

(1) Define a square domain, with an initial global mean based on a standard normal distribution and a reduced variance due to the domain size relative to the scale of fluctuation;

(2) Split the field into four cells;

(3)  Generate three cell values by random process, and the fourth cell value by upwards averaging so as to preserve the initial mean;

(4)  Repeat the above three stages until the desired field resolution is reached.

After the standard normal random field values have been generated appropriately, the last stage is to transform these values into soil parameter values $X$, as input for the FEM or MPM program, using a probability density function such as the normal distribution as has been used for this study. Hence, this involves the following transformation:

$$c_u = \mu + \sigma Z \tag{4.14}$$

where $\mu$ is the mean property value, for example, deduced from from in-situ tests, $\sigma$ is the standard deviation from that mean, and $Z$ is the local average for a random field cell. Note that, for the LAS implementation used here, anisotropic random fields have been generated by post-processing isotropic random fields (Samy, 2003).

### 4.2.3. RANDOM FINITE ELEMENT METHOD

For slope stability analysis, probabilistic modelling started mainly through the use of limit equilibrium methods linked to various statistical approaches (e.g. El-Ramly et al. (2002)), and continued steadily (e.g. Li and Lumb (1987), Christian et al. (1994), Duncan (2000)). More recently, numerical methods have been seen as a viable alternative to the limit equilibrium method. For example, Fenton and Griffiths (2002, 2003) and Hicks and Samy (2002) combined random field theory (Vanmarcke, 1977a), for modelling the spatial variability of soil properties, with the finite element method (FEM), for modelling slope failure mechanims, within a Monte Carlo simulation process; this approach is often referred to as the random finite element method (RFEM) (Griffiths and Fenton, 2004).

RFEM involves multiple realisations of the problem to be solved, in which each realisation involves generating a random field of the material property, mapping cell values from the random field onto the FEM mesh at the Gauss point level, and analysing the problem deterministically by FEM (Hicks and Spencer, 2010). Through using the random finite element method (RFEM), it has been shown that the most critical slope failure mechanisms seek out the path of least resistance (Hicks and Samy, 2002; Fenton and Griffiths, 2002, 2003). Moreover, RFEM fully accounts for spatial correlation and averaging, so that it offers many advantages over traditional probabilistic slope stability techniques (Griffiths and Fenton, 2004). It has also been shown that the mean FOS for a heterogeneous slope is weaker than the deterministic response based on the mean property value, due to the apparent reduction in the property mean along the failure path (Hicks and Nuttall, 2012).

A correlation function refers to a statistical correlation between random variables at two different points in time or space. An isotropic correlation structure has often been used in modelling spatial variability. Paice et al. (1996) studied the effect of a random and spatially correlated soil stiffness on the total settlement under a uniformly loaded strip footing. Griffiths and Fenton (2004) investigated the probability of failure of a cohesive slope and pointed out that, by assuming perfect correlation in which the spatial variability is ignored, simplified probabilistic analysis can lead to unconservative estimates of the probability of failure, thereby highlighting the importance of incorporating spatial

variability into slope stability analyses. Griffiths et al. (2011), through using random field analyses, discussed the influence of spatial variability on infinite slope failures. The location of the critical failure planes were shown to very likely occur above the bottom of the slope, which explains how "first order" methods may underestimate the probability of slope failures, in that the failure planes are always assumed to occur at the base of such slopes. This further demonstrates the importance of utilising random field analyses in slope stability problems, as they allow for the "seeking out" effect.

There is also the issue of anisotropic spatial correlation, in that the spatial correlation length in the horizontal plane is likely to be greater than in the vertical direction (Griffiths et al., 2011). Hicks and Samy (2002) reported that anisotropy of the heterogeneity can have a significant influence on the computed reliability. Hicks and Onisiphorou (2005) focused on the static liquefaction of heterogeneous soil layers in an underwater sandfill berm, and revealed that the spatial correlation length has a significant influence on failure mechanism development and the potential for global instability. Cho (2007, 2009) presented a probabilistic slope stability analysis, in which the importance of the spatial correlation structure was highlighted. Zhu et al. (2013) considered the effect of variation of the permeability function, which relates the coefficient of permeability of the soil to the matric suction, on slope stability and reported that the correlation length of the saturated permeability influences the range of calculated factor of safety values significantly, but does not influence the mean factor of safety substantially. The minimum mean factor of safety was shown to occur at nearly the same critical correlation length that causes the maximum change in the groundwater table.

Note that some reduction of the distribution width of the randomized material properties may be possible, by constraining the spatial variability using site specific data (e.g. cone penetration tests (CPTs) and piezometers) to condition the random fields (Lloret-Cabot et al., 2014). However, many measurements cannot be directly incorporated into conditional random fields, as they measure system responses rather than soil properties, thereby requiring the use of inverse analysis. Chen and Zhang (2006) back-calculated the hydraulic conductivity by use of the measured pore pressure head, whereas Hommels and Molenkamp (2006) reduced the uncertainties in soil stiffness through the use of measured settlements. To make better use of limited site information, material parameters may be modelled as cross-correlated. Vardon et al. (2016) correlated hydraulic conductivity with the shear strength properties (i.e. cohesion and friction angle) of soils using the Kozeny-Carman equation, and applied the results to reduce uncertainties in slope stability analyses. Arnold and Hicks (2011) evaluated the stability of an unsaturated slope during a rainfall event, by spatially varying five influential parameters which were pointwise cross-correlated.

Another consideration is that the strength parameters of soil often vary with depth, due to the process of soil deposition. Gibson and Morgenstern (1962) presented stability numbers for clay slopes in which the shear strength, $c_u$, is directly proportional to depth, and concluded that: "The interesting result emerges that the factor of safety is independent of the height of the slope." Hicks and Samy (2002), by considering the mean trend of the undrained shear strength increasing with depth in a clayey slope, further demonstrated this fact and showed that the reliability can reduce greatly due to a greater range of possible rupture surfaces. Li et al. (2014) studied the influence of the shear strength

parameters (cohesion and friction angle) linearly increasing with depth within infinite slopes, under which circumstances the possibility of critical slip surfaces occurring at the slope bottom decreases considerably.

The investigations have been extended to 3D in recent years. Hicks et al. (2008), Hicks and Spencer (2010) and Hicks et al. (2014) conducted a series of 3D RFEM analyses and found that, based on the horizontal scale of fluctuation relative to the slope geometry, three categories of failure mode were identified for slopes that were long in the third dimension; moreover, the risk posed by potential slides was quantified in terms of slide volumes and slide lengths, which are closely related to the category of failure mode (Hicks et al., 2008, 2014). Griffiths et al. (2009) compared the probability of slope failure using 2D and 3D RFEM probabilistic analyses, and concluded that 2D probability analysis may underestimate the probability of slope failure. Li and Hicks (2014) and Li et al. (2015) compared 3D RFEM solutions with Vanmarcke's (1977b) analytical solution, and showed that significantly different results may be calculated, depending on the scale of fluctuation (SOF) of undrained shear strength in the horizontal direction relative to the slope dimensions. The difference is greatest for small SOFs, due to differences in the predicted failure length and the exaggerated contribution to sliding resistance due to end-effects in the analytical model. In contrast, for large horizontal SOFs relative to the slope length, the two methods generally agree.

### 4.2.4. RANDOM MATERIAL POINT METHOD

As stated above, the spatial variability of soil properties can have a significant effect on soil structure response. However, research so far has been limited to small deformations; hence, the ongoing failure development has been ignored, thereby leading to an incomplete description of the failure mechanism in some cases. Hence, to quantify the risk posed by progressive and retrogressive failures, and to analyse the influence of spatial variability of soil properties on slope post-failure behaviour, an alternative to RFEM (which has generally been based on small strain theory) is investigated here.

By combining random field theory and MPM, this chapter proposes a new technique to investigate the influence of heterogeneity on slope failure mechanisms involving large deformations, including secondary failure mechanisms and failure consequences. This technique is called the "Random Material Point Method" (RMPM). In contrast to RFEM, the random field is mapped onto the problem domain at the material point level in RMPM, rather than to Gauss points. Multiple random field realisations are obtained, and Monte Carlo simulations, involving multiple material point method analyses, are performed in order to obtain a distribution of possible responses. Note that, during the computational cycle, the values are transferred to the nodes, and therefore there will be averaging if there are many material points per cell. However, each material point is dealt with separately in the plasticity algorithm.

## 4.3. INFLUENCE OF HETEROGENEITY ON THE FAILURE OF A SHORT SLOPE

By utilising the proposed RMPM, the influence of soil heterogeneity on an idealised strain-softening clay slope, similar to that in section 3.5, is investigated. For simplicity,

random fields are only used to model the spatial variability of the (peak) undrained shear strength, with the residual strength being modelled as proportional to the peak strength during the analysis. By equating the risk posed by the slope post-failure to the sliding distance, i.e. how far the slope failure retrogresses backwards from the slope crest, the differences with deterministic and RFEM solutions are highlighted.

### 4.3.1. PROBLEM DESCRIPTION

An idealised boundary value problem has been analysed to provide a simple illustration of RMPM, although the same methodology can (and will in the future) be applied to coupled effective stress analyses. Compared to the previous short slope analysis, the left boundary is now extended a greater distance from the slope crest, that is, 20 m, to provide enough space for the development of retrogressive failures. Fig. 4.2 shows a 45°, 5 m high, clay slope, resting on a firm foundation layer. The initial slope geometry has been discretized using 1810, 4-node, quadrilateral elements, with 4 material points per element located at the Gauss point positions (i.e. initially, before the slope starts to deform). The 3000 grey squares in Fig. 4.2 represent the computational domain covering the potential moving trajectories of material points. A frictional contact between the slope base and supporting firm ground is assumed, while rollers are prescribed at the left-hand boundary allowing only vertical movement. The Young's modulus and Possion's ratio are $E$ = 1000 kPa and $v$ = 0.33, respectively. While an undrained failure implies a Poisson's ratio of 0·5, the adopted smaller value aids numerical convergence and promotes a more realistic in-situ stress field, whereas the plastic model component dominates the failure mechanism. The mean peak undrained shear strength is 20 kPa, the residual strength is 4 kPa, and the softening modulus is -50 kPa. For simplicity, the slope is unstable under its own weight; hence, the slope failure is triggered by applying gravitational loading to generate the in-situ stresses. The scales of fluctuation and degrees of anisotropy of the heterogeneity are investigated to quantify the risk posed, as quantified by the distance the failure retrogresses back from the slope crest. The time step is set as $2.5 \times 10^{-3}$ s.
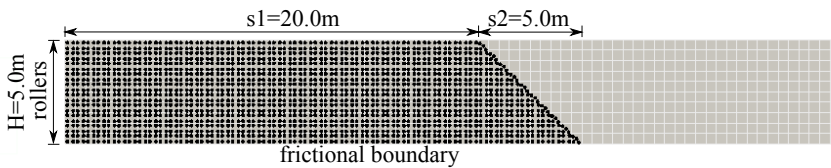


Figure 4.2: Boundary conditions, background mesh and initial geometry of the clay slope. A cruder mesh than used in the analysis is shown for reasons of clarity

### 4.3.2. DETERMINISTIC ANALYSIS

Fig. 4.3(a) shows the final slope configuration computed using a deterministic MPM analysis; that is, once a quasi-static equilibrium state is reached, based on a criterion taking account of the kinetic energy and unbalanced force of the system (Al-Kafaji, 2013). Three failure blocks, as a consequence of three failure planes, are seen to have formed during the failure process. For a straight-forward quantification of the potential failure

consequence, the sliding distance $r$, as shown in Fig. 4.3, is used to define how far the failure retrogresses backwards from the crest.

The remaining subfigures in Fig. 4.3 illustrate the spatially converged result presented in Fig. 4.3(a) via use of additionally discretised analyses. Fig. 4.3(b) presents an analysis utilising 1.5 times more elements in each direction, again with initially 4 material points per element, and Fig. 4.3(c) presents an analysis with the same number of elements and initially 16 material points per element. Although, as expected, some mesh dependency is observed, the overall behaviour, number of failures and sliding distance are consistent enough to ensure the veracity of the following numerical study (which is based on the discretisation in Fig. 4.3(a)). Hence, for considering both the computational accuracy and cost, a discretisation of 1810 elements, with 4 material points per element is chosen for the following analyses.



(a) most coarse converged mesh (1810 elements, 4 material points per element)



(b) refined elements (3840 elements, 4 material points per element)



(c) refined material points (1810 elements, 16 material points per element)
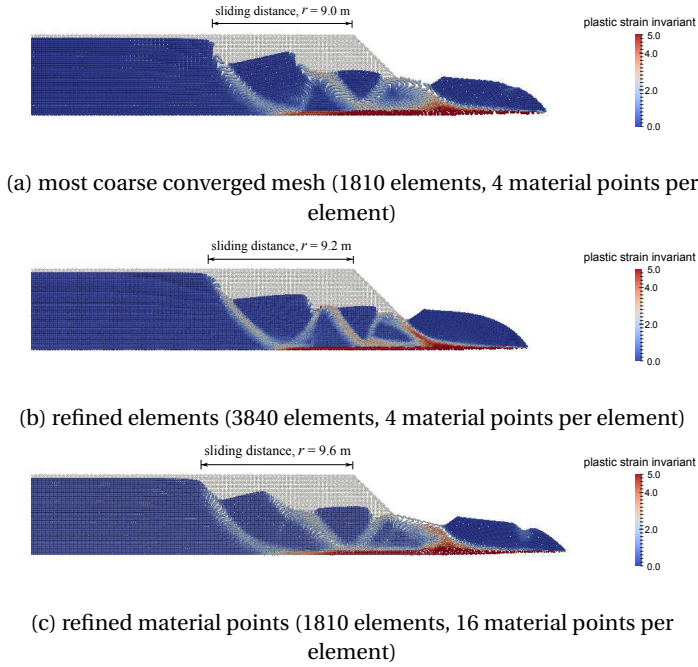
Figure 4.3: Initial and final slope configurations, with contours of plastic shear strain invariant, including spatial convergence analysis

### 4.3.3. Failure process of heterogeneous slopes

The influence of spatial variability of undrained shear strength on the slope response has been assessed by assuming a coefficient of variation of 0.25 for both the peak and residual shear strengths (with all other parameters the same as for the deterministic analysis). Fig. 4.4 shows the failure process for a typical realisation in which $\theta_v = 1.0$ m and $\theta_h = 48.0$ m. The process is divided into three stages, these being initial failure, the first failure block formed, and the final configuration. Fig. 4.4(a) shows the random field of

undrained shear strength for the soil in the slope, with blue representing weak zones and red representing strong zones. The strong soils are, in this case, near the base and top of the soil layer, with the weaker zones in between. As the self-weight is applied, to generate the in situ stresses, the stresses start to build up near the slope toe, which is often where failure initiates if the slope becomes unstable. However, due to the strong soil at the base of the layer, the failure initiates slightly above the toe where the slope stability number ($c_u/\gamma_z z_d$ ) is lower. Hence the failure mechanism avoids the stronger area and seeks out the "path of least resistance", failing at the base of the weaker soil as seen in the final slope configuration.

The "stress regions", shear stresses, and contours of plastic shear strain invariant within the slope are shown in Fig. 4.4(b), (c) and (d), respectively. Fig. 4.4(b) depicts the stages of the constitutive model; that is, the "stress region" governing the behaviour of the material points within the slope. Hence, blue, light blue, orange and red colours indicate elastic, elastic unloading, softening and residual stages of the model, respectively. It is seen that the material points within a developing shear band are mostly governed by the residual cohesion, whereas the soils within previous shear bands mostly experience elastic unloading as a new shear band is being formed. Fig. 4.4(c) shows that the shear stresses at the material points, during the slope collapse process, reasonably coincide with the slope deformations. Fig. 4.4(d) shows that the largest plastic shear strain invariant contours propagate mainly horizontally, forming the basal line of the global failure. Due to the removal of support from the soil at the back-scarp of the first slide, the failure of the back-scarp is triggered and the second failure block is formed, with deformation continuing until the final equilibrium state.

### 4.3.4. Influence of horizontal anisotropy
The influence of horizontal anisotropy (of the heterogeneity) on the slope failure modes is shown in Fig. 4.5, where the final slope configurations for $\theta_h$ = 1.0 m and 6.0 m, with $\theta_v$ = 1.0 m, are depicted. Figs. 4.5(a) and (c) show the random field of the peak cohesion for the soil; and (b) and (d) reveal the final slope deformed states in terms of plastic shear strain invariant contours.

With reference to Figs. 4.4 and 4.5, one common conclusion is that the slopes seek to fail through the weakest zones, which can be seen by the shear bands forming across these areas for each discrete failure block. Meanwhile, it is observed that, for the smaller degree of anisotropy, there is a tendency for multiple failure blocks to form, due to it being easier to "seek out" a failure path through the weaker zones (while avoiding the strong ones). Hence, there are many more zones of deformations within the slope, as shown in Fig. 4.5 (a) and (c). For the larger degree of anisotropy shown in Fig. 4.5 (b) and (d), as the failure retrogresses, bigger blocks are generally formed, as the failure path tries to propagate through the weak zones as much as possible. By also considering the case of $\theta_h$ = 48.0 m (see Fig. 4.4) it may be inferred that, as the horizontal correlation length increases, the slope failures tend to involve larger and fewer intact failure blocks.

initial failure     first failure block formed     final failure

(a) peak cohesion

(b) stress regions

(c) shear stress

(d) plastic strain invariant

31.0

7.6

residual
softening
unloading
elastic

16.3

-18.2

5.0

0.0
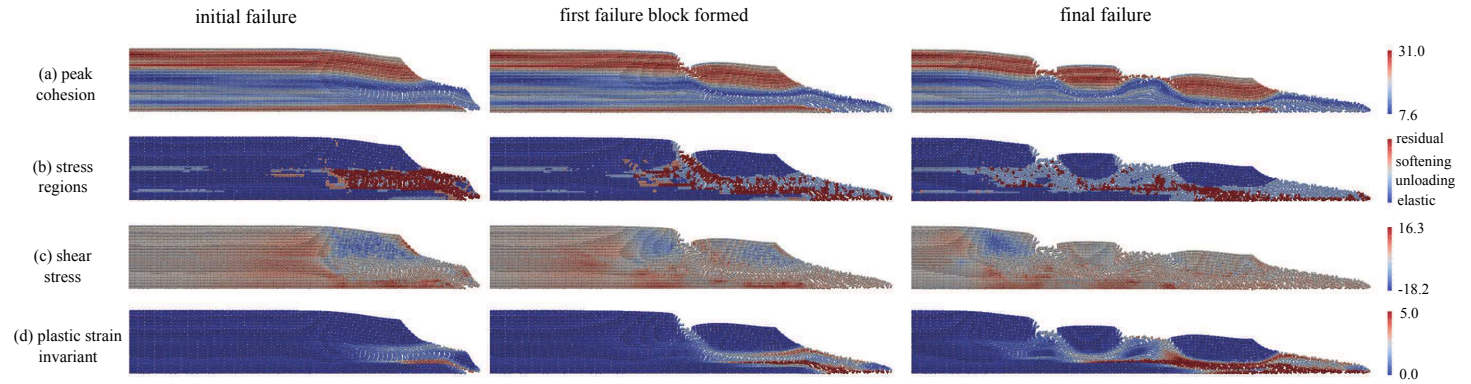
Figure 4.4: Collapse process of a heterogeneous slope with $\theta_h$ = 48.0 m, $\theta_v$ = 1.0 m: (a) peak cohesion distribution within the slope (kPa); (b) stress regions corresponding to the four stages of the implemented material model; (c) shear stress (kPa); (d) accumulated plastic shear strain invariant

(a) $\theta_h = 1.0$ m, $\theta_v = 1.0$ m, random field of peak cohesion (kPa)



(b) $\theta_h = 1.0$ m, $\theta_v = 1.0$ m, plastic shear strain invariant contours



(c) $\theta_h = 6.0$ m, $\theta_v = 1.0$ m, random field of peak cohesion (kPa)



(d) $\theta_h = 6.0$ m, $\theta_v = 1.0$ m, plastic shear strain invariant contours
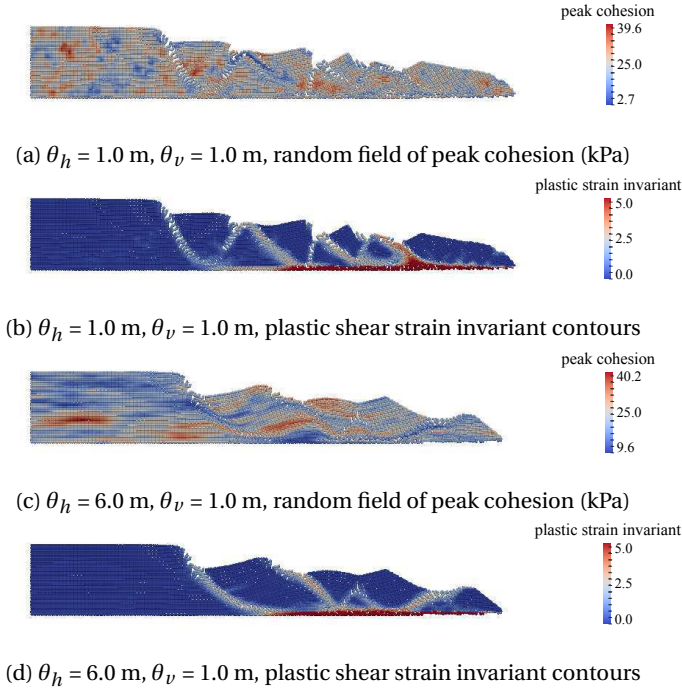
Figure 4.5: Typical final slope configurations for $\theta_h = 1.0$ m and 6.0 m

### 4.3.5. Influence of scale of fluctuation

Two typical isotropic random fields, corresponding to scales of fluctuation of $\theta_h = \theta_v = 1.0$ m and 2.5 m are analysed in this section. Fig. 4.6 shows the random fields of peak cohesion, and corresponding final slope configurations due to self-weight loading. The failure is seen to retrogress backwards, stopping at distances of 9.32 m and 16.30 m for $\theta = 1.0$ m and $\theta = 2.5$ m, respectively.

In Fig. 4.6, three things may be highlighted. Firstly, the influence zone is larger than in the deterministic analysis, especially in case of a lager scale of fluctuation. Secondly, the failed soil block shapes are more diverse. The deterministic analysis reveals failing blocks that are mostly circular wedges, whereas, in heterogeneous slopes, due to the characteristic of seeking out the paths of least resistance automatically during the failure formation, various block shapes and failure mechanisms are observed. Thirdly, the failure process can be different. In the deterministic analysis, the failures occurring at the slope front necessarily happen prior to the ones away from the slope face. However, in the presence of heterogeneity, the soil can fail as a big block first, due to the presence of the weaker soils along the failure path, and subsequently, the within soils can be dislocated into a number of smaller blocks, which is rather like the failure mechanism seen for some long inclined slopes.

(a) $\theta_h = \theta_v = 1.0$ m, random field of peak cohesion (kPa)



(b) $\theta_h = \theta_v = 1.0$ m, final plastic shear strain invariant contours



(c) $\theta_h = \theta_v = 2.5$ m, random field of peak cohesion (kPa)



(d) $\theta_h = \theta_v = 2.5$ m, final plastic shear strain invariant contours
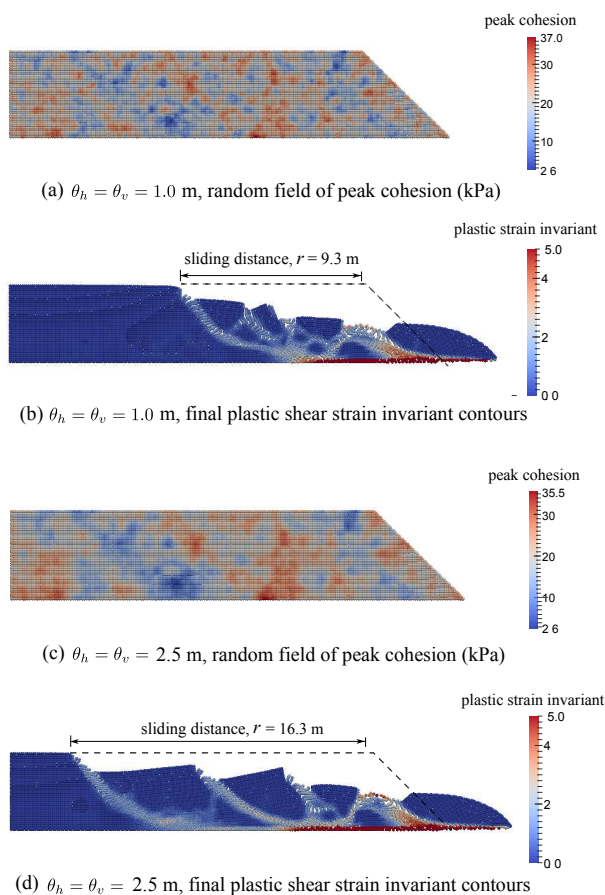
Figure 4.6: Typical final configurations for different scales of fluctuation

### 4.3.6. RMPM VS DETERMINISTIC ANALYSIS

A series of RMPM analyses, each comprising 100 Monte Carlo realisations, have been conducted, for $\theta_v = 1.0$ m and $\theta_h = 1.0$, 6.0 and 48.0 m. Results have been compared to the deterministic analysis, in order to give a more comprehensive and quantitative view of the risk of slope failures.

Figs. 4.7(a) – (c) show the probability density histograms of the computed sliding distance, as well as the fitted normal probability density functions. The normal distribution fits the computed results of the Monte Carlo simulation reasonably well for smaller values of $\theta_h$, as in Figs. 4.7(a) and 4.7(b). Although Fig. 4.7(c) shows a less good fit due to the higher number of realisations needed for convergence with higher $\theta_h$ (Hicks and Samy, 2002), the number of realisations is sufficient to enable proper evaluation of trends. Moreover, the peak in the number of realisations showing a sliding distance of 20 m is an indication that the mesh does not extend far enough from the slope crest in

(a) $\theta_h = 1.0$ m

(b) $\theta_h = 6.0$ m

(c) $\theta_h = 48.0$ m

(d) influence of $\theta_h$ on PDF
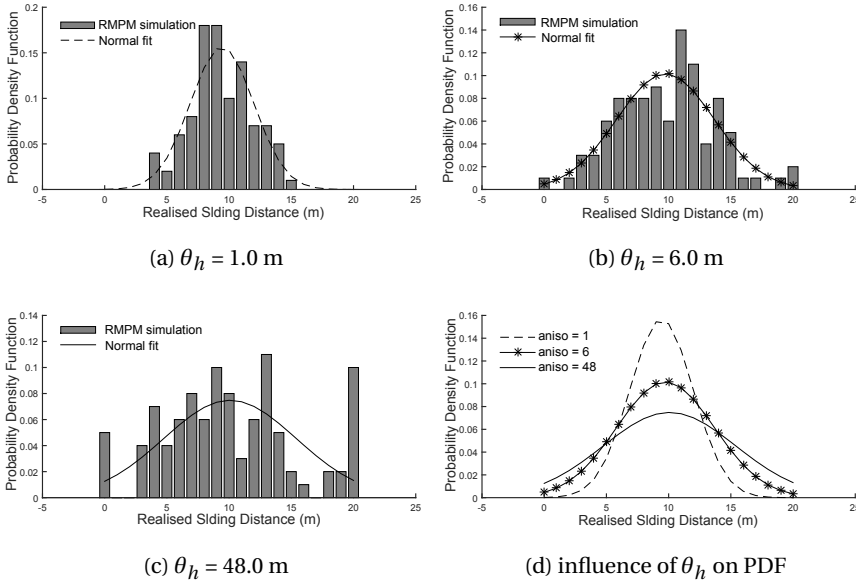
Figure 4.7: Probability density functions of the realised sliding distance for the slope

some cases. The mean sliding distances for $\theta_h$ = 1.0, 6.0 and 48.0 m are $r$ = 9.43, 9.75 and 10.07 m, respectively, compared with $r$ = 9.0 m for the deterministic MPM analysis based on the mean undrained strength. However, of greater practical significance is that the standard deviation of (i.e. the uncertainty in) $r$ increases significantly with $\theta_h$, by a factor of around 2 for the range of $\theta_h$ considered. Hence, the deterministic analysis may seriously underestimate the sliding distance, giving an unconservative estimate of the risk. For the case in which $\theta_h$ = 48.0 m, the spatial variability takes on a layered appearance. A possible consequence is that the slope remains stable (i.e. $r$ = 0 m) due to the presence of high strength soil layers along the potential failure path, espically near the slope toe; conversely, the slope can slide a large distance (e.g. $r$ > 20 m) due to the presence of weak layers.

Note that some reduction of the distribution width may be possible, by constraining the spatial variability using site-specific data to condition the random fields (Lloret-Cabot et al., 2014).

### 4.3.7. RMPM VS RFEM
RFEM solutions have been obtained and compared with results of RMPM (for the same ensemble of random fields), as shown in Fig. 4.8 for $\theta_h$ = 1.0 m. Due to the assumption of small deformations in the RFEM simulation carried out in this thesis, secondary slides were generally not computed, thereby significantly reducing the sliding distance and range of solutions relative to the RMPM simulation. With RMPM, the failure is able to retrogress backwards during the slope collapse, due to the removal of support pro-

vided by soil involved in the initial failure.
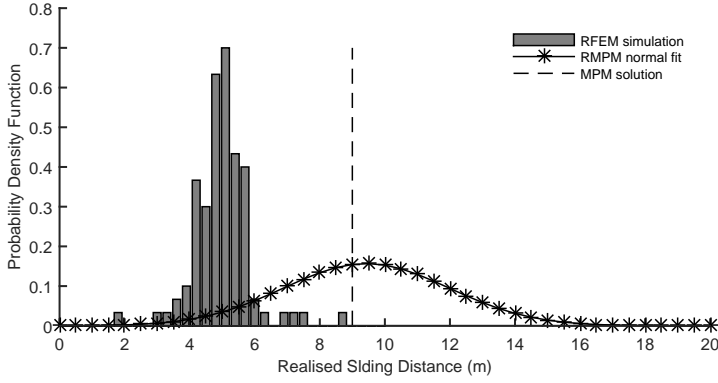


Figure 4.8: RMPM versus RFEM for $\theta_h = 1.0$ m, $\theta_v = 1.0$ m

### 4.3.8. CONCLUSION

To conclude, this section has given a straight-forward insight into the influence of heterogeneity on the slope failure mechanism and propagation. The potential of RMPM in geotechnical analysis has been simply demonstrated for an idealised slope in a strain-softening soil. Large deformations and heterogeneity were both shown to have a significant effect on the initiation and evolution of the slope failure mechanism. By equating the potential failure consequence to the sliding distance (i.e. extent), the deterministic analysis may yield an unconservative result (i.e. it may underestimate the possible risk). RFEM solutions based on small deformations are mainly restricted to initial slope failures, thereby neglecting the effects of possible retrogressive and progressive failures. The influences of the horizontal anisotropy (of the heterogeneity) and scales of fluctuation can cause noticeable changes in the slope failure modes.

## 4.4. INFLUENCE OF HETEROGENEITY ON THE FAILURE OF A LONG SLOPE

This section focuses on the influence of heterogeneity on a long inclined slope. It is commonly reported (e.g. Andresen and Jostad (2004, 2007)) that failure propagates along the slope base in deterministic analyses of this type of gently inclined slope (see also section 3.6 for the failure mechanism of a long inclined slope). But, by incorporating different horizontal scales of fluctuations, various results can be obtained. Three factors are mainly discussed in this section; i.e. the degree of anisotropy of the heterogeneity, slope geometry and coefficient of variation.
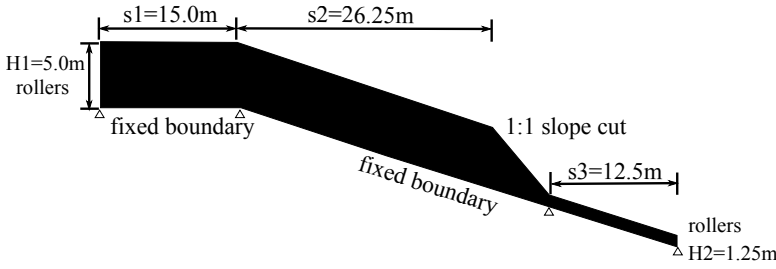
Figure 4.9: Problem geometry (not to scale)

### 4.4.1. PROBLEM DESCRIPTION

A long inclined slope, in a dog-leg shape, as investigated previously in section 3.6, is analysed in this section by incorporating random fields to investigate the influence of heterogeneity on the failure mechanisms of long inclined slopes. For completeness, the slope geometry is again shown, in Fig. 4.9. The main slope is inclined at an angle of 20° to the horizontal; towards the bottom of the slope, a smaller second slope has been cut to a depth of 3.75 m, with an inclination of 45° to the main slope surface (i.e. at 65° to the horizontal). The upper horizontal section is 15 m long, and 5 m high, whereas the inclined slope is over 45 m long. A total of 4600 elements are used and, within each element, 4 material points are placed initially. An idealised strain-softening model is assumed for the soil. The mean peak cohesion is 20.0 kPa, the softening modulus is -50.0 kPa, and the mean residual cohesion is 4.0 kPa. A coefficient of variation of 0.25 is assumed for both the peak and residual cohesions in the following first two cases considered; in other words, the residual cohesion is considered to be proportional to the peak cohesion throughout the simulation. The Young's modulus and Possion's ratio are $E = 1.0 \times 10^4$ kPa and $v = 0.33$, respectively. The soil self-weight is 20.0 kN/m$^3$ and, for simplicity, is considered as the triggering agent for the slope failure. The time step is $2.5 \times 10^{-3}$ s.

### 4.4.2. INFLUENCE OF SCALE OF FLUCTUATION

Fig. 4.10 shows typical random fields of the peak undrained shear strength, $c_u$, for the problem geometry. The details of obtaining random fields of $c_u$ for a complex geometry and material anisotropy can be found in Wong (2004). The scale of fluctuation in the vertical direction, $\theta_v$, is set to 0.5 m, and the degrees of anisotropy considered are 1, 12 and 48, respectively (i.e. the horizontal scale of fluctuation $\theta_h$ is taken as 0.5, 6.0 and 24.0 m, respectively, in which $\theta_h$ here represents the horizontal component of a larger value of $\theta$ acting parallel to the slope surface). A total time of 25 s is used for the three cases.

A deterministic analysis has also been carried out for comparison, as shown in Fig. 4.11, where successive rotational failure planes occur within a big sliding block, believed to be caused by a translational failure as demonstrated in section 3.6.

Fig. 4.12 shows the influence of soil heterogeneity on the slope post-failure behaviours (based on the random fields shown in Fig. 4.10). The slope with isotropic heterogeneity and a small scale of fluctuation, in Fig. 4.12(a), shows few differences in failure response compared to the homogeneous slope, shown in 4.11. The plastic strain invariant accumulates first along the base of the soil layer, to form the basal failure plane consis-
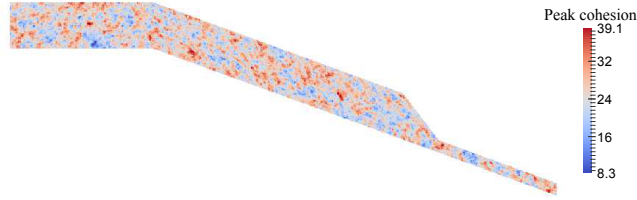
(a) $\xi = 1$, random field of peak cohesion (kPa)
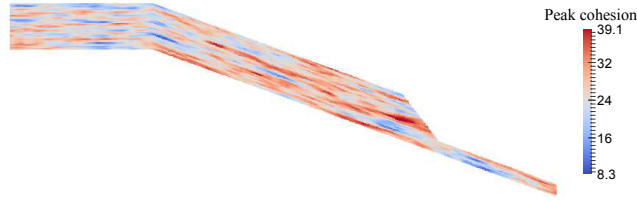


(b) $\xi = 12$, random field of peak cohesion (kPa)
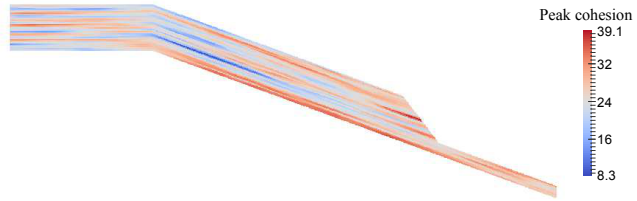


(c) $\xi = 48$, random field of peak cohesion (kPa)

Figure 4.10: Typical random fields for long inclined slopes with different degrees of anisotropy

tent with a large translational failure, while secondary failure surfaces form to break up the sliding mass, giving it a step-like character. Minor differences, such as the occurrence of a shear plane above the slope base, is due to the failure mechanism "seeking out" the least resistant path.

In Fig. 4.12(b), where the degree of anisotropy is 12, the failure of the main part of the slope can be divided into two parts. One part originates from the toe of the small cut slope and propagates, parallel to the base of the soil layer, upwards. The other part starts from the middle part of the soil layer base, where a relatively weaker zone is found, and propagates backwards to the crest between the horizontal and inclined sections. The first rotational failure and other secondary failure blocks are triggered after the initiation of the two translational sliding surfaces.

For the anisotropy of 48, the slope can be considered as layered, as demonstrated
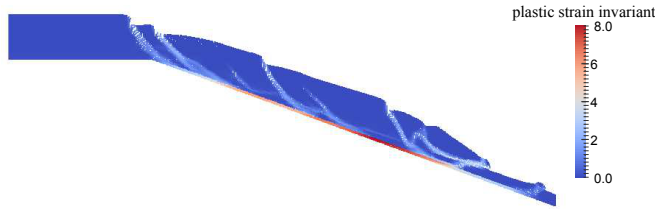
Figure 4.11: Plastic shear strain invariant contours for a deterministic analysis

by the cohesion distribution shown in Fig. 4.10(c). Three main features of the failure mechanism are worth noting. Firstly, it is clear that the critical translational slope failure forms without propagating along the base of the soil layer. Griffiths et al. (2011) and Li et al. (2014) also demonstrated that there is a possibility that the critical mechanism will occur above the base when the factor of safety is lower, although their investigations were restricted to 1-D analyses and the analyses were stopped at the onset of failure. Secondly, there are few secondary failure planes seen in the deformed slope body; the entire inclined part moves as a rigid body and there is no initial rotational failure, as commonly seen in the previous analyses. Thirdly, the start of a rotation failure in the horizontal section of the slope suggests that, even though a large horizontal scale of fluctuation has been applied, the failure mechanism is still related closely to the slope geometry, as also demonstrated by the translational failure that happens in the inclined part.

### 4.4.3. INFLUENCE OF SLOPE ANGLE

As shown in chapter 3, as the slope angle increases the failure modes can change significantly, from successive rotational failures for a shallower slope, to a large translational failure coupled with small secondary failures for a steeper slope. The slope geometry is proven to have a significant influence on the slope failure modes. This subsection continues to examine the slope failure mechanism under the influence of slope geometry, but for the case when a degree of anisotropy of $\xi = 48$ is applied. Four different slope angles, i.e. 5°, 10°, 15° and 20° are considered, and the vertical scale fluctuation is again set to 0.5 m. A total time of 25 s is set for the four analyses.

An example peak cohesion distribution within the slope for 20° is shown in Fig. 4.10(c). The same distribution has been applied to the other three slope angles, and the final failure configurations at $t = 25$ s for the different slope angles are shown in Fig. 4.13. Note that the failure mode for all 4 cases is primarily a big translational failure of the entire inclined part, followed by a subsequent breaking up within the entire moving soil body. Another thing in common is that the failures do not propagate along the base of the soil layer. The shear plane occurring at the lower part of the slope, through the weaker zones shown in the Fig. 4.10(c), forms the basal surface of the big translational failure.

For the shallower slopes shown in Fig. 4.13(a) and (b), i.e. 5° and 10°, the initial rotational slides at the toe area are still considered as the trigger for the following big translational slide. However, the rotational failures are very shallow, and do not propagate
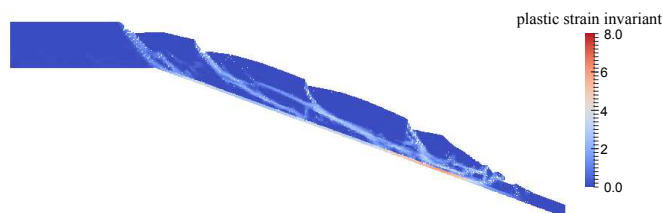
(a) $\xi = 1$, plastic shear strain invariant contours
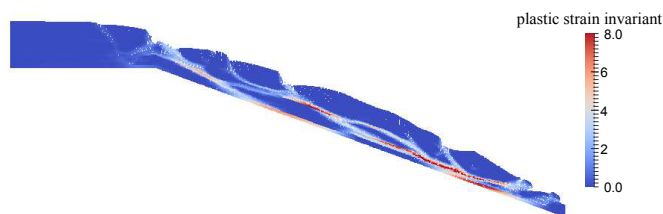


(b) $\xi = 12$, plastic shear strain invariant contours
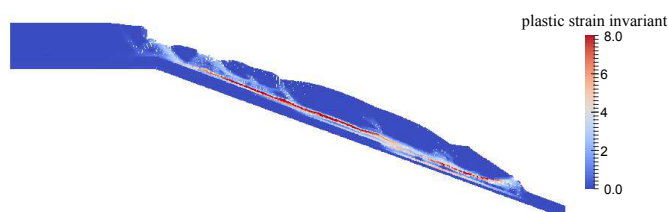


(c) $\xi = 48$, plastic shear strain invariant contours

Figure 4.12: Typical failure mechanisms for long inclined slopes with different degrees of anisotropy

to the slope base. The basal line of the subsequent translational failure starts from the slope toe, and develops parallel to the soil layer base, through the weak soil layer towards the upper part of the slope. Subsequent break-ups within the translationally moving soil body show no big difference from the deterministic solutions.

For the steeper slopes, i.e. 15° in Fig. 4.13(c) and 20° in Fig. 4.12(c), the big translational failure is considered to trigger the whole slope failure, as well as the secondary failure planes including the rotational failure occurring at the slope toe area. For the case of the 20° slope, a shear plane parallel to the basal line of the transaltional failure is developed at the rear part of the inclined slope, above which small failure zones are then formed, while the rest of the soil remains intact, which further indicates that the translational failure is the primary failure mode for the steeper slopes.

To conclude, the 4 cases yield quite similar failure patterns, although deterministic

(a) slope angle = 5°



(b) slope angle = 10°
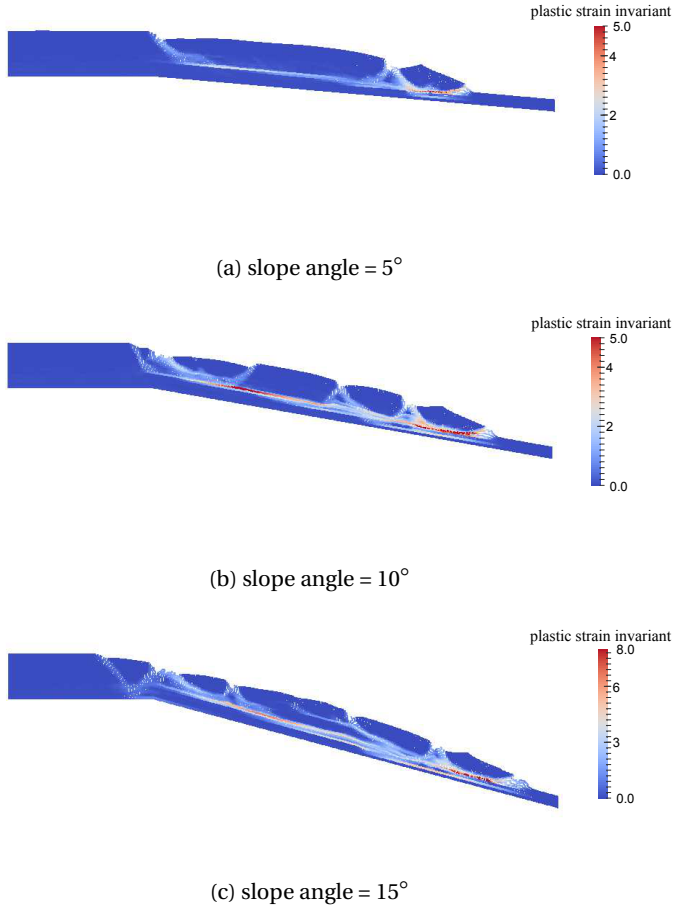


(c) slope angle = 15°

Figure 4.13: Failure configurations of long inclined slopes with different slope angles and $\xi = 48$

analyses for the same slope geometries, shown in Fig. 3.20, show quite different failure mechanisms. The sequence of the translational failure planes can vary with the slope angle, but undoubtedly, the influence of heterogeneity on the slope failure mechanism development is clear. However, no strong conclusions are made here, due to the problem being realisation-based.

### 4.4.4. INFLUENCE OF COEFFICIENT OF VARIATION

An interesting result is found by assuming that the mean and standard deviation of the undrained strength are directly proportional to the depth below the slope surface; that is, because failure is known to be independent of the slope depth for a homogeneous deposit, so that a greater range of failure surfaces are possible in a heterogeneous deposit (Hicks and Samy, 2002). In contrast to the layered slope presented in the previous

section, the cohesion distribution modelled in this section is more zone-based, i.e. a small degree of anisotropy. The scale of fluctuation in the vertical direction is 2.0 m and in the horizontal direction it is 3.0 m. Moreover, the mean undrained shear strength is assumed to increase linearly with the depth, starting at 5.0 kPa at the slope surface and reaching 25.0 kPa at the slope base. Two coefficients of variation ($V$), 0.2 and 0.4, are considered, while other parameters are the same as used above. The slope angle is set as 5°. The result obtained with a deterministic analysis is shown as a comparison, where the undrained shear strength is equal to the depth-dependent mean undrained shear strength from the heterogeneous slope. The running time is set as 100 s.
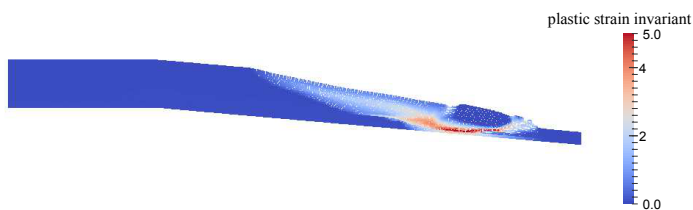


(a) deterministic solution
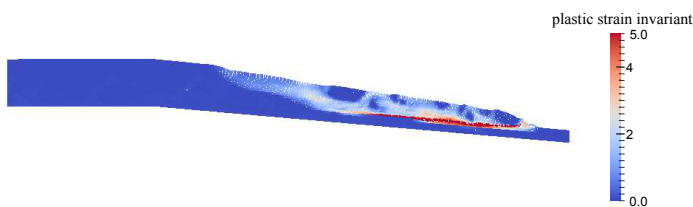


(b) $V = 0.2$
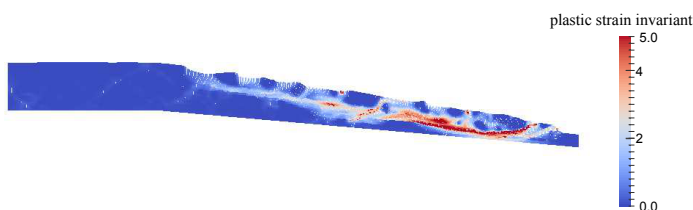


(c) $V = 0.4$

Figure 4.14: Failure configurations for long inclined slopes with different coefficients of variation and $\xi = 1.5$

The deterministic solution is shown in Fig. 4.14(a), where the initial slide is revealed to propagate through to the base of the soil layer and, after that, the soil mass behind it fails en masse. Fig. 4.14(b) and (c) show the results with heterogeneity incorporated. In

4.14(b), for $V = 0.2$, there are two key differences with respect to the deterministic case. Firstly, the failure is found to happen at a certain depth, rather than at the soil layer base, which is consistent with conclusion that slope failure is less dependent on soil depth for cases in which the soil properties vary with the depth (Hicks and Samy, 2002). Secondly, the failure is seen to be travelling backwards, with the plastic strain invariant contours explicitly showing separate failure blocks. At the far end of the failure, a portion of the soil layer is also shown to fail en masse. This is because, with the small anisotropy of the heterogeneity applied, the strength distribution within the soil layer is zone-based. Due to the failure mechanism "seeking out" the path of least resistance, the strong zones may be avoided in the failure evolution process, hence giving separate failure blocks, while, if the differences between the strong and weak zones are very limited, the soils tend to fail en-masse. The situation becomes clearer as $V$ is increased to 0.4, as in this case the weak zones are weaker and the stronger zones are stronger. Hence, the failure is able to travel backwards (as a sequence of blocks) more, as shown in 4.14(c) where a shallow step-like failure mode is apparent and bigger influential zones are observed. This demonstrates that, even in soil deposits containing very loose materials, retrogressive failure mechanisms may still be possible.

## 4.5. CONCLUSIONS

By incorporating random field theory, the random material point method (RMPM) is proposed, where, in contrast to RFEM, the random field cell values are assigned to the material points directly, rather than to Gauss points. Usually, RFEM has been restricted in its applicability to small deformation analyses, without considering very time consuming techniques for solving large strains; hence, the potential slope failure development cannot be described. In contrast, RMPM provides a good insight into slope post-failure behaviour.

Two types of slopes have been investigated in this chapter, i.e. a short slope and a long slope. For the short slope, heterogeneity is shown to have a strong effect on the slope failure mechanism, in particular regarding secondary failures and the extent of failure retrogression. Factors such as the scale of fluctuation and degree of anisotropy are mainly investigated, where a much larger influence zone is revealed by considering the soil heterogeneity compared to traditional deterministic analyses. The wedge formations in the failure development are well explained by considering the heterogeneity, as the failure path automatically seeks out the path of least resistance in avoiding the stronger zones. By equating the potential failure consequence to the sliding distance (i.e. extent), the deterministic analysis may yield an unconservative result (i.e. it may underestimate the possible risk). Moreover, RFEM solutions based on small deformations are mainly restricted to initial slope failures, thereby neglecting the effects of possible retrogressive and progressive failures.

For the long inclined slope, the influence of the heterogeneity on the slope failure mechanism is further highlighted. More specifically, the layered and zoned slopes are respectively modelled by assigning a large degree of anisotropy and a small one. The degree of anisotropy and slope geometry are investigated for slopes with depth-independent statistics, where it is shown that failure can occur without propagating down to the base of the soil layer; moreover, with a large degree of anisotropy, the failure modes,

regardless of slope angle, all yield big translational failures indicating a greater impact from the heterogeneity than the slope geometry. For the zoned slope based on depth-dependent statistics, the coefficients of variation are examined, reflecting differences in the relative influences of weak and strong property zones. The results are compared to deterministic analyses and, apart from further emphasising of the importance of the heterogeneity, it is demonstrated that retrogressive failure can also happen even within soil deposits containing very loose materials, when a big coefficient of variation is present.

**4**

# 5

# RAINFALL-INDUCED SLOPE FAILURES WITH COUPLED MPM

*Rainfall-induced slope failures are a major cause of slope failure, with incidents likely to increase with the predicted escalation of extreme rainfall events. Traditional numerical methods such as the finite element method (FEM) are often restricted in their applicability to small deformation analyses. Therefore, an incomplete description of the failure mechanism is given, in which the failure consequences, or evolving deformations and progressive failures, are ignored. A one-point, two-phase material point method (MPM) formulation is proposed to consider the influence of rainfall on slope failure. Due to the characteristics of MPM in capturing the large deformations, a complete failure process, from initiation to failure, of a slope subjected to rainfall infiltration is presented. The soil behaviour is described by a Mohr–Coulomb strain softening model based on Bishop's stress. The two-phase analysis shows that the rainfall-affected slope is initially stable, until the suction stresses are reduced leading to a superficial failure mode, which in turn leads to a complete slope failure.*

## 5.1. INTRODUCTION

Rainfall induced slope failure is widely studied, due to its importance in the geotechnical engineering field, although, as discussed already, most analyses have been restricted to the stage of small deformations, i.e. initial failure. To take account of the influence of water for such applications, the MPM formulation of previous chapters has been extended to a simplified one-point two-phase formulation. To describe the soil behaviour, the consitutive model is formulated within a Bishop's stress framework.

This chapter starts with an introduction to the MPM formulation for solving coupled dynamic, two-phase problems. The research continues the formulation proposed by Jassim et al. (2013) for fully saturated soils, and moreover, by considering the degree of saturation as a variable within the governing equations, a simplified one-point, two-phase unsaturated formulation for dynamic MPM is derived. For simplicity, the gas phase is omitted. A B-bar shape function is included to stabilise the pore pressure. Simple numerical examples are analysed to verify the formulation by comparing with analytical solutions. The same two slopes as in previous chapters, but now subjected to rainfall, are investigated and, once again, the slope failure mechanism is studied, from the failure initiation to the final quasi-static configuration. The importance of different parameters, such as boundary friction and capillary cohesion, are investigated: firstly, to show the robustness of the method with regard to large deformations; and secondly, to further understand their impacts on the potential slope failure consequences.

## 5.2. LITERATURE REVIEW

### 5.2.1. MECHANISM OF RAINFALL-INDUCED SLIDES

It is recognized that rainfall infiltration results in a rise of the groundwater table and an increase of the pore water pressure, or, in the decrease of matric suction in unsaturated soils (Cai and Ugai, 2004), which in turn causes a reduction in effective normal stress and thereby soil strength along the potential failure path (Brand, 1981; Fredlund and Rahardjo, 1993).

Numerous analyses have been conducted to investigate the effects of rainfall infiltration on slope stability. Results from Tsaparas et al. (2002) showed that, for the same rainfall, the higher the value of the saturated coefficient of permeability, the smaller the safety factor of the slope becomes due to a deeper wetting front. Chen et al. (2009) analysed a failed slope caused by heavy rainfall, near Taipei, using the limit equilibrium method, and showed that the rainfall intensity-time history is of great importance. Pradel and Raad (1993) proposed a method based on the Green-Ampt model, in which the critical rainfall intensity and duration for a rainfall induced slope failure could be approximated. Rahardjo et al. (2007) compared the relationship between rainfall intensity and minimum factor of safety for a homogeneous slope subjected to rainfall for 24h, and suggested that the ratio of intensity over saturated coefficient of permeability should be used, instead of using either of them alone. Xue and Gavin (2008) extended the Horton Equation and discussed the influence of rainfall intensity and pattern of rainfall (variation of rainfall intensity) on the infiltration response of a soil. By using three dimensional (3D) numerical analyses, Ng et al. (2001) investigated the groundwater responses due to various rainfall patterns, in which it was shown that the rainfall pattern has a signifi-

cant influence on pore-water pressures near the ground surface and that the influence gradually diminishes with depth. At a given depth, the influence of rainfall patterns on pore-water pressures depends on the initial groundwater conditions. Among the comparisons of different storm patterns, an advanced storm of 24 h duration was found to be the most critical. Rahardjo et al. (2001) analysed one of the failed slopes caused by a storm in February, 1995, on the Nanyang Technological University Campus, which demonstrated that antecedent rainfall plays an important role in slope stability, as the negative pore pressure can be reduced during rainfall, so that the slope may become marginally safe before the main storm.

Cascini et al. (2009) modelled a shallow landslide of the flow-type in Southern Italy, in which the landslide was divided into two stages; failure and post-failure. The failure stage is characterized by the formation of a continuous shear band through the soil mass (Leroueil, 2001). The post-failure stage is described by the rapid generation of plastic strains and the consequent sudden acceleration of the failed soil mass (Hungr, 2003). Relatively little research has been done so far to describe the post-failure stage (an exception being Pastor et al. (2004)), but such analyses can be considered particularly useful, as they contribute to the assessment of the landsliding volumes and their potential for traveling long distances (Cascini et al., 2009).

### 5.2.2. Multi-phase MPM modeling

The MPM modeling of coupled two-phase hydro-mechanical behaviour is still in its infancy. Following the FEM procedure, two main formulations (considering dynamic analysis only) can be identified, based on whether or not to include the inertial terms of the fluid phase. The full set of governing equations used in describing the dynamic motion is the $v - w$ formulation, where the velocities or displacements of the solid phase, and the fluid phase, e.g. water, are used as the primary variables. It can be used to represent the most general soil behaviour and is convenient for the finite element formulation, although it results in a large number of nodal unknowns (Zienkiewicz et al., 1980). An alternative simplification is also possible, where the primary variables are changed to the solid phase velocities, or displacements, and pore pressures, i.e. $v - p$ formulation. Van Esch et al. (2011) compared the two formulations, concluding that the time step size is more restrictive and that the second compression wave cannot be accurately captured when the $v - p$ formulation is applied. So far, most of the current MPM implementations have used $v - w$ formulations (Zhang et al., 2007; Abe et al., 2013; Jassim et al., 2013; Bandara and Soga, 2015) .

Zhang et al. (2007), to the author's knowledge, were the first to apply MPM for analysing porous media, where two sets of material points are invoked to represent the solid skeleton deformation and the pore fluid flow separately, and an equivalent $v - w$ formulation (displacement, to be more precise, as variables) was adopted. However, due to the same interpolation function being assumed for the solid and fluid material points, while including the solid-water interactive damping force, the formulation was restricted to small deformation analysis.

Jassim et al. (2013) also adopted the $v - w$ formulation, while the solid and fluid phases were represented by the same material point, with each taking a fraction of the material point domain. In contrast to Zhang et al. (2007), the linear momentum conser-

vations were made on the solid phase and the mixture. Following the procedure outlined by Verruijt (2009), the velocities for the fluid and solid phases were solved one after another. The material point positions were updated based on the velocities of the solid phase, while the water velocities were simply used for the pore pressure calculation. The enhancement of volumetric strains was used to mitigate spurious pressure fields and locking problems which may arise when using low-order elements. Stress integration was performed on the Gauss points, if at least 90% of the element area/volume was filled with material points; otherwise it was performed on the material points, so that a smooth stress variation could be achieved. This led to a violation of the mass conservation, due to the true material point volumes not being represented.

Abe et al. (2013) modeled a river levee experiment investigating seepage induced failure, with a proposed formulation involving two sets of material points, within which the relative accelerations of the fluid phase were neglected. The fluid velocities were calculated during each time step based on Darcy's law, and the simulation results matched the experiment data well.

Bandara and Soga (2015) derived their $v - w$ formulation based on mixture theory, with the key aspect of the formulation being that it considered two sets of material points. Pore pressure is calculated incrementally, and explicitly shown as a function of the volumetric strain of the two phases. Water table changes can be modeled via a straightforward calculation of the positions of the fluid material points. Progressive failures of an initially unstable river levee were simulated and, in particular, it included the first attempt to consider unsaturated soil behaviour using MPM.

Yerro et al. (2015) and Yerro (2015) continued the research by Jassim et al. (2013), and proposed a one-point, three-phase (solid, liquid, gas) formulation. The velocities of the gas, fluid and solid phases were calculated successively, based on the momentum balance equations on the gas phase, fluid phase and mixture. Due to the possibility of mass exchange between the fluid phases, the mass balance equation was formulated on each component (solid, water, air) rather than on each phase (solid, liquid, gas). A rainfall-induced slope instability was analysed, with the soil constitutive relationship described by a suction-dependent Mohr-Coulomb model. The evolution process of the slide was shown, providing an insight into the coupled flow-stress-strain mechanisms developing in the slope.

$v - p$ formulations (Zhang et al., 2009; Zabala and Alonso, 2011; Yerro, 2011; Lim et al., 2014) within the MPM framework were mainly developed during earlier periods. Zhang et al. (2009) proposed a coupled MPM formulation based on the $v - p$ form. Zabala and Alonso (2011) applied the method, coupled with a strain-softening Mohr-Coulomb elasto-plastic model, to simulate the construction and failure of the Aznalcollar dam, where the rupture process was captured and well matched to the actual field observations. However, due to the pore pressure integration in the element centre and the low-order element used, spurious pore pressures were possible during large deformations. To mitigate the volumetric locking encountered when using linear elements, Lim et al. (2014) implemented an alternative form of the Hu-Washizu weak form. An example of a spudcan foundation penetrating into a fully saturated soil was modelled.

## 5.3. FORMULATIONS FOR SATURATED SOILS

This section presents a brief introduction of the coupled MPM formulation for solving saturated soils, as a prerequisite for solving the partially saturated soils presented in the next section. Formulations, corresponding assumptions and numerical procedures are briefly listed below, and more details can be found in Van Esch et al. (2011) and Jassim et al. (2013).

### 5.3.1. BALANCE EQUATIONS

This section presents the mass and momentum balance equations for the liquid (water) and solid phases, with the mass balance equation for the solid skeleton initially, as

$$\frac{\partial(1-n)\rho_s}{\partial t} + \nabla(1-n)\rho_s \mathbf{v}_s = 0 \tag{5.1}$$

where $\rho_s$ is the density of the solid grains, $n$ is the porosity, $t$ is time, and $\mathbf{v}_s$ denotes the velocity of the solid particles.

By assuming the incompressibility of the solid grains, the material time derivative of the porosity can be simplified as,

$$\frac{\partial n}{\partial t} = (1-n)\nabla \cdot \mathbf{v}_s \tag{5.2}$$

The mass balance equation for the fluid phase is given by

$$\frac{\partial n\rho_w}{\partial t} + \nabla n\rho_w \mathbf{v}_w = 0 \tag{5.3}$$

where $\rho_w$ and $\mathbf{v}_w$ are the density and velocity of the fluid, respectively. Eq. (5.3) may be expanded using the chain rule, yielding

$$\rho_w \frac{\partial n}{\partial t} + n\frac{\partial \rho_w}{\partial t} + n\rho_w \nabla \mathbf{v}_w + \mathbf{v}_w \nabla n\rho_w = 0 \tag{5.4}$$

Substituting Eq. (5.2) into Eq. (5.4) to eliminate the material time derivative of the porosity, neglecting the spatial water density gradient, and dividing the whole equation by the water density $\rho_w$, the mass balance equation for the fluid reduces to,

$$\frac{n}{\rho_w}\frac{\partial \rho_w}{\partial t} + n\nabla \mathbf{v}_w + (1-n)\nabla \mathbf{v}_s = 0 \tag{5.5}$$

The momentum balance for the fluid is

$$n\rho_w \mathbf{a}_w = n\nabla p_w + n\rho_w \mathbf{b} - \frac{n^2\rho_w \mathbf{g}}{K} \cdot (\mathbf{v}_w - \mathbf{v}_s) \tag{5.6}$$

where $\mathbf{a}_w$ refers to the fluid acceleration, $p_w$ is the water pressure, $\mathbf{b}$ is the body force, and $K$ is the soil hydraulic conductivity. The last term in Eq. (5.6) refers to the fluid-solid interaction term, which is proportional to the fluid velocity relative to the solid velocity.

Using Biot's mixture theory, the momentum balance equation for the solid skeleton can be written as

$$(1-n)\rho_s \mathbf{a}_s = \nabla \cdot \boldsymbol{\sigma}'_s + (1-n)\nabla p_w + (1-n)\rho_s \mathbf{b} + \frac{n^2\rho_w \mathbf{g}}{k} \cdot (\mathbf{v}_w - \mathbf{v}_s) \tag{5.7}$$

where $\mathbf{a}_s$ is the solid acceleration and $\boldsymbol{\sigma}'_s$ represents the effective stress.

By adding Eqs. (5.6) and (5.7), the momentum balance equation for the entire mixture is

$$(1-n)\rho_s\mathbf{a}_s + n\rho_w\mathbf{a}_w = \nabla\cdot\boldsymbol{\sigma} + (1-n)\rho_s\mathbf{b} + n\rho_w\mathbf{b} \tag{5.8}$$

where $\boldsymbol{\sigma}$ is the total stress of the mixture, which can be defined as

$$\boldsymbol{\sigma} = \boldsymbol{\sigma}' + \mathbf{m}_k p_w \tag{5.9}$$

in which $\mathbf{m}_k$ is the Kronecker delta vector (for plane strain $[1\ 1\ 0\ 1]^\mathrm{T}$).

### 5.3.2. CONSTITUTIVE RELATIONS
The proposed constitutive relation for the density of the liquid is

$$\frac{1}{\rho_w}\frac{\partial\rho_w}{\partial t} = -\frac{1}{K_w}\frac{dp_w}{dt} \tag{5.10}$$

where $K_w$ is the bulk modulus of the water and is assumed to be constant. Substitution of Eq. (5.10) into Eq. (5.5) then leads to the rate of change of the water pressure,

$$\frac{dp_w}{dt} = \frac{K_w}{n}(n\nabla\mathbf{v}_w + (1-n)\nabla\mathbf{v}_s) \tag{5.11}$$

### 5.3.3. WEAK FORM OF THE GOVERNING EQUATIONS
The numerical procedures developed by Jassim et al. (2013) are used in this analysis. The momentum balance equations for the mixture and the fluid phase are considered, which includes all the acceleration terms. As in the single phase formulation, the weak form of the momentum balance equations can be obtained by multiplying Eqs. (5.6) and (5.8) with a test function $\mathbf{w}^h$ and integrating over the current configuration $\Omega$ surrounded by the boundary $\Gamma$.

The Cauchy boundary conditions for the solid and liquid phases are

$$\sigma\cdot\mathbf{n} = \boldsymbol{\tau} \tag{5.12}$$

$$p_w\cdot\mathbf{n} = \bar{\mathbf{p}}_w \tag{5.13}$$

where $\boldsymbol{\tau}$ and $\bar{\mathbf{p}}_w$ are the prescribed stresses and pore pressures on the boundary. The term involving the stress is integrated by parts and the divergence theorem is also applied. The momentum balance equation for the fluid phase gives

$$\int_\Omega \mathbf{w}^h\cdot\rho_w\mathbf{a}_w d\Omega =$$
$$\int_\Gamma \mathbf{w}^h\cdot\bar{\mathbf{p}}_w d\Gamma - \int_\Omega \nabla\mathbf{w}^h : p_w d\Omega + \int_\Omega \mathbf{w}^h\cdot\rho_w\mathbf{b}d\Omega - \int_\Omega \mathbf{w}^h\cdot\frac{n\rho_w g}{k}\cdot(\mathbf{v}_w - \mathbf{v}_s)d\Omega \tag{5.14}$$

and the momentum balance equation for the mixture is obtained in a similar way as

$$\int_\Omega \mathbf{w}^h\cdot n\rho_w\mathbf{a}_w d\Omega + \int_\Omega \mathbf{w}^h\cdot(1-n)\rho_s\mathbf{a}_s d\Omega =$$
$$\int_\Gamma \mathbf{w}^h\cdot\tau d\Gamma - \int_\Omega \nabla\mathbf{w}^h : \sigma d\Omega + \int_\Omega \mathbf{w}^h\cdot n\rho_w\mathbf{b}d\Omega + \int_\Omega \mathbf{w}^h\cdot(1-n)\rho_s\mathbf{b}d\Omega \tag{5.15}$$

### 5.3.4. MPM DISCRETISATIONS

The material point method (MPM) discretises a continuum body into a finite set of material points that are tracked throughout the deformation process, rather than using Gauss points within an FEM framework. As reported in the previous section, the shape functions are utilized to link the properties on the background mesh nodes with those on the material points. Eqs. (5.14) and (5.15) can then be discretised in matrix form as

$$\mathbf{M}_w \mathbf{a}_w = \mathbf{F}_{trac,w} + \mathbf{F}_{grav,w} - \mathbf{F}_{int,w} - \mathbf{F}_{drag,w} \tag{5.16}$$

and

$$\mathbf{M}_s \mathbf{a}_s = -\bar{\mathbf{M}}_w \mathbf{a}_w + \mathbf{F}_{trac} + \mathbf{F}_{grav} - \mathbf{F}_{int} \tag{5.17}$$

where the construction of such matrices in the above equations is detailed as follows.

In practice, the lumped mass matrices $\mathbf{M}_w$, $\mathbf{M}_s$ and $\bar{\mathbf{M}}_w$ are normally used for simplicity, which are assembled element-wise as

$$\mathbf{M}_\alpha = \sum_{iel=1}^{nels} \mathbf{M}_{\alpha,e} \tag{5.18}$$

where $\alpha$ represents $w$, $s$; with

$$\mathbf{M}_{\alpha,e} = \begin{bmatrix} \mathbf{M}_{\alpha,1} & \mathbf{0} & \cdots & \mathbf{0} & \cdots & \mathbf{0} \\ \mathbf{0} & \mathbf{M}_{\alpha,2} & \cdots & \mathbf{0} & \cdots & \mathbf{0} \\ \vdots & \vdots & \ddots & \vdots & \vdots & \vdots \\ \mathbf{0} & \mathbf{0} & \cdots & \mathbf{M}_{\alpha,i} & \cdots & \mathbf{0} \\ \vdots & \vdots & \vdots & \vdots & \ddots & \vdots \\ \mathbf{0} & \mathbf{0} & \cdots & \mathbf{0} & \cdots & \mathbf{M}_{\alpha,n_e} \end{bmatrix} \tag{5.19}$$

In the above matrix, each diagonal term corresponds to a node $i$, $n_e$ is the number of nodes per element and the matrix $\mathbf{0}$ is a null matrix. In plane strain problems, the mass matrix is defined as

$$\mathbf{M}_{\alpha,i} = \begin{bmatrix} m_{\alpha,i} & 0 \\ 0 & m_{\alpha,i} \end{bmatrix} \tag{5.20}$$

in which $m_{\alpha,i}$ is the projected nodal mass from the corresponding material points, and $\bar{m}_{w,i}$ is a mass matrix factored by the solid porosity for convenience of the computation,

$$m_{w,i} = \sum_{p=1}^{N_p} m_{w,p} N_i(\mathbf{x}_p) \tag{5.21}$$

$$\bar{m}_{w,i} = \sum_{p=1}^{N_p} n_p m_{w,p} N_i(\mathbf{x}_p) \tag{5.22}$$

$$m_{s,i} = \sum_{p=1}^{N_p} (1 - n_p) m_{s,p} N_i(\mathbf{x}_p) \tag{5.23}$$

where $n_p$ represents the porosity of the solid skeleton at a material point $p$, $m_{w,p}$ and $m_{s,p}$ are the masses for water and solid particles, respectively, $N_p$ is the number of material points within an element, and $N_i(\mathbf{x}_p)$ is the shape function on the $i$th node with respect to the material point located at position $\mathbf{x}_p$.

For simplicity, the remaining terms are described from the element point of view. The body forces (i.e. gravity) are integrated as

$$\mathbf{F}_{grav,w} = \sum_{p=1}^{N_p} \mathbf{N}^{\mathrm{T}}(\mathbf{x}_p) \mathbf{f}_{w,p}^{grav} \tag{5.24}$$

and

$$\mathbf{F}_{grav} = \sum_{p=1}^{N_p} \mathbf{N}^{\mathrm{T}}(\mathbf{x}_p) \mathbf{f}_p^{grav} \tag{5.25}$$

where $\mathbf{F}_{grav,w}$ is the vector of gravity forces acting on the water, and $\mathbf{F}_{grav}$ is the total gravity force accounting for both the water and solid skeleton. $\mathbf{f}_{w,p}^{grav}$ and $\mathbf{f}_p^{grav}$ are calculated using $\mathbf{f}_{w,p}^{grav} = m_{w,p} \cdot \mathbf{g}$ and $\mathbf{f}_p^{grav} = m_p \cdot \mathbf{g}$, where $\mathbf{g}$ is the gravitational acceleration vector which can be expressed as $\mathbf{g} = (0.0, -10.0)^{\mathrm{T}}$.

The traction on the boundary nodes can normally be applied in two ways: (1) the tractions are applied onto the particles located near the boundary first and then, by using the shape functions, the mapped tractions on the nodes can be obtained; (2) the tractions can be enforced on the boundary nodes, where the boundary is assumed to move along with the deformation. The first way is adopted in this study. $\mathbf{F}_{trac}$ and $\mathbf{F}_{trac,w}$, corresponding to the total nodal force and water force applied on the boundary, are assembled as

$$\mathbf{F}_{trac} = \sum_{p=1}^{N_{blp}} \mathbf{N}^{\mathrm{T}}(\mathbf{x}_p) \mathbf{f}_p^{trac} \tag{5.26}$$

and

$$\mathbf{F}_{trac,w} = \sum_{p=1}^{N_{blp}} \mathbf{N}^{\mathrm{T}}(\mathbf{x}_p) \mathbf{p}_{w,p} \tag{5.27}$$

where $N_{blp}$ is the number of material points within the vicinity of the boundary.

The internal force $\mathbf{F}_{int}$, and the internal force due to the water pressure $\mathbf{F}_{int,w}$, are expressed as

$$\mathbf{F}_{int} = \sum_{p=1}^{N_p} (\mathbf{B}_L^{\mathrm{T}}(\mathbf{x}_p) \boldsymbol{\sigma}_p) \cdot V_p \tag{5.28}$$

and

$$\mathbf{F}_w^{int} = \sum_{p=1}^{N_p} (\mathbf{B}_L^{\mathrm{T}}(\mathbf{x}_p) \mathbf{p}_{w,p}) \cdot V_p \tag{5.29}$$

where $\mathbf{p}_{w,p}$ and $\boldsymbol{\sigma}_p$ are, respectively, the water pressure and total stress calculated on the material points directly.

The drag force describes the interaction between the soil skeleton and water particles, and is defined as,

$$\mathbf{F}_{drag,w} = \mathbf{Q}(\mathbf{v}_w - \mathbf{v}_s) \tag{5.30}$$

with $\mathbf{Q}$ being a lumped matrix, and the sub-entry associated with each node $i$ on the diagonal line being given by

$$\mathbf{q}_i = \sum_{p=1}^{N_p} \frac{m_{w,p} n_p \mathbf{g}}{k} N_i(\mathbf{x}_p^t) \tag{5.31}$$

### 5.3.5. NUMERICAL PROCEDURES WITHIN A COMPUTATIONAL CYCLE

For solving the momentum balance equations, i.e. Eqs. (5.15) and (5.16), a discretisation in time is necessary. An explicit time integration is chosen in this formulation for obtaining the numerical solution at each discrete time. Compared to the more widely used $v - p$ form in FEM analyses, the choice of time step size is reported to be less restrictive (Van Esch et al., 2011) when using the $v - w$ form, and moreover, the implementation itself is more straight-forward. The two-phase coupled MPM algorithm is summarised as follows:

(1) Initialization of all the variables on the nodes.
(2) Acceleration of the water phase is solved using Eq. (5.16).
(3) Acceleration of the solid phase is obtained thereafter using Eq. (5.17).
(4) The velocities of the two phases on the nodes are updated using the explicit forward Euler method.
(5) The velocities of the two phases on the material points are updated, and then the positions of the material points based on the calculated velocities are updated.
(6) The velocities on the nodes are updated by mapping back from the material points, and then the stresses and water pressures on the material points are calculated.
(7) The background mesh is reset, and the next computation cycle is initiated.

### 5.3.6. NUMERICAL EXAMPLE

A consolidation example is presented here, with the result validated against Terzaghi's one dimensional consolidation theory (Terzaghi, 1943) to demonstrate the applicability of the coupled MPM code for a saturated problem.

Fig. 5.1(a) shows the details of the numerical model, where a 1.0 m high and 0.1 m wide soil column, fully saturated with water is considered. A 10 kPa traction is applied on the column surface (at the boundary nodes due to the small deformation). The two sides and bottom are assumed to be impermeable, while the water is allowed to drain out from the top surface. The column is discretized using 10 4-node quadrilateral elements, of dimension 0.1 m × 0.1 m. Soil behaviour is modeled using an isotropic linear elastic material and the following material properties are considered: Young's modulus, $E = 1.0 \times 10^4$ kPa; Poisson's ratio, $v = 0.0$; solid grain density, $\rho_s = 2.65 \times 10^3$ kg/m$^3$; initial solid porosity, $n_0 = 0.3$; initial hydraulic conductivity, $K = 1.0 \times 10^{-3}$ m/s; water density, $\rho_w = 1.0 \times 10^3$ kg/m$^3$; bulk modulus of water, $K_w = 2.2$ GPa. The simulation is carried out using a time step size of $\Delta t = 1.0 \times 10^{-7}$ s for a total duration of 1.0 s.

Fig. 5.1(b) compares the computed MPM results with Terzaghi's solution. The isochrones in the figure are plotted for various values of the time factor $T_v$, which is defined as

$$T_v = \frac{c_w t}{h_v^2} \tag{5.32}$$

where $h_v$ is the thickness of the soil layer and $c_w$ is the consolidation coefficient, given by

$$c_w = \frac{k}{\rho_w g(\frac{1}{E} + \frac{n}{K_w})} \tag{5.33}$$

Although the applied low-order elements make the pore pressure constant within an element, resulting in a step-like character to the pore pressure profiles, overall there is a reasonable agreement between the two solutions.



(a) schematic diagram of the test

(b) pore pressure profiles as a function of time
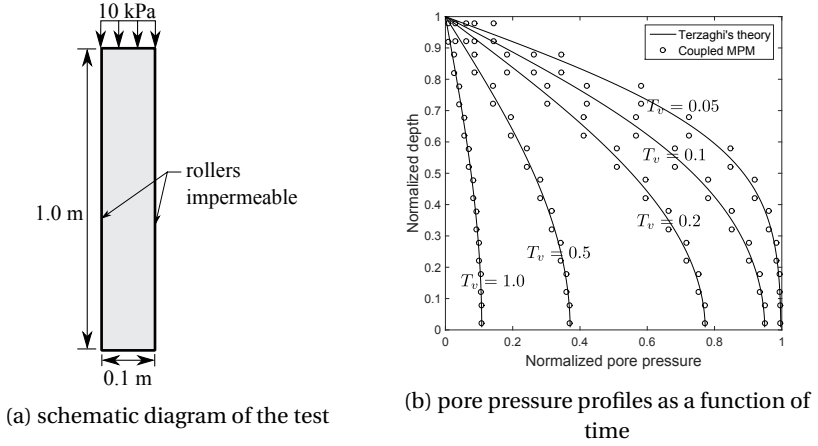
Figure 5.1: One-dimensional consolidation test

## 5.4. MODELLING UNSATURATED SOILS

The formulation is further developed in this section for being able to simulate the behaviour of unsaturated soils. For simplicity, the gas phase is neglected. By introducing the degree of saturation to characterize the soil-water relationship, a simplified one-point, two-phase (solid, liquid) formulation is constructed. Formulations and corresponding assumptions are briefly described first, and an infiltration example is shown to validate the unsaturated formulation.

### 5.4.1. CONSERVATION OF SOIL MASS

As for saturated soils, the soil mass conservation is described as

$$\frac{\partial(1-n)\rho_s}{\partial t} + \nabla(1-n)\rho_s v_s = 0 \tag{5.34}$$

By neglecting the gradient of porosity, and assuming the solid skeleton as incompressible, Eq. (5.34) can be simplified as,

$$\frac{\partial n}{\partial t} = (1-n)\nabla v_s \tag{5.35}$$

### 5.4.2. CONSERVATION OF FLUID MASS

The conservation of the fluid (water) is expressed as

$$\frac{\partial n S_w \rho_w}{\partial t} + \nabla n S_w \rho_w v_w = 0 \tag{5.36}$$

where $S_w$ is the degree of saturation of the soil. By using the chain rule, the above equation is expanded as

$$S_w \rho_w \frac{\partial n}{\partial t} + n \rho_w \frac{\partial S_w}{\partial t} + n S_w \frac{\partial \rho_w}{\partial t} + n S_w \rho_w \nabla v_w + v_m \nabla n S_w \rho_w = 0 \tag{5.37}$$

Substituting Eq. (5.35) into Eq. (5.37) to eliminate the material time derivative of the porosity, neglecting the spatial water density gradient, and dividing the whole equation by the water density $\rho_w$, the mass balance equation for water reduces to,

$$n \frac{\partial S_w}{\partial t} + \frac{n S_w}{\rho_w} \frac{\partial \rho_w}{\partial t} + n S_w \nabla v_w + (1-n) S_w \nabla v_s = 0 \tag{5.38}$$

Assuming a barotropic behaviour for the fluid, its intrinsic density variation is given by

$$\frac{1}{\rho_w} \frac{\partial \rho_w}{\partial t} = -\frac{1}{K_w} \frac{dp_w}{dt} \tag{5.39}$$

Experimental evidence indicates that the degree of saturation of the soil with respect to the liquid phase, $S_w$, is a function of the suction $s$ and the hydraulic history of the soil, which can be represented by the so-called soil water retention curve (SWRC). A simple reversible law proposed by Van Genuchten (1980) is adopted here to relate the so-called effective degree of saturation $S_e$ to the suction $s$, i.e.

$$S_e(s) = \begin{cases} (1 + (\alpha_s s)^{n_s})^{-(1-1/n_s)} & \text{if } p_w \leq 0 \\ S_{sat} & \text{if } p_w > 0 \end{cases} \tag{5.40}$$

in which $\alpha_s$ and $n_s$ are fitting parameters, and the effective degree of saturation is defined as

$$S_e = \frac{S_w - S_{res}}{S_{sat} - S_{res}} \tag{5.41}$$

where $S_{res}$ and $S_{sat}$ are the residual degree of saturation in dry conditions and the degree of saturation at full saturation (which is taken to be 1.0 for most cases).

Hence, the time derivative of the degree of saturation can be written as

$$\frac{\partial S_w}{\partial t} = \frac{\partial S_w}{\partial s} \frac{\partial s}{\partial t} = -\frac{\partial S_w}{\partial s} \frac{dp_w}{dt} = -\lambda \frac{dp_w}{dt} \tag{5.42}$$

where $\lambda$ equals $\frac{\partial S_w}{\partial s}$. Substituting Eqs. (5.35), (5.39) and (5.42) into Eq. (5.38), after simple algebraic manipulation the water pressure can be obtained as,

$$\frac{dp_w}{dt} = \left(n\lambda - n\frac{S_w}{K_w}\right)^{-1} (n S_w \nabla v_w + (1-n) S_w \nabla v_s) \tag{5.43}$$

### 5.4.3. Momentum conservation for water

The momentum equations for unsaturated soils are virtually the same as the saturated ones:

$$\rho_w \mathbf{a}_w = \nabla p_w + \rho_w \mathbf{b} - \frac{n S_w \mu_w}{k} \cdot (\mathbf{v}_w - \mathbf{v}_s) \tag{5.44}$$

where $k$ stands for the soil permeability and $\mu_w$ is the water viscosity. The SWRC can be used to describe the relation between soil permeability and its degree of saturation. It is common in literature to express the actual permeability value at a certain suction level as a fraction of its value at full saturation, i.e.

$$k(S_w) = k_{sat} \cdot k_{rel} \tag{5.45}$$

where $k_{rel}$ is the relative permeability, which is the ratio between the actual permeability and the permeability at full saturation, and can be calculated according to the Van Genuchten (1980) formula,

$$k_{rel} = \sqrt{S_e} \left[ 1 - \left( 1 - S_e^{\,n_s/(n_s-1)} \right)^{1-1/n_s} \right]^2 \tag{5.46}$$

### 5.4.4. Momentum conservation for the mixture

As in Eq. 5.8, the momentum conservation for the mixture is

$$(1-n)\rho_s \mathbf{a}_s + n S_w \rho_w \mathbf{a}_w = \nabla \cdot \boldsymbol{\sigma} + (1-n)\rho_s \mathbf{b} + n S_w \rho_w \mathbf{b} \tag{5.47}$$

in which, apart from the water body force being multiplied by the degree of saturation, Bishop's effective stress is also utilised in the calculation of the total stress $\boldsymbol{\sigma}$, i.e.

$$\boldsymbol{\sigma}' = \boldsymbol{\sigma} - \mathbf{m}(\chi p_w) \tag{5.48}$$

where $\chi$ is an effective stress parameter called the matric suction coefficient and varies from 0 to 1 covering the range from dry to fully saturated conditions. For convenience, $\chi$ is simplified to equal to the degree of saturation, $S_w$, in the following calculations. $\mathbf{m}$ is the vector $[1101]^{\mathrm{T}}$ for 2D plane strain analysis.

### 5.4.5. Computing the solid skeleton's porosity

The porosity of the soil is updated after each time step based on the deformation gradient as follows:

$$n(\mathbf{x}_p, t + \Delta t) = 1 - \frac{(1 - n(\mathbf{x}_p, t))}{J(\mathbf{x}_p, t + \Delta t)} \tag{5.49}$$

where $J$ is the Jacobian of the deformation gradient tensor, and can be approximated by the trace of the strain tensor, i.e. $J = 1 + tr(\boldsymbol{\epsilon})$, when small deformation is ensured within each time step.

The degree of saturation and permeability are updated according to the specific soil-water retention curve.

Using the same discretization techniques and numerical procedures outlined for saturated soils in section 5.3.5, the same final governing equation forms can be obtained, except for the coupling terms which need to include the degree of saturation.

#### 5.4.6. Infiltration example

For validating the coupled MPM code for unsaturated soils, the laboratory test by Liakopoulos (1964) is analysed. The experiment was performed on a column of Del Monte sand, which was initially fully saturated by adding water from the top continuously. The water supply ceased at the start of the experiment. The two side walls were impermeable to water, while the water was able to freely drain from the bottom. The tensiometers instrumented along the column height were used to measure the moisture tension during the desaturation due to gravity. The schematic diagram of Liakopoulos' test is shown in Fig. 5.2, where the initial and boundary conditions are defined. For simplicity, the gas pressure is assumed to equal atmospheric pressure in the unsaturated zone.
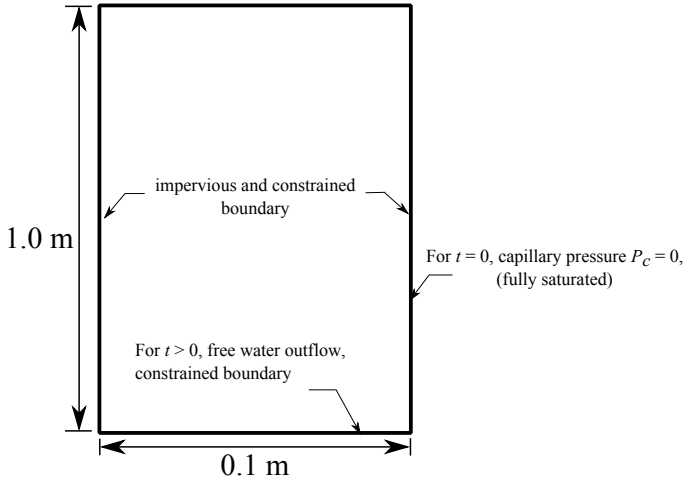


Figure 5.2: The Liakopoulos (1964) test problem

The material properties are given in Table 5.1. The relationships for saturation-capillary pressure and relative permeability-saturation, valid for saturation $S_w \geq 0.91$, take the following forms (Lewis and Schrefler, 1998):

$$S_w = 1 - 1.9722 \times 10^{11} p_c^{2.4279} \tag{5.50}$$

$$k_{rl} = 1 - 2.207(1.0 - S_w)^{1.0121} \tag{5.51}$$

For the numerical calculations, the column of sand was divided into 10 4-node quadrilateral elements of size 0.1 m × 0.1 m. The time step size was set to $5.0 \times 10^{-6}$s. The results of the simulation at different times, i.e. the water saturation, vertical displacement and capillary pressure, are shown and compared in Fig. 5.3. Small strain analysis is utilised in the calculation due to the small vertical displacement observed. A gradually decreasing outflow rate is expected, which corresponds to the smaller changing rate of the degree of saturation at the top of the specimen. The reasonable agreement between the computed and experimental results demonstrates the applicability of the model for unsaturated soils.
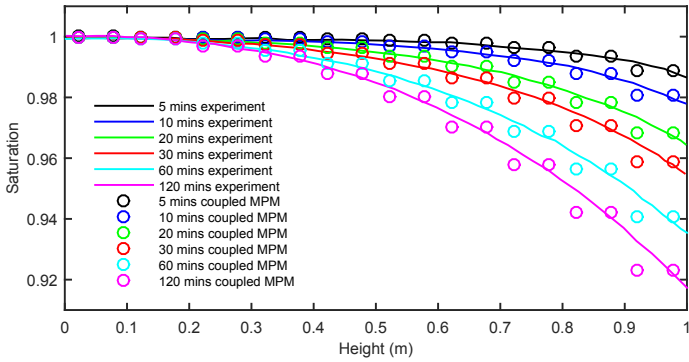
(a) saturation versus height
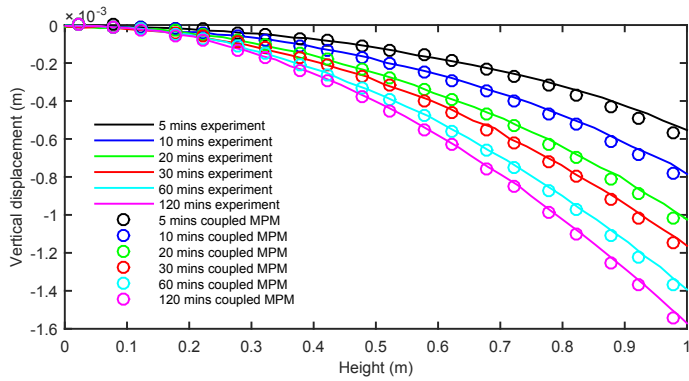


(b) vertical displacement versus height
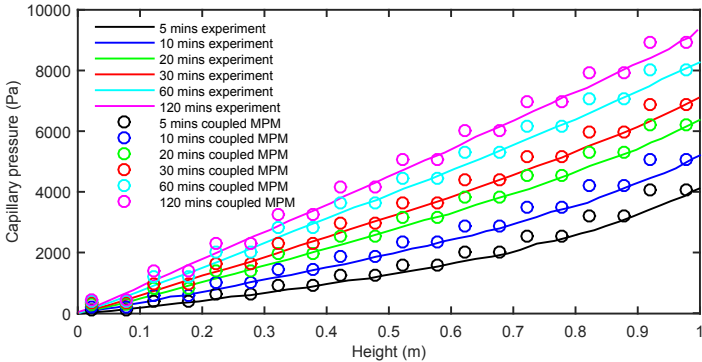


(c) capillary pressure versus height

Figure 5.3: Comparisons between MPM and experimental results

| Parameters | Values |
|---|---|
| Young's modulus (kPa) | $1.3 \times 10^3$ |
| Possion's ratio | 0.4 |
| Solid grain density (kg/m$^3$) | $2.0 \times 10^3$ |
| Liquid density (kg/m$^3$) | $1.0 \times 10^3$ |
| Porosity | 0.2975 |
| Intrinsic permeability (m$^2$) | $1.0 \times 10^{-13}$ |
| Water viscosity (Pa · s) | $1.0 \times 10^{-3}$ |
| Gravitional acceleration (m/s$^2$) | 9.806 |

Table 5.1: Material properties for the analysis of Liakopoulos' test (Lewis and Schrefler, 1998).

## 5.5. A RAINFALL-INDUCED SHORT SLOPE FAILURE

A rainfall-induced short slope failure is first analysed to give a straight-forward view of the development of retrogressive failure as water infiltrates into the slope. The characteristics of the example soil slope are reviewed first, including the slope geometry, material model and soil-water retention curve. The collapse process of the soil slope is given thereafter.

### 5.5.1. CHARACTERISTICS OF THE EXAMPLE SOIL SLOPE
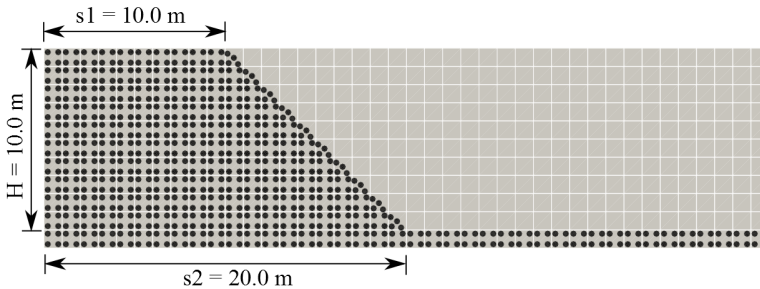


Figure 5.4: Initial geometry of the short slope

Fig. 5.4 shows the slope geometry, with the slope height being 10 m and the slope angle being 45°. The distance from the slope crest to the left-side boundary is 10.0 m. For modelling the contact in between the slope base and the ground, the rough contact, inherent in the material point method, is used due to its simplicity. Hence, a layer of material points is set at the bottom of the domain to model the contact. The material points are initialised on the Gauss points positions. After that, the original mesh is discarded and a new computational (background) mesh, shown in light grey, is defined by discretizing the background into squares of size 1.0 m × 1.0 m. A total of 440 4-node quadrilateral elements is used for the background mesh. Rollers allowing only vertical displacement are prescribed for both lateral boundaries of the domain, and the bottom boundary is fully fixed.

A suction-dependent Mohr-Coulomb model, i.e. using Bishop's stress, is adopted to

describe the soil response, in which the cohesion is assumed to decrease proportionally with the equivalent plastic strain invariant, until reaching the residual value, as illustrated in section 3.4. The friction angle and dilation angle remain constant. The material properties are summarised in Table 5.2. As seen from the table, the intrinsic permeability in this example is $4.5 \times 10^{-9}$ m$^2$, which is nearly 4000 times the permeability used for the analysis in Fig. 5.1; hence, the ratio of permeability over water viscosity is much larger, which is proportional to the time step size. Therefore, the time step size for the simulation is selected as $1.0 \times 10^{-4}$ s.

| Parameters | Values |
|---|---|
| Young's modulus (kPa) | $1.0 \times 10^3$ |
| Possion's ratio | 0.33 |
| Solid grain density (kg/m$^3$) | $2.7 \times 10^3$ |
| Liquid density (kg/m$^3$) | $1.0 \times 10^3$ |
| Porosity | 0.3 |
| Intrinsic permeability (m$^2$) | $4.5 \times 10^{-9}$ |
| Water bulk modulus (kPa) | $1.0 \times 10^6$ |
| Water viscosity (Pa $\cdot$ s) | $1.0 \times 10^{-3}$ |
| Peak cohesion (kPa) | 20.0 |
| Residual cohesion (kPa) | 0.1 |
| Friction angle (°) | 20.0 |
| Dilation angle (°) | 0.1 |

Table 5.2: Material properties for the slope analysis

The van Genuchten law, as given in Eqs. (5.40) and (5.46), is utilised to describe the relations between the degree of saturation, $S_w$, the permeability of the soil with respect to the fluid phase, $k$, and the pore water pressure. $S_{sat}$ and $S_{res}$ are taken to be 1.0 and 0.23 for the following analysis. The two fitting parameters, $\alpha_s$ and $n_s$, are 0.44 and 3.04, respectively, which are typical values for a sandy silt (Abed, 2008). The corresponding van Genuchten curve is shown in Fig. 5.5.

## 5.5.2. RAINFALL-INDUCED SLOPE FAILURE

The numerical simulation has two steps: (1) gravity loading to generate the in-situ stresses and the application of an initial prescribed suction of 50.0 kPa, where the pore pressures are allowed to equalise until an in-situ hydrostatic condition is achieved; and (2) a zero pore water pressure applied to the slope surface to model continuous water infiltration into the slope, until either a slope failure occurs or an equilibrium condition is reached.

For simplicity, the suction was initially assumed to be constant throughout the slope; and, for modelling the fully saturated soil at the boundary, zero pore pressure is applied to the material points located in the surface elements and maintained throughout the simulation. The disadvantage of dealing with the boundary in this way is that it may cause some unrealistic outcomes, as material points may move a long distance and end up as non-boundary material points. This aspect will be the subject of a future investigation.
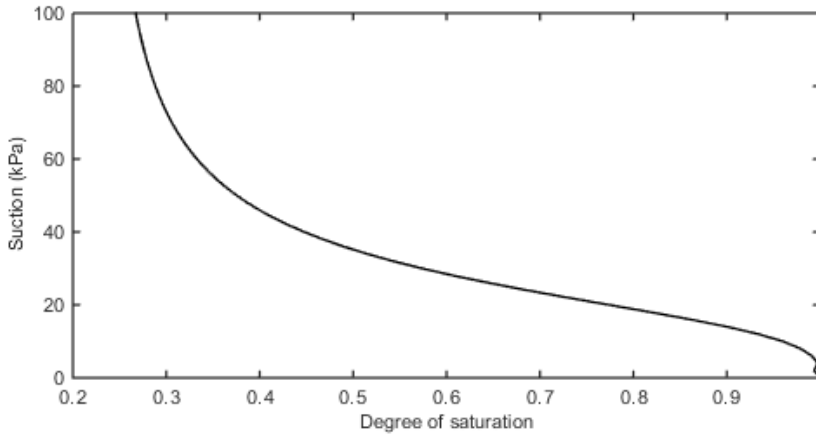
Figure 5.5: Soil-water retention curve considered for the analysis
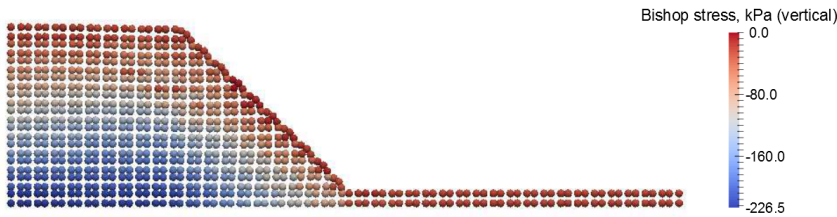


Figure 5.6: Stress distribution within the slope at the end of step 1

The stress distribution within the slope at the end of step 1, i.e. when an equilibrium state was reached under the applied gravity and prescribed suction on the slope, is shown in Fig. 5.6. This serves as a starting stress state for step 2. As the water infiltrates into the slope continuously, the failure is initiated.

Fig. 5.7(a) - (c) shows the slope failure process due to rainfall infiltration from the slope surface, up to a time of 16.0 s from when the rainfall starts. Due to the rainfall infiltration at the slope surface, three successive failures are observed during the evolution process, shown in Fig. 5.7(a), (b) and (c), corresponding to $t = 8.0$ s, 12.0 s, and 16.0 s, respectively, with plastic shear strain invariant contours shown on the material points. Two things may be noted: (1) the failure is retrogressive; (2) the last two failures are mainly occurring in the previous deposited soils from the initial slide, as the maximum strain invariants are seen on the top parts and base of the disturbed slope. The remaining soil is only slightly affected during the process, as was also previously observed in the column

collapse example presented in section 2.2.4 (see Fig. 2.16), which is mainly attributed to the soil properties, but also partly due to the proximity of the left-hand boundary in this example. However, the sliding distance is seen to be mainly caused by the initial slide by comparing the Figs. 5.7(a) and (c).
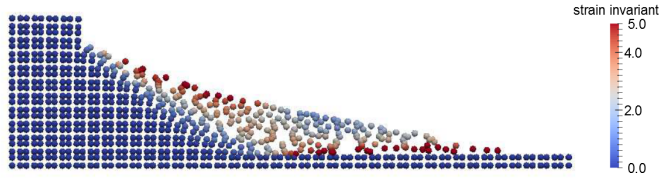


(a) $t = 8.0$ s
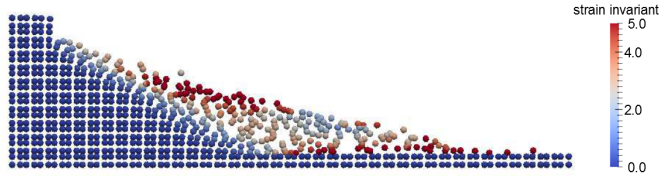


(b) $t = 12.0$ s
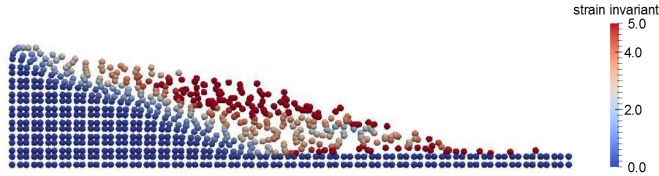


(c) $t = 16.0$ s

Figure 5.7: Collapse process of a short slope

As a comparison, Fig. 5.8 presents the final configuration, (when a quasi-static equilibrium state is reached), of the slope under gravity loading using a total stress analysis. There is only one failure block occurring, without the retrogressive failures shown in the previous figure. Although the adopted computational mesh is very crude, the differences in the solutions when using different numerical tools are apparent. The retrogressive failures occurring in the rainfall-induced slope collapse may be better described using the coupled MPM.
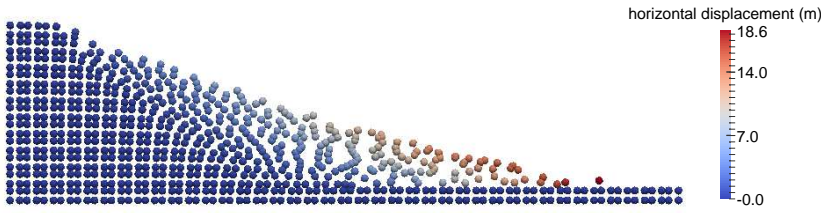
Figure 5.8: Short slope collapse with a total stress analysis

## 5.6. INFLUENCE OF RAINFALL ON A LONG INCLINED SLOPE FAIL-URE

The failure process of a rainfall-induced long slope is shown in this section. The retrogressive failure process, as often seen in reality, occurring with time as water infiltrates into the slope is provided. The general characteristics of the slope are described first, including the slope geometry. Comparisons with a total stress analysis (without considering pore pressure) are shown to emphasize the important role of rainfall in the slope failure initiation, as well as the failure propagation. The influence of soil friction angle and residual cohesion on the slope failure mechanism are discussed last.

### 5.6.1. PROBLEM DESCRIPTION

Fig. 5.9 shows the slope geometry, as described in previous chapters. The slope angle is set as 30°. The model is discretised by using 842 4-node quadrilateral elements, with 4 material points per element initially, resulting in a total of 3368 material points representing the slope. The simulation stops when failure is fully developed in the inclined part.

The soil properties and material model are as stated above. The simulation procedure also follows the previous example, where an initial −50 kPa pore pressure is prescribed to the slope body to maintain the equilibrium under gravity loading, and then a constant zero pore pressure is assigned to the surface material points for modelling the rainfall infiltration, to trigger the slope collapse.
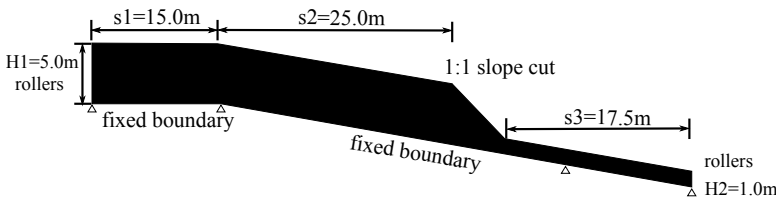


Figure 5.9: Initial geometry of the slope (not to scale)

## 5.6.2. COLLAPSE PROCESS

Fig. 5.10 shows the collapse process of the slope when subjected to rainfall infiltration, where the plastic shear strain invariant contours are shown on the right-hand-side of the figure, and the pore pressure contours are shown on the left-hand-side, at five different times. The analysis used a time step size of $5.0 \times 10^{-5}$ s to avoid non-convergence in the large deformation phase and a high permeability has been chosen for illustrative purposes. Using an Intel Xeon E5-1620 processor, the analyses take approximately 3-4 hours to execute on a single core.

In Fig. 5.10(a,b), i.e. $t = 8.75$ s, an initial failure occurs at the slope surface as this part of the slope becomes fully saturated, which implies an increase of the pore pressure and hence a decrease in the soil strength. As this small body of soil moves downslope, lateral support is removed from the soil upslope and the soil continues to saturate, and a wedge-shaped soil block forms through both the saturated and unsaturated parts (Fig. 5.10(c, d)). At $t = 16.25$ s (Fig. 5.10(e, f)), the soils within the saturated zone in the upper part of the slope are seen to fail, giving an impression of superficial slope failures leading to larger slope failures. Due to the change in the slope geometry, retrogression within the slope cross-section is able to continue, as seen with a further failure initiating at $t = 18.75$ s (Fig. 5.10(g, h)). Fig. 5.10(i, j) shows the situation at $t = 25.0$ s, when a slope failure has developed throughout the full length of the slope, although initially made up of a series of individual failures. Note that the material 'piles up' against the right-hand boundary, due to the prescribed size of the background mesh and the roller boundary condition, which have been included in the analysis to reduce the computation time.

The shear stress distributions within the slope at four distinct times are shown in Fig. 5.11. It is seen that the stress remains relatively unaffected in zones far from the failure planes. Moreover, the stresses are seen to be largest either side of the shear plane. The shear stresses within previous sliding soil blocks, when a new failure plane is forming, are shown to decrease. This may correspond to the observations made for the single-phase slope failure process in section 3.5; i.e. these parts of soil experience stress unloading, and are governed by the residual shear strength thereafter. Stress oscillations exist, which are mostly seen near the right hand boundary, as in Fig. 5.11 (c) and (d), and are thought to be mainly affected by the prescribed roller boundary, although integration at sub-optimal (non-Gaussian) points and the imcompressibility of the soil in saturated conditions are also likely to have contributed to the oscillations seen in Fig. 5.11 (a) and (b). This could be the subject of future research, in order to improve the robustness of the method for a better description of the failure.

During the analysis, most of the failures are seen to initiate in the saturated zone, with other failures being partly through the unsaturated zone. As the infiltration depth of the water becomes deeper, e.g. via an intense rainfall event, the failure depth of the soil is also seen to increase.

In this example, rainfall-induced progressive failure occurs partly due to the progressive loss of strength, but also due to changing geometry, which, for example, may remove lateral support from the soil behind. Moreover, the rainfall-induced slope collapse was shown to be more superficial than that in total stress analyses.

(a) pore pressure at $t = 8.75$ s

(b) plastic strain invariant at $t = 8.75$ s

(c) pore pressure at $t = 12.5$ s

(d) plastic strain invariant at $t = 12.5$ s

(e) pore pressure at $t = 16.25$ s

(f) plastic strain invariant at $t = 16.25$ s

(g) pore pressure at $t = 18.75$ s

(h) plastic strain invariant at $t = 18.75$ s

(i) pore pressure at $t = 25.0$ s

(j) plastic strain invariant at $t = 25.0$ s
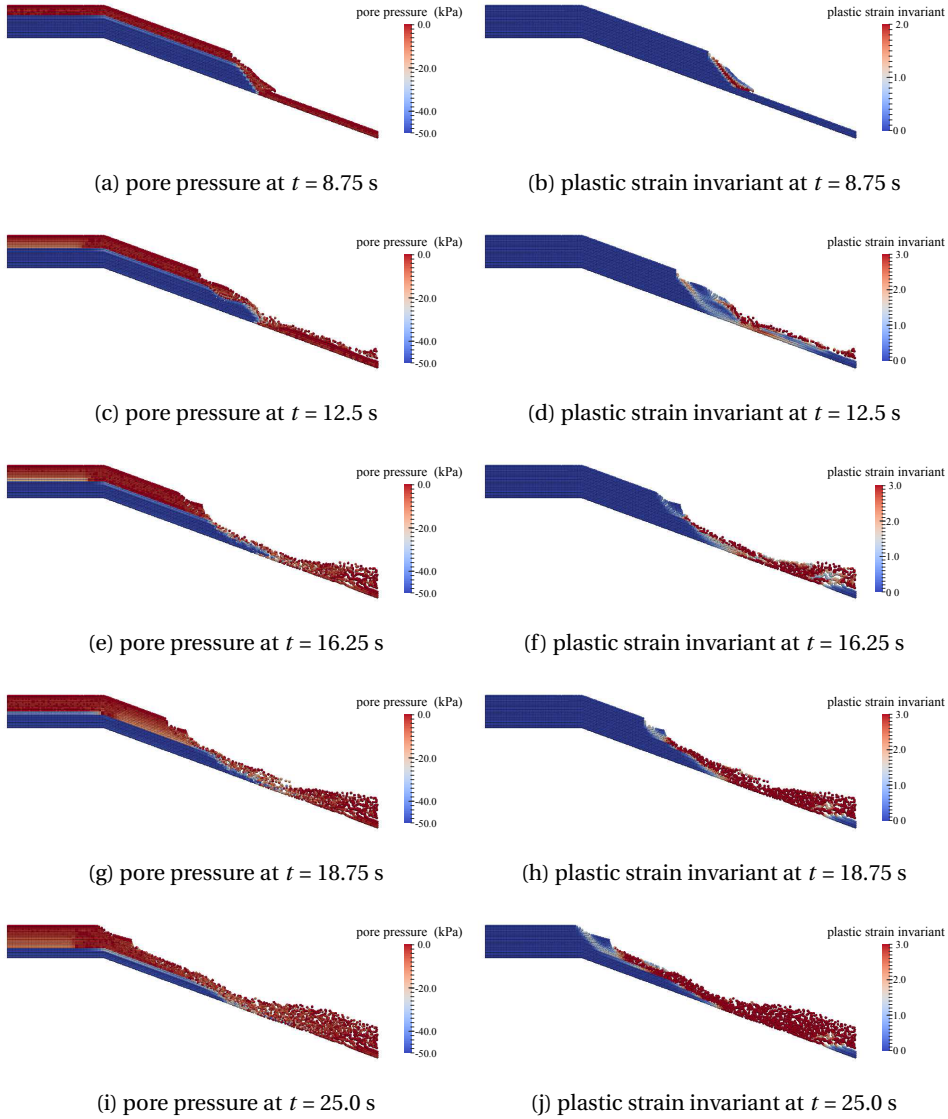
Figure 5.10: Rainfall induced slope collapse process in terms of pore pressure and plastic shear strain invariant contours

(a) $t = 10.0$ s

(b) $t = 12.0$ s



(c) $t = 16.25$ s

(d) $t = 25.0$ s
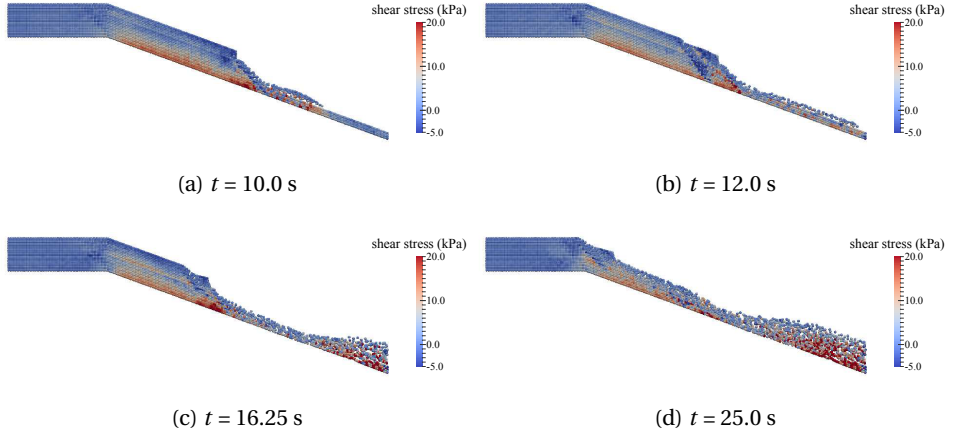
Figure 5.11: Shear stress states at material points at different times

**5**

### 5.6.3. COMPARISON WITH A TOTAL STRESS ANALYSIS

A total stress analysis has been undertaken for comparative purposes based on the same material parameters as above. Without any suction, the slope is initially unstable and the failure is triggered by gravity.

The progression of the slope failure at two different times is shown in Fig. 5.12. At $t = 0.5$ s, Fig. 5.12(a) shows two complete shear bands forming inside the slope; that is, a rotational slip in the down-slope part, and a translational slide over the whole slope length. The two shear bands are formed almost simultaneously and both failures reach the base of soil layer. In contrast to the retrogressive failure caused by the slope geometry change, as seen in the rainfall-induced slope collapse, the slope failure here is mainly a translational failure of almost the entire slope. Fig. 5.12(b) shows the configuration of the deformed slope at time $t = 2.0$ s, where it is seen that the soil body is mainly moving along the two shear bands.

Two things can be concluded, based on Fig. 5.12. Firstly, it shows that the slope experiences mainly a translational failure; this differs from the rainfall-induced slope failure shown in Fig. 5.10, where the retrogression occurs inside the slope. Secondly, the initial failure volume/area is much larger than for the rainfall-induced slope failure.

### 5.6.4. INFLUENCE OF THE FRICTION ANGLE

In this section, the influence of the friction angle on the slope failure mechanism is discussed. Apart from the 20° case described above, friction angles of 15° and 30° have also been considered, with all other material properties kept the same as in Table 5.2.

Fig. 5.13 shows the slope failure process when the friction angle equals 30°. As above, the plastic shear strain invariant contours are shown on the right-hand-side, and the pore pressure contours are shown on the left-hand-side. The failure initiates on the slope surface, as shown in Fig. 5.13(a, b), when the surface soils become fully saturated. Due to the lateral support removed from the soils upslope, and the continuing saturation of the
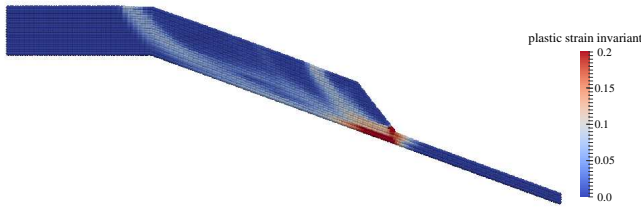
(a) plastic strain invariant at $t = 0.5$ s
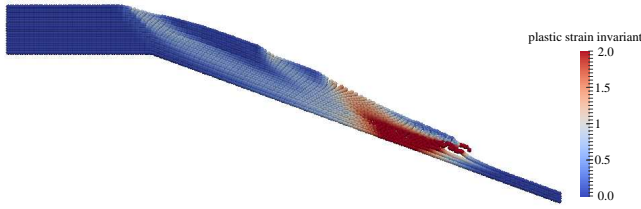


(b) plastic strain invariant at $t = 2.0$ s

Figure 5.12: Plastic shear strain invariant contours showing slope collapse using a total stress analysis

soil, a series of retrogressive failures is seen to occur in the superficial zones of the slope. In contrast to the 20° case, the failure only occurs inside the saturated zones, without propagating through the unsaturated zones, as shown in Fig. 5.13(c, d), which could be due to the higher resistance from a higher friction angle. The retrogression is seen to stop at a certain point, while a big translational slide is shown to form, covering the whole inclined part, when the slope is shown to be fully saturated, as illustrated in Fig. 5.13(e, f). Secondary failures are then seen to be forming within the moving mass, which resembles the failure modes under undrained conditions as shown in Fig. 5.12.

For a friction angle of 15°, a different failure mode may be obtained as shown in Fig. 5.14. In Fig. 5.14(a, b), as the water starts to infiltrate into the soil, in contrast to the superficial failures in the saturated zones exhibited for the two larger friction angles, an initial circular failure plane is seen to form in the downslope area. Strength loss is also expected along the failure surface, represented by the large plastic shear strain invariant. As part of soils slide downslope, the whole inclined slope failure is triggered, which is shown by a failure plane propagating down to the slope base through the whole inclined area. The soil mass then dislocates into smaller volumes/areas, which results in the slope appearance having a step-like character, as shown in Fig. 5.14(c, d). Water is, however, only accumulated in very shallow areas due to the shorter time required for full failure to develop. Note that the slope was initially stable under gravity and the prescribed suction force.

To conclude, the soil friction angle is shown to have a significant impact on the slope failure mechanism. Most of the failures are seen to initiate and then retrogress back-

(a) pore pressure at $t = 6.25$ s

(b) plastic strain invariant at $t = 6.25$ s

(c) pore pressure at $t = 25$ s

(d) plastic strain invariant at $t = 25$ s

(e) pore pressure at $t = 36.5$ s

(f) plastic strain invariant at $t = 36.5$ s
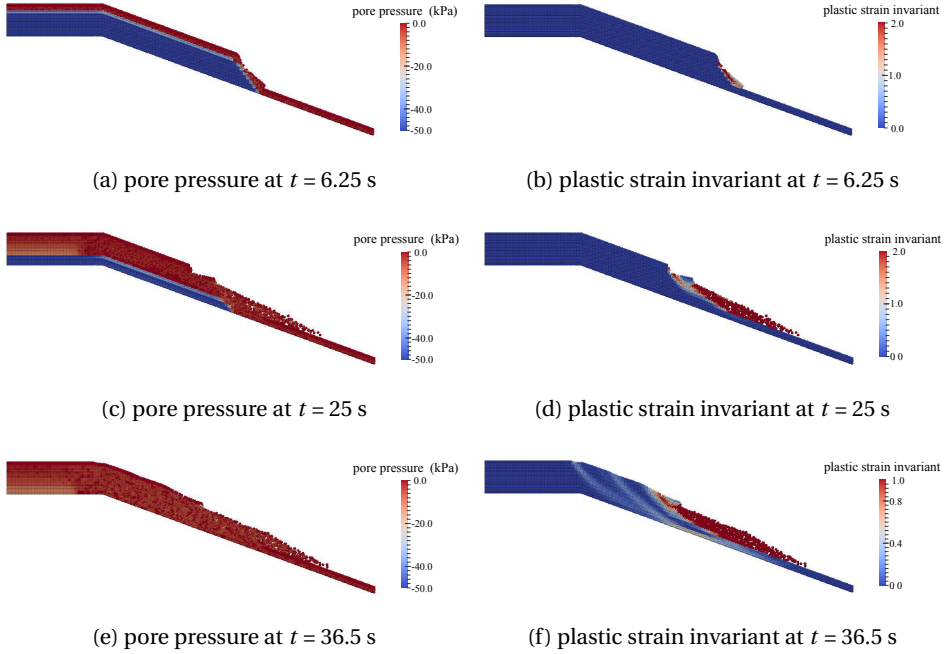
Figure 5.13: Rainfall induced slope collapse for friction angle equal to 30°

wards and upwards within the saturated zones during the infiltration process. As the friction angle increases, i.e. giving a higher soil resistance, the slope is more likely to experience a superficial failure, which is constrained within the saturated zones. However, as the infiltration process continues, a whole slope collapse could be possible in a very similar manner to the undrained condition, leading to a big translational slide followed by a series of secondary failures. The retrogressive failures reported in clayey-type soils are seen to be possible as the friction angle decreases. This could be partly due to the sudden soil weight increase as the surface soils become saturated.

### 5.6.5. INFLUENCE OF RESIDUAL COHESION

Fig. 5.15 shows the final configurations of the slope collapse, when the failure is developed fully in the inclined part of the slope, for the residual cohesion set to 0.01 kPa and 5.0 kPa. Other material properties are the same as for the base case.

Fig. 5.15(a, b) provides the slope final configuration for the case of a residual cohesion of 0.01 kPa, which shows very little difference in response to the base case, i.e. a steep rear scarp is normally completely exposed prior to the development of the next slide. As some soil slides away, the lateral support to the soils upslope is reduced sufficiently, hence initiating the next failures in the sequence. Fig. 5.15(c, d) shows the failure mechanism for the slope with a residual cohesion of 5.0 kPa. It is worth noting that the shallow slips are occurring successively in a retrogressive way, even though the rear scarp

(a) pore pressure at $t = 2.5$ s



(b) plastic strain invariant at $t = 2.5$ s



(c) pore pressure at $t = 5.0$ s



(d) plastic strain invariant at $t = 5.0$ s
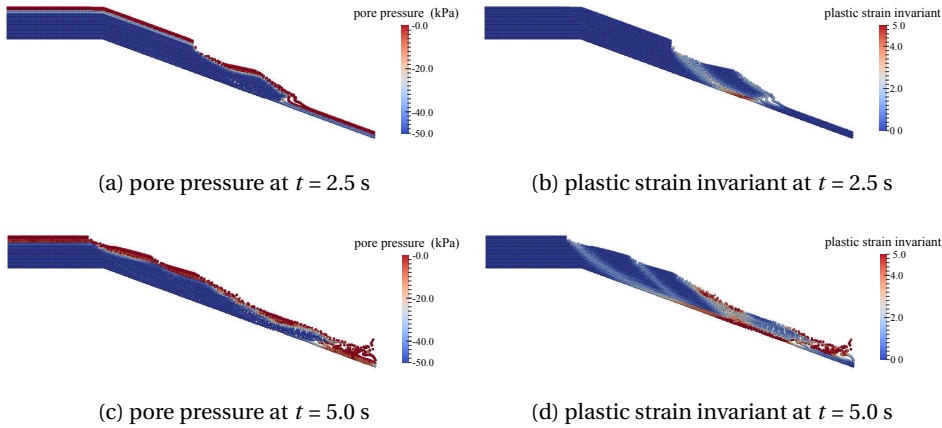
Figure 5.14: Rainfall induced slope collapse for friction angle equal to 15°

is not completely exposed. It is different from the case illustrated in Fig. 5.13(f), when a big translational slide is shown first, followed by secondary failures that form within the moving mass. As stated in Thomson and Hayley (1975) and Van Asch et al. (1984), a slight movement of soil blocks can cause sufficient reductions of the lateral support and hence lead to retrogressive failures.



(a) pore pressure at $t = 25.0$ s for residual cohesion of 0.01 kPa



(b) plastic strain invariant at $t = 25.0$ s for residual cohesion of 0.01 kPa



(c) pore pressure at $t = 28.75$ s for residual cohesion of 5.0 kPa



(d) plastic strain invariant at $t = 28.75$ s for residual cohesion of 5.0 kPa
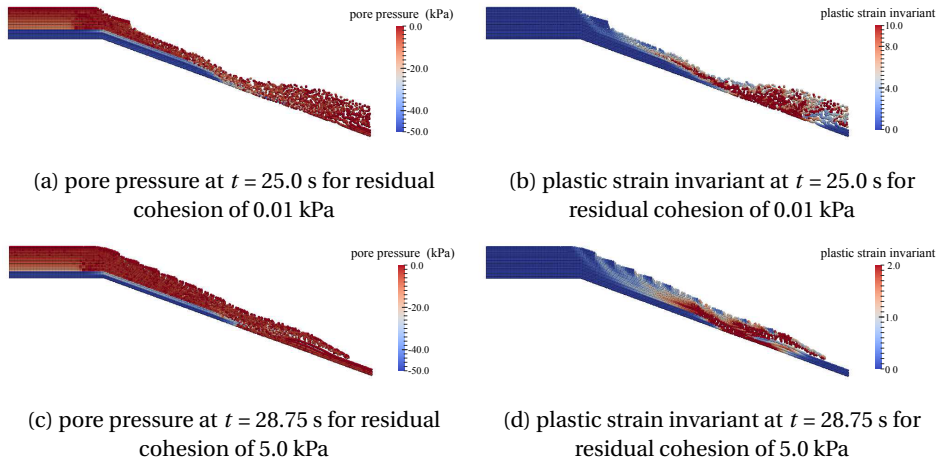
Figure 5.15: Influence of residual cohesion on slope failure mechanism

The soil strength can be decomposed into the cohesive strength (i.e. bonding forces in between the soil grains) and the frictional strength (Hajiabdolmajid and Kaiser, 2003). With a smaller residual cohesion, the cohesive strength can be almost completely removed, and the strength is then almost proportional to stress. In this case a diffuse fail-

ure occurs and no distinct back-scarp remains. With a higher residual cohesion, a steep rear scarp is left and the soils behind may become unstable and hence the next failure is initiated. As the cohesion increases, the cohesive strength of the soil lessens the sliding distance during the slope failures. This gives a similar failure pattern as normally observed in clayey-type soils, as reported in Van Asch et al. (1984).

## 5.7. Conclusions

The formulation of the coupled material point method is presented and further developed in order to describe the response under loading of unsaturated soils. A 1-D consolidation test and an infiltration problem have been presented to validate the formulation. With the method, an initial investigation of rainfall-induced slope failures has been presented. The method has been able to simulate slope failure from initiation through to the post-failure processes. Two slope geometries are discussed. For the smaller slope, the emphasis was to show the differences between using a total stress analysis and coupled MPM. The retrogressive failures of the slope during the rainfall infiltration process are observed when using coupled MPM, while only a single shear failure plane is shown in the slope final configuration when the total stress analysis is utilised.

For the long inclined slope, the rainfall-induced failure is shown to be formed by a series of mainly superficial failures, as are often observed in practice. This retrogressive failure mode is very different from that obtained in a total stress analysis, where a large translational slide is obtained for the slope geometry considered. Parametric studies regarding friction angles and residual cohesion have been conducted. With a higher friction angle, the slope may fail due to a large translational slide during an intensive rainfall event (making the slope saturated within a short time), without showing retrogression during the infiltration process. As the friction angle decreases, the retrogression is more obviously seen, through both saturated and unsaturated zones. As for the influence of the residual cohesion, it is shown that when a higher residual cohesion is assigned, shallow successive slips are exhibited without the complete exposure of the rear scarp during the failure process. In contrast, a smaller cohesion may lead to steeper rear scarps being exposed. It is thought that the coupled MPM, with further development, can be utilised to investigate a wide range of slopes at risk of rainfall-induced failure, including multiple and progressive failures.

# 6

# CONCLUSIONS AND OUTLOOK TO FUTURE WORK

## 6.1. CONCLUDING REMARKS

This thesis presents a number of theoretical and numerical developments, as well as a series of numerical analyses, to investigate the behaviour of slopes during failure. The work has concentrated on the development and implementation of the material point method and its application to slope failures.

The consequence of slope failures comes not only from the failure initiation, but in many cases from the development of the failure and flow of the failed material. From past studies of slope failures and landslides, a number of types of failure have been described, including translational failures, rotational failures, retrogressive failures and progressive failures. The behaviour of these failures after initiation depends strongly on the material behaviour and geometric changes during the failure.

To tackle the numerical simulation of slope failures, the material point method has been further developed and implemented. Three main developments have been presented: (a) the implicit material point method (IMPM) has been developed, in order to potentially save computation time and allow advantages in the accuracy of the material model; (b) the random material point method (RMPM) has been proposed and implemented, to enable the analysis of both heterogeneity and large deformations in slope failure analysis; and (c) the coupled material point method (CMPM) has been developed, with the aim to model the slope failure and its consequence due to the triggering of pore water pressure changes within soils, such as due to rainfall, etc.

The research has focused on the reproduction of commonly seen failure modes of clayey-type slopes, and in analyses of the underlying failure mechanisms, although simple slope geometries are included to facilitate the interpretation. A series of simple geometric analyses have been undertaken, utilising simple material models which are able to reproduce a range of different failures observed in reality.

Specifically, the main achievements of the research are summarised as follows:

Initially, the thesis presents the development and implementation of an IMPM formulation. A unified implicit MPM framework, in which both quasi-static and dynamic analyses can be solved, was proposed. The majority of other versions of MPM reported in literature have utilised an explicit time integration scheme, which requires strict time step control and thereby increases the computational cost and time. It has been found that, by utilising the implicit integration scheme, an improved algorithm accuracy can be found, which is important for some constitutive behaviours such as elasto-plasticity.

Various aspects of the IMPM implementation were tested and reported, including the numerical stability of elements which are not full (i.e. of material points), the number of material points per element and the energy conservation in the system. However, as is often the case in the finite element method, the conditions for a satisfactory solution are dependent on the problem considered and cannot be determined a priori. Particular attention should be paid to some parameters chosen in the simulations, e.g. the damping parameter. The analysis of a soil column collapse revealed that a parameter of 0.15 gives a reasonable fit to experimental results.

The developed and implemented IMPM was applied to slope instability analyses. To enable the simulation of post-failure behaviour, a constitutive model including post-failure behaviour was required, and so a simple idealized cohesion-softening model was introduced. Two main scenarios are presented and used throughout the thesis: (a) a

relatively small slope, similar to a cutting, and (b) a long slope, similar to a natural slope. Regarding the small slope, the slope geometry change is seen to have a big influence in the slope failure mechanism. As the previous slide moves far away from the initial conditions, rendering the exposure of a steepened scarp behind it, the force imbalance can be transferred backwards and trigger other slides. The constitutive model stages governing the behaviour of material points can be observed during the slope collapse process. It can be seen that the strength loss does not occur simultaneously throughout the slope, but according to the stress state and the accumulated plastic strain. There are two observations worthy of note: firstly, when a block of soil moves out of the sliding area, the exposed soil at the back scarp experiences elastic unloading; secondly, as a new shear band is formed, the soils within the previous shear band(s) remain at the residual state or elastically unload. Observations on the collapse process of a long inclined slope reveal that multiple slides can occur simultaneously, and that, based on the slope angle, two types of slope failure can be categorised. For gentler slopes, a retrogressive failure mode, with individual failure blocks forming wedge structures, is observed, whereas, for steeper slopes, a large translational slide is observed, with the soil mass subsequently breaking up.

For considering the effects of spatial variability of soil strength properties on slope failure mechanisms, including secondary failure mechanisms and the consequences of failure, a variant of the random finite element method (RFEM) has been proposed, called the random material point method (RMPM). RMPM combines random field theory, for modelling spatial variability, with the material point method (MPM) for modelling geotechnical response, within a Monte Carlo simulation process. It differs from RFEM by assigning random field (cell) values to material points, rather than to Gauss points. Comparisons with RFEM, through the analysis of an idealised small slope, showed that RMPM provides a much wider range of solutions, in general increasing the volume of material in the failure, while a comparison with the deterministic MPM solution showed that the deterministic analysis may yield unconservative results and underestimate the possible risk, based on equating the potential failure consequence to the sliding distance (i.e. extent). For a long inclined slope and a large degree of anisotropy, the failure surface was found to propagate above the slope base due to the soil heterogeneity. Coefficients of variation were examined to demonstrate that retrogressive failure could also happen within soil deposits containing very loose materials. Note that mesh dependency as expected (i.e. FEM variant) is observed in the code performance, and hence a study concerning the problem should be carried out before proceeding to Monte-Carlo simulations, in order to ensure that results are consistent.

Coupled MPM was implemented in order to consider the influence of pore water pressure change in the slope failure mechanism under saturated loading conditions. By introducing the degree of saturation to characterize the soil-water relationship, the model has been extended to include unsaturated soil behaviour. The developed model uses a single material point representing the material mass and the water moves through the points. The rainfall-induced slope collapse process was shown to be progressive and retrogressive using the coupled MPM approach, thereby resembling reality; in contrast, total stress analyses yielded unrealistic results that were independent of water flow with time in the soil, further highlighting the importance of utilising the coupled MPM in

solving related topics in the future. Rainfall induced slope failures are observed in the form of a series of mainly superficial failures.

## 6.2. RECOMMENDATIONS FOR FUTURE WORK

The material point method has been shown to be a reliable and useful numerical tool in geotechnical analyses and designs. However, the development of MPM is still at an early stage. A few recommendations for future research within the scope of this thesis are as follows:

- Implicit MPM shows a certain superiority in solving quasi-static large deformation problems, with the high-order element being integrated to reduce the stress oscillations. However, without the inertial terms included, the stability of the code is reduced. A soft-stiffness across the background mesh and a higher number of material points are needed to improve the code performance. A simple cantilever beam problem was considered within the thesis, which gives a case-dependent result. In the future, a more generalised result could be obtained by including more benchmark problems, although an absolute generalised solution would be very difficult to obtain due to the limitations and characteristics of each problem.

- Stress oscillations are problems inherent in MPM formulations, due to the integrations on the moving material points, cell crossing errors, etc., which may bring potential bad influences to the program performance. Many ways to combat this problem have been proposed, such as GIMP, integrations on the Gauss points and so on. However, GIMP has been limited to solving problems involving structured background meshes, while integrations on the Gauss points may bring in some intermediate mapping errors. Hence, using high-order elements or splines could be a future research topic, improving both the algorithmic accuracy and code robustness.

- The random MPM has been proposed in this thesis, which is able to assess the potential risks in terms of reliability as in RFEM, giving a more comprehensive estimate of the failure consequence (e.g. failure extent). However, analysing the whole failure process may result in a much longer CPU time compared to an RFEM analysis focusing only on the failure initiation. Hence, parallel computing techniques can be incorporated in the future to enable more realisations for the Monte-Carlo simulation, giving more robust solutions.

- A reduction of the uncertainties relating to soil property distributions is possible, by constraining the spatial variability using site specific data to condition the random fields. Results can be combined with RMPM analyses to provide more accurate and realisitic evaluations of slope system responses. Comparisons with real slope failures should also be undertaken in the future.

- Boundary condition treatment regarding the water phase could be useful in further research. For example, zero pore pressure prescribed boundary material points could change positions during successive retrogressive failures, for example in the long inclined slope collapse case, and could end up within the slope body. A better technique should be found to better interpret the boundary material points.

The rainfall infiltration boundary was simply represented by nulling pore pressures on the boundary material points in the current MPM formulation, without the capability of modelling the rainfall intensity and patterns. Velocity-based boundaries can be considered, and a better representation of the movement of the water phase should be taken into account as well.

- A simple frictional algorithm is provided in this thesis to model the contact inbetween the slope base and the fixed ground boundary. It can be extended to a more generalised contact, including both frictional and adhesive components, in which the boundary nodes can be detected automatically; hence, problems such as impact and penetrations can be better captured. Moreover, in cases of soil-fluid interactions, extra work may be needed to reduce the oscillations that exist at the soil-fuid interface.

- The heterogeneity of the soil undoubtedly has a significant influence on the slope failure initiation, as demonstrated by RFEM, and the failure consequence, as shown by RMPM. In reality, the spatial distribution of soil permeability could also lead to preferential flow paths within the soil when subjected to the rainfall flow, and hence influence the slope failure mechanism and modes. Random field theory could be combined with coupled MPM in future research, to investigate a wide range of slopes at risk of rainfall-induced failure.

- MPM codes may suffer excessive mesh dependency problems when strain-softening models are used, as has previously been found for FEM. Localisation of deformation has a detrimental effect on the integrity of the structure, and often acts as a direct precursor to structural failure. Hence, it is important to properly capture the localisation phenomenon in analysing structure (in)stabilities. The implementation of a suitable regularisation technique to address the issue, as is done in FEM, should be a subject of future research.

**6**

# REFERENCES

Abbo, A. and Sloan, S.: A smooth hyperbolic approximation to the Mohr-Coulomb yield criterion, Computers and Structures, 54, 427–441, 1995.

Abe, K., Soga, K., and Bandara, S.: Material point method for coupled hydromechanical problems, Journal of Geotechnical and Geoenvironmental Engineering, 140, 1–16, 2013.

Abed, A.: Numerical modeling of expansive soil behavior, Ph.D. thesis, Stuttgart University, 2008.

Al-Kafaji, I. K. J.: Formulation of a dynamic material point method (MPM) for geomechanical problems, Ph.D. thesis, Stuttgart University, 2013.

Andersen, S. and Andersen, L.: Analysis of stress updates in the material-point method, in: The Nordic Seminar on Computational Mechanics, pp. 129–134, 2009.

Andresen, L. and Jostad, H. P.: Analyses of progressive failure in long natural slopes, in: Numerical Models in Geomechanics – NUMOG IX, pp. 25–27, Ottawa, Canada, 2004.

Andresen, L. and Jostad, H. P.: Numerical modeling of failure mechanisms in sensitive soft clay - Application to offshore geohazards, in: Offshore Technology Conference, pp. 75–95, 2007.

Arnold, P. and Hicks, M. A.: A stochastic approach to rainfall-induced slope failure, in: Proceedings of 3rd international symposium of safety and risk, Munich, Germany, pp. 107–115, 2011.

Bandara, S. S.: Material point method to simulate large deformation problems in fluid-saturated granular medium, Ph.D. thesis, University of Cambridge, 2013.

Bandara, S. S. and Soga, K.: Coupling of soil deformation and pore fluid flow using material point method, Computers and Geotechnics, 63, 199–214, 2015.

Bardenhagen, S. and Kober, E.: The generalized interpolation material point method, Computer Modeling in Engineering and Sciences, 5, 477–496, 2004.

Bardenhagen, S., Guilkey, J. E., Roessig, K., Brackbill, J., Witzel, W., and Foster, J.: An improved contact algorithm for the material point method and application to stress propagation in granular material, Computer Modeling in Engineering and Sciences, 2, 509–522, 2001.

Bathe, K.-J.: Finite element procedures, Prentice Hall, New Jersey, 2nd edn., 1996.

Belytschko, T., Krongauz, Y., Organ, D., Fleming, M., and Krysl, P.: Meshless methods: An overview and recent developments, Computer Methods in Applied Mechanics and Engineering, 139(1-4), 3–47, 1996.

Benson, D. J.: An efficient, accurate, simple ALE method for nonlinear finite element programs, Computer Methods in Applied Mechanics and Engineering, 72, 305–350, 1989.

Bernander, S.: Progressive failure in long natural slopes: formation, potential extension and configuration of finished slides in strain-softening soils, Ph.D. thesis, Lulea university of Technology, 2000.

Beuth, L., Wieçkowski, Z., and Vermeer, P.: Solution of quasi-static large-strain problems by the material point method, International Journal for Numerical and Analytical Methods in Geomechanics, 35, 1451–1465, 2011.

Bishop, A. W.: The use of the slip circle in the stability analysis of slopes, Géotechnique, 5, 7–17, 1955.

Bjerrum, L.: Stability of natural slopes in quick clay, Géotechnique, 5, 101–119, 1955.

Brand, E.: Some thoughts on rain-induced slope failures, in: Proceedings of the 10th International Conference on Soil Mechanics and Foundation Engineering, Stockholm, Sweden, vol. 3, pp. 373–376, 1981.

Brunsden, D. and Jones, D.: Relative time scales and formative events in coastal landslide systems, Zeitschrift Geomorph NF Suppl, 34, 1–19, 1980.

Bui, H. H., Fukagawa, R., Sako, K., and Ohno, S.: Lagrangian meshfree particles method (SPH) for large deformation and failure flows of geomaterial using elastic–plastic soil constitutive model, International Journal for Numerical and Analytical Methods in Geomechanics, 32, 1537–1570, 2008.

Bui, H. H., Fukagawa, R., Sako, K., and Wells, J.: Slope stability analysis and discontinuous slope failure simulation by elasto-plastic smoothed particle hydrodynamics (SPH), Géotechnique, 61, 565–574, 2011.

Cai, F. and Ugai, K.: Numerical analysis of rainfall effects on slope stability, International Journal of Geomechanics, 4, 69–78, 2004.

Carson, M.: On the retrogression of landslides in sensitive muddy sediments, Canadian Geotechnical Journal, 14, 582–602, 1977.

Cascini, L., Cuomo, S., Pastor, M., and Sorbino, G.: Modeling of rainfall-induced shallow landslides of the flow-type, Journal of Geotechnical and Geoenvironmental Engineering, 136, 85–98, 2009.

Chen, R., Chen, H., Chen, K., and Zhung, H.: Simulation of a slope failure induced by rainfall infiltration, Environmental Geology, 58, 943–952, 2009.

Chen, Y. and Zhang, D.: Data assimilation for transient flow in geologic formations via ensemble Kalman filter, Advances in Water Resources, 29, 1107–1122, 2006.

Chen, Z. and Brannon, R.: An evaluation of the material point method, Report: SAND, 2002.

Cho, S. E.: Effects of spatial variability of soil properties on slope stability, Engineering Geology, 92, 97–109, 2007.

Cho, S. E.: Probabilistic assessment of slope stability that considers the spatial variability of soil properties, Journal of Geotechnical and Geoenvironmental Engineering, 136, 975–984, 2009.

Christian, J. T., Ladd, C. C., and Baecher, G. B.: Reliability applied to slope stability analysis, Journal of Geotechnical Engineering, 120, 2180–2207, 1994.

Clausen, J., Damkilde, L., and Andersen, L.: An efficient return algorithm for non-associated plasticity with linear yield criteria in principal stress space, Computers and Structures, 85, 1795–1807, 2007.

Coetzee, C., Vermeer, P., and Basson, A.: The modeling of anchors using the material point method, International Journal for Numerical and Analytical Methods in Geomechanics, 29, 879–895, 2005.

Cooley, J. W. and Tukey, J. W.: An algorithm for the machine calculation of complex Fourier series, Mathematics of Computation, 19, 297–301, 1965.

Cruden, D. M.: A simple definition of a landslide, Bulletin of Engineering Geology and the Environment, 43, 27–29, 1991.

Cruden, D. M. and Varnes, D. J.: Landslide types and processes, Special report 247, Washington DC: Transportation Research Board, National Research Council, 1958.

Cundall, P.: Distinct element models of rock and soil structure., In Analytical and Computational Methods in Engineering Rock Mechanics, pp. 129–163, 1987.

Dai, F. and Lee, C.: Frequency–volume relation and prediction of rainfall-induced landslides, Engineering Geology, 59, 253–266, 2001.

Demers, D., Robitaille, D., Locat, P., and Potvin, J.: Inventory of large landslides in sensitive clay in the province of Quebec, Canada: preliminary analysis, in: Landslides in Sensitive Clays, pp. 77–89, 2014.

Dey, R., Hawlader, B., Phillips, R., and Soga, K.: Progressive failure of slopes with sensitive clay layers, in: Proceedings of the 18th International Conference on Soil Mechanics and Geotechnical Engineering, Paris, France, pp. 2177–2180, 2013.

Dey, R., Hawlader, B., Phillips, R., and Soga, K.: Large deformation finite-element modelling of progressive failure leading to spread in sensitive clay slopes, Géotechnique, 65, 657–668, 2015.

Donea, J., Huerta, A., Ponthot, J.-P., and Rodríguez-Ferran, A.: Arbitrary Lagrangian-Eulerian methods, Encyclopedia of Computational Mechanics, 1, 413–437, 2004.

Duncan, J. M.: Factors of safety and reliability in geotechnical engineering, Journal of Geotechnical and Geoenvironmental Engineering, 126, 307–316, 2000.

El-Ramly, H., Morgenstern, N. R., and Cruden, D. M.: Probabilistic slope stability analysis for practice, Canadian Geotechnical Journal, 39, 665–683, 2002.

Fellenius, W.: Calculation of the stability of earth dams, in: Transactions of the 2nd Congress on Large Dams, Washington, DC, USA, vol. 4, pp. 445–463, 1936.

Fenton, G. A. and Griffiths, D.: Probabilistic foundation settlement on spatially random soil, Journal of Geotechnical and Geoenvironmental Engineering, 128, 381–390, 2002.

Fenton, G. A. and Griffiths, D.: Bearing-capacity prediction of spatially random c $\varphi$ soils, Canadian Geotechnical Journal, 40, 54–65, 2003.

Fenton, G. A. and Vanmarcke, E. H.: Simulation of random fields via local average subdivision, Journal of Engineering Mechanics, 116, 1733–1749, 1990.

Fern, E. J. and Soga, K.: The role of constitutive models in MPM simulations of granular column collapses, Acta Geotechnica, 11, 659–678, 2016.

Fortin, A., Ouellet, D., Paradis, S., and Demers, D.: Développement au Ministére des Transports du Québec d'un porail informatique pour l'accés á des bases de données géotechnique., in: Proceedings of the 4th Canadian conference on geohazards: from causes to management, Québec, Canada, pp. 169–174, Presses de l'Université Laval, Québec, Canada, 2008.

Fredlund, D. G. and Rahardjo, H.: Soil mechanics for unsaturated soils, John Wiley and Sons, New Jersey, 1993.

Gersch, W. and Yonemoto, J.: Parametric time series models for multivariate EEG analysis, Computers and Biomedical Research, 10, 113–125, 1977.

Ghosh, S. and Kikuchi, N.: An arbitrary Lagrangian-Eulerian finite element method for large deformation analysis of elastic-viscoplastic solids, Computer Methods in Applied Mechanics and Engineering, 86, 127–188, 1991.

Gibson, R. and Morgenstern, N.: A note on the stability of cuttings in normally consolidated clays, Géotechnique, 12, 212–216, 1962.

Gregersen, O.: The quick clay slide at Rissa, Norway, in: 10th International Conference on Soil Mechanics and Foundation Engineering, Stockholm, Sweden, vol. 3, pp. 421–426, 1981.

Griffiths, D. and Fenton, G. A.: Seepage beneath water retaining structures founded on spatially random soil, Géotechnique, 43, 577–587, 1993.

Griffiths, D. and Fenton, G. A.: Probabilistic slope stability analysis by finite elements, Journal of Geotechnical and Geoenvironmental Engineering, 130, 507–518, 2004.

Griffiths, D. and Lane, P.: Slope stability analysis by finite elements, Géotechnique, 49, 387–403, 1999.

Griffiths, D., Huang, J., and Fenton, G. A.: On the reliability of earth slopes in three dimensions, in: Proceedings of the Royal Society A Mathematical Physical and Engineering Sciences, vol. 465, pp. 3145–3164, The Royal Society, 2009.

Griffiths, D., Huang, J., and Fenton, G. A.: Probabilistic infinite slope analysis, Computers and Geotechnics, 38, 577–584, 2011.

Guilkey, J. E. and Weiss, J. A.: Implicit time integration for the material point method: Quantitative and algorithmic comparisons with the finite element method, International Journal for Numerical Methods in Engineering, 57, 1323–1338, 2003.

Guilkey, J. E., Hoying, J. B., and Weiss, J. A.: Computational modeling of multicellular constructs with the material point method, Journal of Biomechanics, 39, 2074–2086, 2006.

Hajiabdolmajid, V. and Kaiser, P.: Brittleness of rock and stability assessment in hard rock tunneling, Tunnelling and Underground Space Technology, 18, 35–48, 2003.

Harlow, F. H.: The particle-in-cell computing method for fluid dynamics, Methods of Computational Physics, 3, 319–343, 1964.

Henderson, T. C., McMurtry, P. A., Smith, P. J., Voth, G. A., Wight, C. A., and Pershing, D. W.: Simulating accidental fires and explosions, Computing in Science and Engineering, 2, 64–76, 2000.

Hendron, A. J. and Patton, F. D.: The Vaiont slide – a geotechnical analysis based on new geologic observations of the failure surface, Engineering Geology, 24, 475–491, 1987.

Hentz, S., Daudeville, L., and Donzé, F. V.: Identification and validation of a discrete element model for concrete, Journal of Engineering Mechanics, 130, 709–719, 2004.

Hicks, M. A. and Nuttall, J. D.: Influence of soil heterogeneity on geotechnical performance and uncertainty: A stochastic view on EC7, in: Proceedings of 10th International Probabilistic Workshop, Universität Stuttgart, Stuttgart, Germany, pp. 215–227, 2012.

Hicks, M. A. and Onisiphorou, C.: Stochastic evaluation of static liquefaction in a predominantly dilative sand fill, Géotechnique, 55, 123–133, 2005.

Hicks, M. A. and Samy, K.: Influence of heterogeneity on undrained clay slope stability, Quarterly Journal of Engineering Geology and Hydrogeology, 35, 41–49, 2002.

Hicks, M. A. and Spencer, W. A.: Influence of heterogeneity on the reliability and failure of a long 3D slope, Computers and Geotechnics, 37, 948–955, 2010.

Hicks, M. A., Chen, J., and Spencer, W. A.: Influence of spatial variability on 3D slope failures, in: 6th International Conference on Computer Simulation Risk Analysis and Hazard Mitigation, Crete, Greece, vol. 39, pp. 335–342, 2008.

Hicks, M. A., Nuttall, J. D., and Chen, J.: Influence of heterogeneity on 3D slope reliability and failure consequence, Computers and Geotechnics, 61, 198–208, 2014.

Hommels, A. and Molenkamp, F.: Inverse analysis of an embankment using the Ensemble Kalman filter including heterogeneity of the soft soil., in: 6th European Conference on Numerical Methods in Geotechnical Engineering, pp. 635–639, Graz, Austria, 2006.

Hu, W. and Chen, Z.: Model-based simulation of the synergistic effects of blast and fragmentation on a concrete wall using the MPM, International Journal of Impact Engineering, 32, 2066–2096, 2006.

Hungr, O.: Flow slides and flows in granular soils, in: Proceedings of the International Workshop Flows – Occurrence and Mechanisms of Flows in Natural Slopes and Earthfill, Sorrento, Italy, 2003.

Hungr, O., Leroueil, S., and Picarelli, L.: The Varnes classification of landslide types, an update, Landslides, 11, 167–194, 2014.

Idelsohn, S., Onate, E., Del Pin, F., and Calvo, N.: Fluid–structure interaction using the particle finite element method, Computer Methods in Applied Mechanics and Engineering, 195, 2100–2123, 2006.

Idelsohn, S. R., Oñate, E., and Pin, F. D.: The particle finite element method: a powerful tool to solve incompressible flows with free-surfaces and breaking waves, International Journal for Numerical Methods in Engineering, 61, 964–989, 2004.

Jassim, I., Stolle, D., and Vermeer, P.: Two-phase dynamic analysis by material point method, International Journal for Numerical and Analytical Methods in Geomechanics, 37, 2502–2522, 2013.

Jing, L.: A review of techniques, advances and outstanding issues in numerical modelling for rock mechanics and rock engineering, International Journal of Rock Mechanics and Mining Sciences, 40, 283–353, 2003.

Keaton, J., Wartman, J., Anderson, S., Benoît, J., deLaChapelle, J., Gilbert, R., and Montgomery, D.: The 22 March 2014 Oso Landslide, Snohomish County, Washington, GEER report, NSF Geotechnical Extreme Events Reconnaissance, 2014.

Kilburn, C. R. and Petley, D. N.: Forecasting giant, catastrophic slope collapse: lessons from Vajont, Northern Italy, Geomorphology, 54, 21–32, 2003.

Kumar, K., Soga, K., and Delenne, J.-Y.: Multi-scale modelling of granular avalanches, in: AIP Conference, vol. 1542, pp. 1250–1253, 2013.

Leroueil, S.: Natural slopes and cuts: movement and failure mechanisms, Géotechnique, 51, 197–243, 2001.

Lewis, R. W. and Schrefler, B. A.: The finite element method in the static and dynamic deformation and consolidation of porous media, 2nd Edition, John Wiley and Sons, Chichester, 1998.

Li, D., Qi, X., Phoon, K. K., Zhang, L., and Zhou, C.: Effect of spatially variable shear strength parameters with linearly increasing mean trend on reliability of infinite slopes, Structural Safety, 49, 45–55, 2014.

Li, K. S. and Lumb, P.: Probabilistic design of slopes, Canadian Geotechnical Journal, 24, 520–531, 1987.

Li, Y. and Hicks, M. A.: Comparative study of embankment reliability in three dimensions, in: 8th European Conference on Numerical Methods in Geotechnical Engineering, vol. 1, pp. 467–472, Delft, the Netherlands, 2014.

Li, Y., Hicks, M. A., and Nuttall, J. D.: Comparative analyses of slope reliability in 3D, Engineering Geology, 196, 12–23, 2015.

Liakopoulos, A. C.: Transient flow through unsaturated porous media, Ph.D. thesis, University of California, Berkeley, 1964.

Lim, L. J.: Pile penetration simulation with material point method, Master's thesis, Delft University of Technology, 2012.

Lim, L. J., Andreykiv, A., and Brinkgreve, R.: On the application of the material point method for offshore foundations, in: 8th European Conference on Numerical Methods in Geotechnical Engineering, vol. 1, pp. 253–258, Delft, the Netherlands, 2014.

Lin, C.-W., Liu, S.-H., Lee, S.-Y., and Liu, C.-C.: Impacts of the Chi-Chi earthquake on subsequent rainfall-induced landslides in central Taiwan, Engineering Geology, 86, 87–101, 2006.

Liu, W. K., Belytschko, T., and Chang, H.: An arbitrary lagrangian-eulerian finite element method for path-dependent materials, Computer Methods in Applied Mechanics and Engineering, 58, 227–245, 1986.

Llano-Serna, M. A., Farias, M. M., and Pedroso, D. M.: An assessment of the material point method for modelling large scale run-out processes in landslides, Landslides, doi:10.1007/s10346-015-0664-4, 2015.

Lloret-Cabot, M., Fenton, G. A., and Hicks, M. A.: On the estimation of scale of fluctuation in geostatistics, Georisk: Assessment and Management of Risk for Engineered Systems and Geohazards, 8, 129–140, 2014.

Locat, A., Leroueil, S., Bernander, S., Demers, D., Jostad, H. P., and Ouehb, L.: Progressive failures in eastern Canadian and Scandinavian sensitive clays, Canadian Geotechnical Journal, 48, 1696–1712, 2011.

Locat, A., Jostad, H. P., and Leroueil, S.: Numerical modeling of progressive failure and its implications for spreads in sensitive clays, Canadian Geotechnical Journal, 50, 961–978, 2013.

Lube, G., Huppert, H. E., Sparks, R. S. J., and Freundt, A.: Static and flowing regions in granular collapses down channels, Physics of Fluids, 19, 1601–1618, 2007.

Lucy, L. B.: A numerical approach to the testing of the fission hypothesis, The Astronomical Journal, 82, 1013–1024, 1977.

Lumb, P.: The variability of natural soils, Canadian Geotechnical Journal, 3, 74–97, 1966.

Ma, J., Lu, H., and Komanduri, R.: Structured mesh refinement in generalized interpolation material point (GIMP) method for simulation of dynamic problems, Computer Modeling in Engineering and Sciences, 12, 213 – 227, 2006.

Mast, C. M.: Modeling landslide-induced flow interactions with structures using the material point method, Ph.D. thesis, University of Washington, 2013.

Matheron, G.: The intrinsic random functions and their applications, Advances in Applied Probability, pp. 439–468, 1973.

McDougall, S. and Hungr, O.: A model for the analysis of rapid landslide motion across three-dimensional terrain, Canadian Geotechnical Journal, 41, 1084–1097, 2004.

Mitchell, R. and Klugman, M.: Mass instabilities in sensitive Canadian soils, Engineering Geology, 14, 109–134, 1979.

Müller-Salzburg, L.: The rock slide in the Vajont Valley, Engineering Geology and Rock Mechanics, 2, 148–212, 1964.

Nairn, J.: Material point method calculations with explicit cracks, Computer Modeling in Engineering and Sciences, 4, 649–664, 2003.

Nayak, G. and Zienkiewicz, O.: Convenient form of stress invariants for plasticity, J. Struct. Div. ASCE, 4, 949–953, 1972.

Nazem, M., Sheng, D., Carter, J. P., and Sloan, S. W.: Arbitrary Lagrangian–Eulerian method for large-strain consolidation problems, International Journal for Numerical and Analytical Methods in Geomechanics, 32, 1023–1050, 2008.

Nazem, M., Carter, J. P., and Airey, D. W.: Arbitrary Lagrangian–Eulerian method for dynamic analysis of geotechnical problems, Computers and Geotechnics, 36, 549–557, 2009.

Newmark, N. M.: A method of computation for structural dynamics, Journal of Engineering Mechanics Division ASCE, 85, 67–94, 1959.

Ng, C. W., Wang, B., and Tung, Y.: Three-dimensional numerical investigations of groundwater responses in an unsaturated slope subjected to various rainfall patterns, Canadian Geotechnical Journal, 38, 1049–1062, 2001.

Odenstad, S.: The Landslide at Skottorp on the Lidan river: Febr. 2., 1946, in: Royal Swedish Institute Proceedings, vol. 4, pp. 1–38, 1951.

Oñate, E., Idelsohn, S. R., Del Pin, F., and Aubry, R.: The particle finite element method - an overview, International Journal of Computational Methods, 1, 267–307, 2004.

Paice, G., Griffiths, D., and Fenton, G. A.: Finite element modeling of settlements on spatially random soil, Journal of Geotechnical Engineering, 122, 777–779, 1996.

Pastor, M., Merodo, J. F., Gonzalez, E., Mira, P., Li, T., and Liu, X.: Modelling of landslides:(I) Failure mechanisms, Springer, 2004.

Pastor, M., Haddad, B., Sorbino, G., Cuomo, S., and Drempetic, V.: A depth-integrated, coupled SPH model for flow-like landslides and related phenomena, International Journal for Numerical and Analytical Methods in Geomechanics, 33, 143–172, 2009.

Pastor, M., Blanc, T., Haddad, B., Petrone, S., Morles, M. S., Drempetic, V., Issler, D., Crosta, G., Cascini, L., Sorbino, G., et al.: Application of a SPH depth-integrated model to landslide run-out analysis, Landslides, 11, 793–812, 2014.

Phuong, N., van Tol, A., Elkadi, A., and Rohe, A.: Modelling of pile installation using the material point method (MPM), in: 8th European Conference on Numerical Methods in Geotechnical Engineering, vol. 1, pp. 271–276, 2014.

Pradel, D. and Raad, G.: Effect of permeability on surficial stability of homogeneous slopes, Journal of Geotechnical Engineering, 119, 315–332, 1993.

Qiu, G., Henke, S., and Grabe, J.: Application of a coupled Eulerian-Lagrangian approach on geomechanical problems involving large deformations, Computers and Geotechnics, 38, 30–39, 2011.

Quinn, P., Diederichs, M., Hutchinson, D. J., and Rowe, R. K.: An exploration of the mechanics of retrogressive landslides in sensitive clay, in: Proceedings of the 60th Canadian Geotechnical Conference and 8th Joint CGS/IAH-CNC Groundwater Conference, Ottawa, Canada, pp. 21–24, 2007.

Rahardjo, H., Li, X., Toll, D. G., and Leong, E. C.: The effect of antecedent rainfall on slope stability, Geotechnical and Geological Engineering, 19, 371–399, 2001.

Rahardjo, H., Ong, T., Rezaur, R., and Leong, E. C.: Factors controlling instability of homogeneous soil slopes under rainfall, Journal of Geotechnical and Geoenvironmental Engineering, 133, 1532–1543, 2007.

Rodriguez-Paz, M. and Bonet, J.: A corrected smooth particle hydrodynamics formulation of the shallow-water equations, Computers and Structures, 83, 1396–1410, 2005.

Sadeghirad, A., Brannon, R. M., and Burghardt, J.: A convected particle domain interpolation technique to extend applicability of the material point method for problems involving massive deformations, International Journal for Numerical Methods in Engineering, 86, 1435–1456, 2011.

Samy, K.: Stochastic analysis with finite elements in geotechnical engineering, Ph.D. thesis, University of Manchester, 2003.

Shin, W. K.: Numerical simulation of landslides and debris flows using an enhanced material point method, Ph.D. thesis, University of Washington, 2009.

Sloan, S. W., Abbo, A. J., and Sheng, D.: Refined explicit integration of elastoplastic models with automatic error control, Engineering Computations, 18, 121–194, 2001.

Sloan, S. W., Abbo, A. J., and Sheng, D.: Erratum, Engineering Computations, 19, 594, 2002.

Sluys, L. J., Muhlhaus, H. B., Borst, R. D., and Pamin, J.: Fundamental issues in finite element analyses of localization of deformation, Engineering Computations, 10, 99–121, 1993.

Smith, I. M. and Griffiths, D. V.: Programming the finite element method, John Wiley and Sons, Chichester, 4th edn., 2005.

Soga, K., Alonso, E., Yerro, A., Kumar, K., and Bandara, S.: Trends in large-deformation analysis of landslide mass movements with particular emphasis on the material point method, Géotechnique, pp. 1–26, 2015.

Sokolovskii, V. V.: Statics of granular media, Journal of Applied Mechanics, 33, 239–247, 1966.

Sołowski, W. and Sloan, S.: Modelling of sand column collapse with material point method, in: Proceedings of the 3rd International Symposium on Computational Geomechanics, pp. 698–705, 2013.

Spencer, W. A.: Parallel stochastic and finite element modelling of clay slope stability in 3D, Ph.D. thesis, University of Manchester, 2007.

Steffen, M., Wallstedt, P., Guilkey, J., Kirby, R., and Berzins, M.: Examination and analysis of implementation choices within the material point method (MPM), Computer Modeling in Engineering and Sciences, 31, 107–127, 2008.

Stomakhin, A., Schroeder, C., Chai, L., Teran, J., and Selle, A.: A material point method for snow simulation, ACM Transactions on Graphics (TOG), 32, 102, 2013.

Sulsky, D. and Kaul, A.: Implicit dynamics in the material-point method, Computer Methods in Applied Mechanics and Engineering, 193, 1137–1170, 2004.

Sulsky, D., Chen, Z., and Schreyer, H. L.: A particle method for history-dependent materials, Computer Methods in Applied Mechanics and Engineering, 118, 179–196, 1994.

Sulsky, D., Zhou, S., and Schreyer, H. L.: Application of a particle-in-cell method to solid mechanics, Computer Physics Communications, 87, 236–252, 1995.

Terzaghi, K.: Theoretical soil mechanics, John Wiley and Sons, New Jersey, 1943.

Tho, K., Leung, C., Chow, Y., and Swaddiwudhipong, S.: Eulerian finite-element technique for analysis of jack-up spudcan penetration, International Journal of Geomechanics, 12, 64–73, 2012.

Thomson, S. and Hayley, D. W.: The Little Smoky Landslide, Canadian Geotechnical Journal, 12, 379–392, 1975.

Tsaparas, I., Rahardjo, H., Toll, D. G., and Leong, E. C.: Controlling parameters for rainfall-induced landslides, Computers and Geotechnics, 29, 1–27, 2002.

Van Asch, T., Brinkhorst, W., Buist, H., and Vessem, P.: The development of landslides by retrogressive failure in varved clays, Zeitschrift fur Geomorphologie NF, 4, 165–181, 1984.

Van Esch, J., Stolle, D., and Jassim, I.: Finite element method for coupled dynamic flow-deformation simulation, in: Proceedings of the 2nd International Symposium on Computational Geomechanics, 2011.

Van Genuchten, M. T.: A closed-form equation for predicting the hydraulic conductivity of unsaturated soils, Soil Science Society of America Journal, 44, 892–898, 1980.

Vanmarcke, E. H.: Probabilistic modelling of soil profiles, Journal of the Geotechnical Engineering Division ASCE, 103, 1227–1246, 1977a.

Vanmarcke, E. H.: Reliability of earth slopes, Journal of the Geotechnical Engineering Division ASCE, 103, 1247–1265, 1977b.

Vanmarcke, E. H.: Random fields: analysis and synthesis, World Scientific, 2010.

Vardon, P. J., Liu, K., and Hicks, M. A.: Reduction of slope stability uncertainty based on hydraulic measurement via inverse analysis, Georisk Assessment and Management of Risk for Engineered Systems and Geohazards, doi:10.1080/17499518.2016.1180400, 2016.

Varnes, D. J.: Slope movement types and processes, special report 176, Washington DC: Transportation Research Board, National Academy of Sciences, 1978.

Verruijt, A.: An introduction to soil dynamics, Springer Science and Business Media, 2009.

Wang, B., Vardon, P. J., and Hicks, M. A.: Implementation of a quasi-static material point method for geotechnical applications, in: Proceedings of the 3rd International Symposium on Computational Geomechanics, pp. 305–313, Krakow, Poland, 2013.

Wang, B., Vardon, P. J., and Hicks, M. A.: Investigation of aspects of an implicit dynamic material point method implementation, in: 8th European Conference on Numerical Methods in Geotechnical Engineering, vol. 1, pp. 313–318, Delft, the Netherlands, 2014.

Wang, B., Hicks, M. A., and Vardon, P. J.: Slope stability analyses using the random material point method, Géotechnique letters, 6, 113–118, 2016a.

Wang, B., Vardon, P. J., and Hicks, M. A.: Investigation of retrogressive and progressive slope failure mechanismsusing the material point method, Computers and Geotechnics, 78, 88–98, 2016b.

Wang, B., Vardon, P. J., Hicks, M. A., and Chen, Z.: Development of an implicit material point method for geotechnical applications, Computers and Geotechnics, 71, 159–167, 2016c.

Wang, F. W., Zhang, Y. M., Huo, Z. T., Matsumoto, T., and Huang, B. L.: The July 14, 2003 Qianjiangping landslide, Three Gorges Reservoir, China, Landslides, 1, 157–162, 2004.

Wang, Y. and Tonon, F.: Modeling Lac du Bonnet granite using a discrete element model, International Journal of Rock Mechanics and Mining Sciences, 46, 1124–1135, 2009.

Więckowski, Z.: The material point method in large strain engineering problems, Computer Methods in Applied Mechanics and Engineering, 193, 4417–4438, 2004.

Więckowski, Z., Youn, S.-K., and Yeon, J.-H.: A particle-in-cell solution to the silo discharging problem, International journal for numerical methods in engineering, 45, 1203–1225, 1999.

Wong, S. Y.: Stochastic characterisation and reliability of saturated soils, Ph.D. thesis, University of Manchester, 2004.

Xu, L., Dai, F., Chen, J., Iqbal, J., and Qu, Y.: Analysis of a progressive slope failure in the Xiangjiaba reservoir area, Southwest China, Landslides, 11, 55–66, 2014.

Xue, J. and Gavin, K.: Effect of rainfall intensity on infiltration into partly saturated slopes, Geotechnical and Geological Engineering, 26, 199–209, 2008.

Yap, T. Y. and Hicks, M. A.: An investigation of element-size-dependency in strain localization, in: Proceedings of the 10th International Conference on Computer Methods and Advances in Geomechanics, pp. 153–159, Tucson, USA., 2001.

Yerro, A.: Solving hydro-mechanical problems with the material point method, in: Proceedings of the 21st European Young Geotechnical Engineers Conference Geotechnical Engineering: New Horizons, pp. 318–323, Rotterdam, the Netherlands, 2011.

Yerro, A.: MPM modelling of landslides in brittle and unsaturated soils, Ph.D. thesis, Universitat Politècnica de Catalunya, 2015.

Yerro, A., Alonso, E. E., and Pinyol, N. M.: The material point method for unsaturated soils, Géotechnique, 65(3), 201–217, 2015.

Zabala, F. and Alonso, E. E.: Progressive failure of Aznalcollar dam using the material point method, Géotechnique, 61, 795–808, 2011.

Zhang, H., Wang, K., and Zhang, Z.: Material point method for numerical simulation of failure phenomena in multiphase porous media, in: International Symposium on Computational Mechanics, Beijing, China, pp. 36–47, 2007.

Zhang, H., Wang, K., and Chen, Z.: Material point method for dynamic analysis of saturated porous media under external contact/impact of solid bodies, Computer Methods in Applied Mechanics and Engineering, 198, 1456–1472, 2009.

Zhang, X., Krabbenhoft, K., Sheng, D., and Li, W.: Numerical simulation of a flow-like landslide using the particle finite element method, Computational Mechanics, 55, 167–177, 2015.

Zhang, Z. and Chen, Q.: Comparison of the Eulerian and Lagrangian methods for predicting particle transport in enclosed spaces, Atmospheric Environment, 41, 5236–5248, 2007.

Zhu, H., Zhang, L., Zhang, L., and Zhou, C.: Two-dimensional probabilistic infiltration analysis with a spatially varying permeability function, Computers and Geotechnics, 48, 249–259, 2013.

Zienkiewicz, O., Chang, C., and Bettess, P.: Drained, undrained, consolidating and dynamic behaviour assumptions in soils, Géotechnique, 30, 385–395, 1980.

# NOTATION

## Acronyms

ALE     arbitrary Lagrangian-Eulerian

CEL     coupled Eulerian-Lagrangian

CFL     Courant-Friedrichs-Lewy

CG     conjugate gradient

CMPM   coupled material point method

CPDI    convected particle domain interpolation

CPT     cone penetration test

DEM    discrete element method

EVF     Eulerian volume fraction

FEM    finite element method

FFT     fast Fourier transform

FOS     factor of safety

FOSM   first order second moment

FSI     fluid-solid interaction

FVM    finite volume method

GIMP    generalized interpolation material point

IMPM   implicit material point method

LAS     local average subdivision

LEM    limit equilibrium method

MA     moving average

MPM    material point method

PFEM    particle finite element method

PIC     particle-in-cell

pdf       probability density function

RFEM   random finite element method

RMPM   random material point method

SPH      smoothed particle hydrodynamics

SWRC   soil water retention curve

TBM      turning bands method

UL        updated Lagrangian

UL-FEM   updated Lagrangian finite element method

USF      update stress first

USL      update stress last

## Latin Symbols

$A$        hardening modulus (Chapter 3); averaging area (Chapter 4)

$A_1$       intermediate modulus in modified Mohr-Coulomb function

$a$        smoothing parameter in modified Mohr-Coulomb function

$\mathbf{a}$        acceleration

$\mathbf{a}_s$       acceleration of solid skeleton

$\mathbf{a}_w$       acceleration of water

$B_1$       intermediate modulus in modified Mohr-Coulomb function

$\mathbf{b}$        body force

$\mathbf{B}_L$       linear strain–displacement transformation matrix

$\mathbf{B}_{NL}$     nonlinear strain–displacement transformation matrix

$c$        cohesion

$c_d$       damping factor

$c_i$       initial cohesion

$c_p$       peak cohesion

$c_r$       residual cohesion

$c_u$       undrained shear strength

| | |
|---|---|
| $c_v$ | wave speed |
| $c_w$ | consolidation coefficient |
| $\mathbf{c}^s$ | traction vector |
| $\mathbf{D}^e$ | elastic stress-strain matrix |
| $\mathbf{D}^{ep}$ | elasto-plastic stress-strain matrix |
| $E$ | Young's modulus |
| $E_{kin}$ | kinetic energy |
| $E_{strain}$ | strain energy |
| $F$ | yield function |
| $\mathbf{F}_{damp}$ | damping force |
| $\mathbf{F}_{drag,w}$ | drag force due to the soil-water interaction |
| $\mathbf{F}_{ext}$ | external force |
| $\bar{\mathbf{F}}_{ext}$ | modified external force |
| $\mathbf{F}_{grav}$ | gravity force |
| $\mathbf{F}_{grav,w}$ | water gravity force |
| $\mathbf{F}_i$ | resultant nodal force |
| $\mathbf{F}_{int}$ | internal force |
| $\mathbf{F}_{int,w}$ | water internal force |
| $\mathbf{F}_{react}$ | reaction force |
| $\mathbf{F}_{trac}$ | traction force |
| $\mathbf{F}_{trac,w}$ | traction water force |
| $\mathbf{g}$ | gravitational acceleration vector |
| $H$ | hardening/softening modulus |
| $h$ | thickness of the boundary layer |
| $h_v$ | thickness of the soil layer in the consolidation test |
| $i$ | node numbering |
| $J$ | determinant of Jacobian matrix |
| $J_3$ | the third stress invariant |

| | |
|---|---|
| $K$ | hydraulic conductivity |
| $K_w$ | bulk modulus of water |
| $k$ | soil permeability |
| $k_{rel}$ | relative permeability |
| $k_{sat}$ | permeability at full saturation |
| $k_\theta$ | smoothing parameter in modified Mohr-Coulomb function |
| $\mathbf{K}$ | stiffness matrix |
| $\bar{\mathbf{K}}$ | modified stiffness matrix in the final governing equation of the implicit material point method |
| $\mathbf{K}_L$ | linear terms of the stiffness matrix |
| $\mathbf{K}_{NL}$ | nonlinear terms of the stiffness matrix |
| $L$ | length of bar |
| $m_w$ | fluid mass |
| $\bar{m}_w$ | fluid mass in a material point per unit of volumetric fraction |
| $m_s$ | solid mass |
| $\mathbf{M}$ | mass matrix |
| $\mathbf{M}_w$ | fluid mass matrix |
| $\bar{\mathbf{M}}_w$ | fluid mass matrix fraction |
| $\mathbf{M}_s$ | solid mass matrix |
| $\mathbf{m}$ | nodal mass matrix of size dimension × dimension |
| $\mathbf{m}_k$ | Kronecker delta vector $[1\ 1\ 0\ 1]^{\mathrm{T}}$ |
| $N_{blp}$ | number of material points within the vicinity of the boundary |
| $N_{\dim}$ | number of dimensions for the problem considered |
| $N_n$ | number of grid nodes around a material point |
| $N_p$ | number of material points |
| $n$ | porosity |
| $n_0$ | initial solid porosity |
| $n_e$ | number of nodes per element |

$n_s$      fitting parameters in SWRC curve

**N**      shape function

**n**      normal vector

$p$      material point numbering

$p_w$      water pressure

$\bar{\mathbf{p}}_w$      prescribed boundary pore pressures

$\mathbf{p}_w$      prescribed boundary pore pressures

**Q**      water dragging matrix

$Q$      plastic potential function

$\mathbf{R}_{ext}$      virtual external work

$r$      sliding distance

$S^c$      traction boundary

$S_e$      effective degree of saturation

$S_w$      degree of saturation

$S_{res}$      residual degree of saturation

$S_{sat}$      full degree of saturation

$s$      suction

**S**      second Piola-Kirchhoff stress

**s**      deviator stress tensor

$T_1$, $T_2$      finite domain length

$T_v$      time factor in the consolidation test

$t$      time

$t_1$, $t_2$      point at the end of sampling length $T$

$u$      standardized random variable

**u**      displacement

$\bar{\mathbf{u}}$      incremental displacement

$V$      coefficient of variation

$V_p$      material point domain

| | |
|---|---|
| $\mathbf{v}$ | velocity |
| $\bar{\mathbf{v}}$ | velocity used to update the displacement in explicit MPM formulation |
| $\mathbf{v}_s$ | velocity of the solid skeleton |
| $\mathbf{v}_w$ | velocity of liquid |
| $W^{ext}$ | external work |
| $\mathbf{w}^h$ | test function |
| $X$ | spatially varying property |
| $x$ | Cartesian coordinate |
| $\mathbf{x}$ | location |
| $y$ | Cartesian coordinate |
| $Z$ | local average for a random field cell |
| $z$ | Cartesian coordinate |
| $z_d$ | depth |

## Greek Symbols

| | |
|---|---|
| $\alpha$ | time stepping parameter used in the Newmark time integration |
| $\alpha_1, \alpha_2$ | fitting parameters to consider the depth-dependent trends in the point statistics |
| $\alpha_s$ | fitting parameters in SWRC curve |
| $\beta_1$ | eigenvalue |
| $\Gamma$ | boundary of the domain |
| $\gamma$ | variance function |
| $\gamma_z$ | self weight |
| $\Delta\mathbf{e}$ | linear part of the incremental strain |
| $\Delta\boldsymbol{\eta}$ | high-order terms of the incremental strain |
| $\Delta\boldsymbol{\omega}$ | spin tensor increment |
| $\delta$ | time stepping parameter used in the Newmark time integration |
| $\delta_1$ | force ratio |
| $\delta_2$ | energy ratio |

| | |
|---|---|
| $\boldsymbol{\epsilon}$ | Green-Lagrange strain tensor |
| $\boldsymbol{\varepsilon}^p$ | plastic strain |
| $\bar{\boldsymbol{\varepsilon}}^p$ | plastic shear strain invariant |
| $\bar{\varepsilon}_{pr}$ | plastic shear strain invariant at the onset of residual strength |
| $\eta$ | ratio of residual strength over peak strength |
| $\theta$ | Lode angle |
| $\theta_h$ | horizontal scale of fluctuation |
| $\theta_T$ | transition angle |
| $\theta_v$ | vertical scale of fluctuation |
| $\kappa$ | internal hardening/softening parameter |
| $\lambda$ | magnitude of plastic strain |
| $\mu$ | mean |
| $\mu_f$ | friction coefficient |
| $\mu_w$ | water viscosity |
| $\upsilon$ | Poisson's ratio |
| $\xi$ | anisotropy of heterogeneity |
| $\rho$ | mass density; correlation function (Chapter 4) |
| $\rho_s$ | density of solid grains |
| $\rho_w$ | liquid density |
| $\sigma$ | standard deviation |
| $\bar{\sigma}$ | square root of second stress invariant |
| $\sigma_m$ | mean stress |
| $\boldsymbol{\sigma}$ | total(Cauchy) stress tensor |
| $\hat{\boldsymbol{\sigma}}$ | Cauchy stress matrix |
| $\tilde{\boldsymbol{\sigma}}$ | Jaumann stress matrix |
| $\boldsymbol{\sigma}^J$ | Jaumann stress tensor |
| $\boldsymbol{\sigma'}_s$ | (Bishop) effective stress tensor |
| $\tau_1, \tau_2$ | lag distance |

| | |
|---|---|
| $\tau$ | shear stress component |
| $\boldsymbol{\tau}$ | prescribed boundary stress |
| $\phi$ | friction angle |
| $\boldsymbol{\varphi}_i$ | weighting function |
| $\Omega_p$ | material point volume |
| $\chi$ | matric suction coefficient |
| $\chi_p$ | characteristic function |
| $\psi$ | dilation angle |
| $\Omega$ | configuration of the continuum |
| $\Omega_e$ | element domain |
| $\Omega_\chi$ | integral domain of the characteristic function |
| $\omega_1$ | frequency of oscillation |
| $\boldsymbol{\omega}$ | test function |
| $\boldsymbol{\nabla}$ | vector differential operator |
| $\partial F/\partial\boldsymbol{\sigma}$ | vector normal to the yield surface |
| $\partial Q/\partial\boldsymbol{\sigma}$ | vector normal to the plastic potential surface |

# SUMMARY

Slope failure is a typical geotechnical problem, receiving substantial attention due to its potential to cause catastrophic damage. A complete description of slope failure should not be limited to only the description of the failure initiation, but should also include the slope failure propagation and final configuration. Such analyses can be considered particularly useful, as they contribute to the assessment of landslide volumes and their potential for traveling long distances. The widely-used finite element method (FEM) suffers from the disadvantage of mesh distortion during the initial stages of slope failure, which often results in analyses not being able to complete further steps. In contrast, the material point method (MPM) has been shown to be able to reliably capture large deformations, and is now being applied in the geotechnical field. Indeed, since its adaptation to solid mechanics in 1994, increasing attention has been given to it for a wide range of applications, including wave attacks on sea dykes, the progressive failure of river levees, and so on.

In this thesis, MPM has been further developed and implemented for applications to slope failure under different scenarios, and a number of the challenges associated with the simulation of observed slope failures have been tackled. These challenges include: (i) soil behaviour, including a material model that allows for the softening behaviour often observed post-failure, (ii) soil variability, (iii) unsaturated soil conditions and rainfall induced changes, and (iv) the very small timestep associated with explicit numerical methods, often used elsewhere in MPM. A series of simple slope simulations are presented, demonstrating the ability of the developed methods to simulate observed failure modes, from progressive failures to retrogressive failures and superficial failures.

The implicit material point method (IMPM) has been developed and implemented with the aim to provide an efficient computational procedure and to increase algorithmic accuracy. The alternative method, the explicit time integration scheme more often used in other MPM implementations, reduces the critical time step size required for the numerical stability of the analysis, and may make the computational effort prohibitive. Moreover, for problems involving plastic straining, in each loading/time step the displacement increment is not strictly determined for a fixed load increment by using an explicit time integration scheme. Hence, errors may accumulate over time.

Failure development and propagation in slopes require a representation of post-failure material behaviour, as well as a numerical method to simulate the large deformations. A simple strain softening material model has been implemented here to represent post-failure material behaviour. A series of slope failure simulations have shown that the method can simulate the range of post-failure modes observed in practice, such as retrogressive and progressive slope failures.

Spatial variation (i.e. heterogeneity) in soil properties exist, due to the geological, environmental, and physio-chemical processes during soil deposition. Accounting for the natural variability of soils, via the use of random fields of material properties, the

149

random material point method (RMPM) has been proposed in the thesis, which combines random field theory with MPM. In contrast to the random finite element method (RFEM), cell values from random fields are assigned to material points directly, rather than to the Gauss points of a finite element mesh. Multiple random field realisations can then be obtained and Monte Carlo simulations, involving multiple MPM analyses, can be performed in order to obtain a distribution of possible responses. The risks posed by potential slides have been quantified by the extent of retrogressive failure; i.e. due to the tendency for secondary failures to be triggered by the removal of support from the remaining soil mass caused by the initial failure. The results show that RMPM provides a much wider range of possible solutions, compared to RFEM in which solutions are limited to the initial slide. The importance of considering the effects of both large deformations and the spatial variability of soil strength properties in slope stability analyses has been highlighted.

Soil is a two phase material, and its behaviour is governed by the interaction between the solid and water phases. Changes in the water content of the soil have an important impact on the slope failure process of an unsaturated soil, by increasing the soil unit weight and reducing the soil effective stresses. A one-point, two-phase coupled material point method (coupled MPM) has been proposed to consider the influence of water on the slope failure process. Rainfall-induced slope failures are thereby considered and shown to be formed by a series of more superficial failures as are often observed in practice.

Through the developments and analyses presented in this thesis, it is shown that the majority of observed slope failures can be simulated, from spreads, to progressive and retrogressive failures, to earthflows. The ability to simulate the failure progression, from initiation through to final position, can allow a better assessment of the hazard posed by natural and man-made slopes.

# SAMENVATTING

Het bezwijken van een talud is een geotechnisch fenomeen bij uitstek, dat vanwege zijn potentieel catastrofale gevolgen veel aandacht krijgt. Een volledige analyse van het bezwijken van een talud zou niet beperkt moeten blijven tot het eerste moment van bezwijken, maar zou ook de verdere ontwikkeling van het bezwijkproces moeten omvatten. Een dergelijke analyse kan extra waardevol zijn wanneer toegepastinde analyse van bezwijkingsvolumes en bijbehorend verplaatsingsbereik. De veelgebruikte eindige elementen methode (FEM) heeft slechts beperkte toepasbaarheid en grote vervormingen leiden vaak tot verwrongen elementen, wat verdere analyse onmogelijk maakt. De material point method (MPM) daarentegen heeft bewezen grote vervormingen op betrouwbare manier te kunnen beschrijven en wordt nu gebruikt in de geotechniek. Sinds de introductie in de vaste stof mechanica in 1994 geniet deze methode meer en meer aandacht vanwege zijn brede toepasbaarheid, onder meer op het gebied van golfslag op zeeweringen en voortschrijdend bezwijken van rivieroevers.

In deze dissertatie is MPM verder ontwikkeld en geïmplementeerd voor toepassing op taludbezwijking onder verschillende scenario's en een aantal problemen rond het simuleren van waargenomen talud bezwijking zijn opgelost. Deze problemen omvatten: (i) grondgedrag, waaronder een materiaalmodel voorsofteninggedrag zoals vaak voorkomt na bezwijken, (ii) variabiliteit van de grond, (iii) onverzadigde condities en veranderingen daarin als gevolg van regenval en (iv) de zeer kleine tijdstap gerelateerd aan de expliciete formulering van de numerieke methodes, zoals vaak elders gebruikt voor MPM. Het vermogen van de ontwikkelde methode tot het simuleren van waargenomen bezwijkingsmechanismen, van progressieve bezwijking tot retrogressieve bezwijking en ondiepe bezwijking, wordt gedemonstreerd aan de hand van een reeks eenvoudige simulaties van taluds.

De impliciete material point method (IMPM) is ontwikkeld en geïmplementeerd met het doel een rekenkundigefficiëntemethode op te leveren en algoritmische nauwkeurigheid te vergroten. De expliciete tijdsintegratie als alternatieve methode, zoals gewoonlijk gebruikt wordt in MPM, verkleint de kritieke grootte van de tijdstap die nodig is om numerieke stabiliteit te garanderen en kan leiden tot onhaalbaar grote rekenbelasting. Daarbij komt nog dat in het geval van plastische vervorming, wanneer expliciete integratie over de tijd wordt gebruikt, een toename in verplaatsingmogelijk niet-deterministisch is voor een gegeven toename in belasting. Als gevolg kunnen onnauwkeurigheden opbouwen over de tijd.

De totstandkoming en ontwikkeling van bezwijkingsmechanismen in taluds vereist een beschrijving van post-bezwijkingsgedrag van het materiaal alsmede een numerieke methode die in staat is grote vervormingen in rekening te brengen. Een eenvoudig materiaalmodel voor softening is geïmplementeerd om post-bezwijkingsgedrag van het materiaal te beschrijven. Een reeks simulaties van taludbezwijking hebben aangetoond dat

de methode in staat is een scala aan post-bezwijkingsgedrag te simuleren, zoals waarge-
nomen kan worden in de praktijk, waaronder retrogressieve en progressieve bezwijking.

Grondeigenschappen kunnen ruimtelijke variaties (heterogeniteit) tonen als gevolg
van geologische, milieukundige of fysisch-chemische processen gedurende de afzetting.
Voor het in rekening brengen van natuurlijke variabiliteit van grond door middel van ase-
lecte weergave van ruimtelijke variaties in grondeigenschappen is de random material
point method (RMPM) geïntroduceerd in deze dissertatie. Deze methode combineert
theorie van aselecte velden met MPM. In tegenstelling tot de random eindige elementen
methode(RFEM) worden cel waarden van aselecte velden hier direct aan materiaal pun-
ten toegeschreven en niet aan Gauss punten zoals in FEM. Zo kunnen meerdere aselecte
velden gerealiseerd worden en Monte Carlo simulaties, met meerdere MPM analyses,
kunnen worden gemaakt teneinde een verdeling van mogelijk gedrag te genereren. De
risico's die voortkomen uit mogelijke afschuivingen zijn gekwantificeerd aan de hand
van het bereik van retrogressieve bezwijking, vanwege de neiging naar secundaire be-
zwijkingen als gevolg van het wegvallen van de ondersteuning van de massa van de ini-
tiële afschuiving . De resultaten tonen aan dat RMPM een veel breder bereik aan moge-
lijke uitkomsten heeft in vergelijking met RFEM, waarin uitkomsten beperkt blijven tot
de initiële afschuiving. Het belang van het in acht nemen van zowel grote vervormin-
gen en ruimtelijke variabiliteit van de sterkteparameters in analyses van taludstabiliteit
wordt hiermee onderstreept.

Grond bestaat uit twee fasen en grondgedrag wordt bepaald door de interactie tussen
de vaste fase en de waterfase. Veranderingen in het watergehalte van de grond hebben
een grote invloed op het bezwijkingsproces van een talud bestaand uit onverzadigde
grond, door het verhogen van de dichtheid en het verlagen van de effectieve spanning.
Een enkel-punts, twee-fasen, gekoppelde material point method (coupled MPM) is ge-
formuleerd om de invloed van water op het bezwijkingsproces in rekening te kunnen
brengen. Hiermee wordt taludbezwijking als gevolg van neerslag bestudeerd. Totale be-
zwijking wordt hier gedemonstreerd te ontstaan als gevolg van een reeks meer opper-
vlakkige bezwijking, zoals vaak waargenomen wordt in de praktijk.

Aan de hand van de ontwikkelingen en analyses in deze dissertatie is inzichtelijk ge-
maakt dat de meerderheid van waargenomen bezwijkingsmechanismen kunnen wor-
den gesimuleerd, zowel met betrekking op bereik als mechanismen van progressieve
tot retrogressieve bezwijking. Het vermogen de ontwikkeling van bezwijking te kunnen
modelleren, van initiatie tot de uiteindelijke evenwichtssituatie, kan een betere beoor-
deling mogelijk maken van het gevaar dat uit gaat van natuurlijke- en door de mens ge-
maakte taluds.

# ACKNOWLEDGMENTS

I would like to first express my sincere gratitude to Prof. dr. Michael Hicks for his supervision, who is very detailed and patient in both the research field and life. Whenever his help is needed, he is always there, spending countless time in revising my papers and thesis, and helping me stay focused on my research target. He is one of the greatest assets to any student, and I do feel very privileged to work with him throughout these years.

I would also like to thank Dr. Philip Vardon for his continuous support and guidance. His expertise, and much personal advice are greatly appreciated, and very helpful to my research. Special thanks go to Prof. Zhen Chen and Dr. Shan Jiang from the University of Missouri, in the United States, for their help and advice in MPM program coding during my stay in America.

Sincere thanks to the China Scholarship Council and TU Delft for their financial support of this PhD research.

I would also like to thank my colleagues, both past and present, for their support and help throughout my studies. Many interesting and insightful discussions and talks have benefited me greatly.

On a more personal note, I would like to sincerely thank many of my friends in Delft for their friendship and support, which made the years in Delft very pleasant and sweet. No matter how far the distance will be, the friendship, in particular during my last months in Delft, will make me smile.

Finally I would like to express my thanks to my Mother and Father for their unwavering love, support and advice throughout all of my studies.

# CURRICULUM VITÆ

## Bin WANG

20-04-1989      Born in Anqing, China.

## EDUCATION

2005–2009       Undergraduate in Civil Engineering
                Wuhan University of Technology, P.R. China

2009–2011       Postgraduate in Geotechnical Engineering
                Wuhan University, P.R. China

2011–Present    Ph.D. Candidate in Geotechnical Engineering
                Technische Universiteit Delft, the Netherlands
                *Thesis:*       Slope failure analysis using the material point method
                *Promotor:*     Prof. dr. M. A. Hicks

## AWARDS

2013       Best poster award of department research meeting
2016       Best paper award of Géotechnique Letters for second quarter of 2016

# LIST OF PUBLICATIONS

## JOURNAL PUBLICATIONS

3. **Wang, B., Hicks, M. A., and Vardon, P. J.**, *Slope stability analysis using the random material point method*, Géotechnique letters, **6**(2), 113-118, 2016.

2. **Wang, B., Vardon, P. J., and Hicks, M. A.**, *Investigation of retrogressive and progressive slope failure mechanisms using the material point method*, Computers and Geotechnics, **78**, 88–98, 2016.

1. **Wang, B., Vardon, P. J., and Hicks, M. A.**, *Development of an implicit material point method for geotechnical applications*, Computers and Geotechnics, **71**, 159– 167, 2016.

## CONFERENCE PUBLICATIONS

1. **Wang, B., Vardon, P. J., and Hicks, M. A.**, *Implementation of a quasi-static material point method for geotechnical applications*, in: Proceedings of the 3rd International Symposium on Computational Geomechanics, pp. 305–313, Krakow, Poland, 2013.

2. **Wang, B., Vardon, P. J., and Hicks, M. A.**, *Investigation of aspects of an implicit dynamic material point method implementation*, in: 8th European Conference on Numerical Methods in Geotechnical Engineering, vol. 1, pp. 313–318, Delft, the Netherlands, 2014.

3. **Wang, B., Vardon, P. J., and Hicks, M. A.**, *Preliminary analysis of rainfall-induced slope failures using the material point method*, in: Proceedings of the 12th International Symposium on Landslides, pp. 305–312, Napoli, Italy, 2016.